Grid Development and a Study of B-flavour tagging at DØ

Philip William Lewis
Imperial College London

A thesis submitted for the degree of
Doctor of Philosophy
of the University of London
and the Diploma of Imperial College

September, 2006

Grid Development and a Study of B-flavour tagging at DØ

Philip William Lewis
Imperial College London

September, 2006

ABSTRACT

Run IIa of the DØ experiment at the Tevatron took place between Spring 2002 and Spring 2006, collecting approximately 1.2 fb^{-1} of data. A fundamental principal of the DØ computing model is the utilisation of globally distributed computing resources as part of a grid. In particular use is made of the "SAMGrid". The first part of this thesis describes the work undertaken at Imperial College on several DØ distributed computing projects. These included the deployment and development of parts of the SAMGrid software suite, and participation in the Winter 2003/2004 data reprocessing effort.

One of the major goals of the DØ experiment is the observation of mixing in the B_s^0-meson system. The measurement of the mixing frequency is important as it can be used to constrain the CKM matrix, which describes CP violation in the Standard Model. The second part of this thesis describes the development of an opposite side flavour tagging algorithm and its calibration using B^+ and B_d^0 meson decays. The application of this algorithm to an analysis of the B_s^0 meson system is then described, which lead to the world's first two-sided limit on the B_s^0 meson oscillation frequency (Δm_s) which was measured to lie in the interval between 17 ps^{-1} and 21 ps^{-1} at the 90% confidence level.

Acknowledgements

I would like to thank...

My supervisors Gavin Davies and David Colling for their help and support and Rick Jesik for supervising me in my time at Fermilab,

PPARC and Imperial College for providing me with the finances and opportunity to do this PhD,

The B-physics group at DØ and in particular my collaborators on the B_d-flavour tagging note, and those who worked on the B_s-mixing analyses.

My workmates at DØ and Imperial,

All my flatmates in Herne Hill, Wicker Park, the village and Seven Sisters,

Last but not least my Mum, Dad and Sister.

Contents

Abstract **2**

Acknowledgements **3**

Contents **4**

List of Figures **8**

List of Tables **13**

Preface **15**

Chapter 1. The DØ experiment at the Tevatron **18**

1.1 The Tevatron 19

1.2 The DØ detector 21

  1.2.1 Coordinate system 22

  1.2.2 Central tracking 22

  1.2.3 Preshower detectors 27

  1.2.4 Calorimeter 28

  1.2.5 Muon system 30

  1.2.6 Trigger system 33

Chapter 2. The Standard Model and CP violation **35**

2.1 Discrete symmetries in the Standard Model 35

2.2 The CKM Matrix 37

2.3 Constraints on the CKM matrix from B^0-oscillations 39

2.3.1 CKM parameter values 40
2.4 Mixing in the neutral B-meson system 42
2.5 B-Physics at the Tevatron 44
2.5.1 B-production at the Tevatron 44
2.5.2 Collecting and reconstructing B-decays 46

Chapter 3. Distributed Computing and the DØ experiment 50
3.1 The DØ computing model 51
3.1.1 DØ computing requirements 51
3.1.2 Grid computing 53
3.2 SAMGrid 54
3.2.1 SAM 54
3.2.2 JIM v1 55
3.3 SAMGrid and DØ Run II 56
3.4 Job management 56
3.4.1 Monitoring Monte Carlo jobs 56
3.4.2 Advertisement of resources 57
3.5 Data management 59
3.5.1 Specification 61
3.5.2 Design 61
3.5.3 The *Storemgr* module 64
3.5.4 Performance and Conclusions 67
3.6 $p14$ reprocessing (Winter 2003/2004) 68
3.6.1 Organisation 69
3.6.2 Operation 71
3.6.3 Certification 72
3.6.4 Results 73
3.7 $p17$ reprocessing 74
3.7.1 Preparation 74
3.7.2 Operation 75
3.7.3 Results 75
3.8 Conclusions 75
3.8.1 Summary 75

Chapter 4. B_d Mixing Analysis **77**

4.1 Sample selection 77

  4.1.1 Selection cuts 78

4.2 Flavour tag construction 80

  4.2.1 The likelihood ratio method 83

  4.2.2 Construction of probability distributions 84

  4.2.3 Discriminating variables 85

  4.2.4 Results 90

4.3 B_d^0 mixing analysis 95

  4.3.1 Mass fitting procedure 95

  4.3.2 Asymmetry fitting procedure 103

4.4 Results 111

4.5 Systematic errors 126

4.6 Conclusions 128

Chapter 5. B_s Mixing Analysis **131**

5.1 Sample selection 131

  5.1.1 Selection cuts 131

  5.1.2 Signal optimisation 133

5.2 Fitting procedure 134

  5.2.1 Signal PDF 137

  5.2.2 Background PDF 140

5.3 Amplitude fit method 140

  5.3.1 Systematic errors 142

5.4 Results 142

5.5 Cross checks 145

  5.5.1 Binned asymmetry fit of Δm_d 145

  5.5.2 Amplitude fit for Δm_d 147

5.6 Conclusions 147

Chapter 6. Conclusions **149**

6.1 Distributed Computing for DØ 149

6.2 B^0-oscillations 150

References **153**

List of Figures

1.1 The Tevatron accelerator complex. 19

1.2 The peak luminosity produced by the Tevatron during the course of Run IIa, (April 2001 to February 2006). 21

1.3 The integrated luminosity produced by the Tevatron over the course of Run IIa, (April 2001 to February 2006). 22

1.4 Cross section of the DØ Run II detector. An enlarged view of the inner sections is shown in Figure 1.5. 23

1.5 The central tracking region. 24

1.6 The DØ Silicon Microstrip Tracker. 25

1.7 The DØ Calorimeter. 29

2.1 The unitarity triangle. 39

2.2 Dominant box diagrams for B_q^0–$\bar{B}_q^0$ mixing[22]. 39

2.3 Constraints the unitarity triangle, Summer 2005. 41

2.4 Feynman diagrams illustrating the leading order QCD production mechanisms for b-quarks at the Tevatron. 45

3.1 The amount of raw and reconstruced data/GB produced per day between July 2001 and July 2003. Periods in which no raw/reconstructed data are produced correspond to the detector shutdowns. 52

3.2 The monthly Monte Carlo production/GB for DØ between July 2001 and June 2003 52

3.3 A simplified schematic of the SAM system 55

3.4 Workflow for reprocessing. 70

3.5 Overlay of RecoCert plots from Lyon (Red) and Manchester (Black). Plots overlap almost exactly, illustrating that differences to physical quantities due to CPU type were negligible. 73

3.6 Pie chart showing the percentage of remotely reprocessed events at each site. In total 100 M events were reprocessed remotely. 74

3.7 Breakdown of the number of events reprocessed with $p17$ at each participating site. 75

4.1 The $K\pi\pi - K\pi$ invariant mass for selected μD^* candidates. The curve shows the result of the fit with a double Gaussian signal, and exponential plus linear background function. 81

4.2 The $K\pi$ invariant mass for selected μD^0 candidates. The curve shows the result of the fit described in Section 4.3.1. 81

4.3 The $K\pi$ invariant mass for selected μD^* candidates. The curve shows the result of the fit described in Section 4.3.1. 82

4.4 Dilution of events tagged by Q_{SV} versus the coefficient k. Distribution shown for events which included a muon tag candidate (red circles) and those without a muon tag candidate (blue squares). The statistical errors shown for different k coefficients are correlated. 89

4.5 a) Distribution of muon jet charge for muons with $NSEG = 3$. b) Distribution of muon jet charge for muons with $NSEG < 3$. c) Distribution of electron jet charge. The $q(b^{rec})$ is the charge of the b quark from the reconstruction side. The tag variable distributions for events with reconstructed b-flavour (drawn as points) and $\bar{b}$-flavour (drawn as a histogram) should be symmetrical within statistical fluctuations, and the ratio of the distributions at each point is used to calculate the likelihood ratio R. 92

4.6 a) Distribution of secondary vertex charge for events with muon. b) Distribution of secondary vertex charge for events without muon. c) Distribution of event jet charge. The $q(b^{rec})$ is the charge of the b quark from the reconstruction side. The tag variable distributions for events with reconstructed b-flavour (drawn as points) and $\bar{b}$-flavour (drawn as a histogram) should be symmetrical within statistical fluctuations, and the ratio of the distributions at each point is used to calculate the likelihood ratio R. 93

4.7 Normalised distributions of the combined tagging variable. The $q(b^{rec})$ is the charge of the b quark from the reconstruction side. The clear separation of the two distributions illustrates the power of the combined tag to discriminate between events with b- and $\bar{b}$-flavour. 94

4.8 The $K\pi$ invariant mass for reconstructed $B \rightarrow \mu D^{*} X$ Monte Carlo events. The square black markers correspond to events in which $D^0 \rightarrow K^+\pi^-$. The triangular red markers correspond to events in which $D^0 \rightarrow K^+\pi^-\pi^0$. 97

4.9 Tagged $M(K\pi)$ distribution for events in the D^* sample, tagged by the three taggers: muon, SV charge and electron, and by the combined tagger for $|d| > 0.3$. The fitted function and parameters corresponds to eqn. (4.13). 112

4.10 The fit to $M(K\pi)$ mass for non-oscillating (left) and oscillating (right) for $\mu^+ D^{*-}$ events tagged by the SV charge with $|d| > 0.3$ in bins -0.025-0.0, 0.0-0.025, 0.025-0.050, 0.050-0.075 113

4.11 The fit to $M(K\pi)$ mass for non-oscillating (left) and oscillating (right) for $\mu^+ D^{*-}$ events tagged by the SV charge with $|d| > 0.3$ in bins 0.075-0.100, 0.100-0.125, 0.125-0.250 114

4.12 The fit to $M(K\pi)$ mass for non-oscillating (left) and oscillating (right) for $\mu^+ D^{*-}$ events tagged by the Muon tagger with $|d| > 0.3$ in bins -0.025-0.0, 0.0-0.025, 0.025-0.050, 0.050-0.075 115

4.13 The fit to $M(K\pi)$ mass for non-oscillating (left) and oscillating (right) for $\mu^+ D^{*-}$ events tagged by the Muon tagger with $|d| > 0.3$ in bins 0.075-0.100, 0.100-0.125, 0.125-0.250 116

4.14 The asymmetries obtained in the D^* (left) and D^0 (right) samples with the result of the fit superimposed for the Muon and electron tagger. For the individual taggers, $|d| > 0.3$ was required. The drop in the negative VPDL bin is due to the $c\bar{c}$ background. Flavour oscillation of the B_d meson component is responsible for the fall in asymmetries across the positive VPDL bins. 118

4.15 The asymmetries obtained in the D^* (left) and D^0 (right) samples with the SV and the combined tagger and the result of the fit superimposed. The samples required $|d| > 0.3$. The drop in the negative VPDL bin is due to the $c\bar{c}$ background. Flavour oscillation of the B_d meson component is responsible for the fall in asymmetries across the positive VPDL bins. 119

4.16 The asymmetries obtained in the D^* (left) and D^0 (right) samples with the combined tagger in $|d|$ bins, 0.1-0.2 and 0.2-0.3. The result of the fit is superimposed. As expected the measured asymmetries correspond to the $|d|$ interval with larger asymmetries found for events with larger values of $|d|$. 120

4.17 The asymmetries obtained in the D^* (left) and D^0 (right) samples with the combined tagger in $|d|$ bins, 0.3-0.45 and 0.45-0.6. The result of the fit is superimposed. As expected the measured asymmetries correspond to the $|d|$ interval with larger asymmetries found for events with larger values of $|d|$. 121

4.18 The asymmetries obtained in the D^* (left) and D^0 (right) sample with the combined tagger for bin $|d| > 0.6$. The result of the fit is superimposed. As expected the measured asymmetries correspond to the $|d|$ interval with larger asymmetries found for events with larger values of $|d|$. 122

4.19 P_T distribution of the reconstructed B^+ candidates 125

5.1 $M(K^+K^-\pi^-)$ invariant mass distribution for the untagged (left) and tagged (right) B_s^0 sample. The left and right peaks correspond to the μ^+D^- and $\mu^+D_s^-$ candidates respectively. The fitting curve uses a single Gaussian to describe the μ^+D^- signal and double Gaussian for the $\mu^+D_s^-$ signal. The background is modelled by an exponential function. 135

5.2 K-factor distributions used for the semileptonic B_s^0 decays. $P_T(B)$ is taken from Monte Carlo truth information, $P_T(\mu D_s)$ is calculated from the reconstructed tracks. 138

5.3 Efficiency to reconstruct the $B_s \rightarrow \mu^+ D_s^- X$ decay as a function of VPDL. The fall in efficiency at short VPDL is due to the significance cuts on the track impact parameters. 139

5.4 B_s^0 oscillation amplitude with statistical and systematic errors. The solid red line shows the $\mathcal{A} = 1$ axis. The dashed line shows the sensitivity $\sigma_{\mathcal{A}}$ including both statistical and systematic uncertainties. The expected limit corresponding to $\sigma_{\mathcal{A}} \geq 1$ was found to be 14.1 ps^{-1}. The measured limit corresponding to $\mathcal{A}+|\sigma_{\mathcal{A}}| \geq 1$ was found to be 14.8 ps^{-1}. There is a peak observed at $\mathcal{A} \sim 19$ ps^{-1} around which $\mathcal{A} \neq 0$ at a 95% confidence level. 144

5.5 Likelihood scan over $\Delta m_s$with amplitude $\mathcal{A} = 1$. The dotted line is drawn to illustrate the 90% conifdence limits between 17 and 21 ps^{-1}, drawn with respect to the minimum at 19 ps^{-1}. 145

5.6 The asymmetries obtained in the $\mu^+ D^-$ sample using the combined tagger and $|d| > 0.3$ cut. The asymmetries are fitted to measure the B_d^0 oscillation frequency to be 0.44 ± 0.10 ps^{-1} consistent with the world averaged measurement. 146

5.7 B_d^0 oscillation amplitude shown with statistical errors only. The solid red line shows the $\mathcal{A} = 1$ axis. The dashed line shows the sensitivity $\sigma\mathcal{A}$ using the statistical uncertainty only. The B_d^0 oscillations are clearly visible as the peak $\mathcal{A} = 1$ at ~ 0.5 ps^{-1}. 147

5.8 Constraints the unitarity triangle, Summer 2005. 148

List of Tables

3.1 The LDAP objects which contain Monte Carlo job information, along with their associated mandatory and optional attributes 57
3.2 Table showing the improvement in tracking from $p13$ to $p14$ [49]. 68
3.3 Computer centres which participated in the Winter 2004 reprocessing. 70
3.4 Breakdown of UK reprocessing resources. 71

4.1 Table showing the Chi-squared of different fits to the $B^+ \to \mu^+\nu\bar{D}^0X$ signal peak at 1.85GeV. The background fit functions are taken from Equations 4.15 and 4.16 96
4.2 Table showing the correlations between the fitted variables to the $K\pi$ mass distribution of the $B^+ \to \mu^+\nu\bar{D}^0X$ sample. Large correlations are found between the widths and R which describe the signal double Gaussian; between the position and shape of the bifurcated background peak; and between the magnitude of the exponential background and its decay constant 100
4.3 Table showing the results of a free fit to $B^+ \to \mu^+\nu\bar{D}^0X$ samples. The first column contains parameter values from the fit to all events. Subsequent columns show the significance of the deviation from this value for the fits to sub-samples. The parameters describing the background and signal peaks display no significant trends at the 3σ level. The decay constant b_0 shows significant variation across the samples. 101

4.4 Table showing the results of a free fit to $B_d^0 \rightarrow \mu^+ \nu D^{*-} X$ samples. The first column contains parameter values from the fit to all events. Subsequent columns show the significance of the deviation from this value for the fits to sub-samples. The parameters describing the background and signal peaks display no significant trends at the 3σ level. The decay constant b_0 shows significant variation across the samples. 102

4.5 Tagging performance for events with reconstructed B^0 for different taggers and subsamples. 122

4.6 Tagging performance for events with reconstructed B^+ for different taggers and subsamples. For comparison, the dilution $\mathcal{D}'_d$ measured in the D^* sample with addition of wrong sign $\mu^+ \nu \bar{D}^0 \pi^+$ events is also shown. 123

4.7 Measured value of Δm_d and $f_{c\bar{c}}$ for different taggers and subsamples. 123

4.8 The asymmetries for two samples B^+ candidates using a $P_T > 16$ GeV cut. No dependence of the asymmetry with P_T is observed. 125

4.9 The asymmetries for two samples B^0 candidates using a $P_T > 16$ GeV cut. No dependence of the asymmetry with P_T is observed. 125

4.10 Systematic uncertainties Δm_d. 129

4.11 Systematic uncertainties $\mathcal{D}(B^0)$. 130

5.1 Systematic studies shown at four example values of Δm_s 143

Preface

This thesis describes work performed as a member of the DØ collaboration and as part of the European DataGrid project between December 2002 and March 2006. The focus of this work in the period to Summer 2004 was the implementation and development of the SAMGrid software used at Imperial College and the distributed reprocessing of data across UK sites. From Spring 2004 the work focused on an initial state flavour tagging algorithm for B-meson decays. This involved the certification and calibration of the algorithm in a measurement of the B_d^0 mixing frequency using $B \rightarrow \mu^+ \nu \bar{D}^0 X$ decays. The calibrated tagger was then applied to an analysis of B_s^0-mixing in semileptonic $B_s^0 \rightarrow D_s^- \mu^+ \nu_\mu X$ decays.

Between December 2003 and September 2004 I worked closely with Rod Walker on DØ computing projects at Imperial College. These tasks included: management of Monte Carlo production, maintenance of the local SAM installation and deployment and development of SAMGrid software in order to run DØ jobs. In particular I was responsible for modifications to the SAMGrid information and monitoring system to collect and display details of Monte Carlo production jobs, and for the creation of a data management tool *Storemgr* designed to store files within the SAMGrid framework. From September 2004 to June 2005 I was the sole person responsible for running DØ computing projects at Imperial College. I managed the certification process for the nine sites participating in the $p14$ data reprocessing task, and was responsible for the reprocessing operations at the three UK sites. In addition I undertook preparatory work for the $p17$ reprocessing task on the LeSC and RAL Tier 1A computing farms.

I have been a member of the B-physics group at DØ since Spring 2004. I was an active member of the B-mixing and lifetimes subgroup and collaborated on the development of an opposite side flavour tagging algorithm and its application to mixing analyses of semileptonic B_d^0 and B_s^0 decays. In particular I was one of the principal authors of the *bdmixing_tag* package, which provides a standard tool for analysing the performance of a flavour tagging algorithm. This contains code to perform the whole analysis chain to make a B_d^0-mixing frequency measurement using a binned asymmetry fit and includes systematic studies. In addition it produces calibration values for the tag. The calibrated tagger was then applied in the B_s^0-mixing analysis, for which I performed a cross-check by measuring the B_d^0-mixing frequency by using the binned asymmetry fitting code to fit the B_d^0 meson signal component.

The thesis has the following structure:

- Chapter 1 is a brief description of the DØ detector at the Tevatron accelerator complex.
- Chapter 2 describes the theoretical motivation for studying oscillations in the neutral B_s^0 and B_d^0 meson systems, and summarises the theoretical framework of B-oscillations within the Standard Model. In addition topics relevant to performing B-physics at the Tevatron are introduced.
- Chapter 3 describes the grid activities undertaken at Imperial College. The reasons for utilising grid computing for the DØ experiment are given. The SAMGrid framework and the work done to extend the capability of the Job Information and Management (JIM) package are described. The Winter 2003/2004 $p14$ reprocessing task is then described including the operation and management of the participating UK sites.

- Chapter 4 describes the development of the combined opposite side flavour tagging algorithm. The application of this tagger to the $B \to \mu^+ \nu \bar{D}^0 X$ semileptonic decays is described, and the measurement of the B_d^0-mixing frequency and the tagger performance presented.
- Chapter 5 describes the application of the combined flavour tagging algorithm to semileptonic $B_s^0 \to D_s^- \mu^+ \nu_\mu X$ decays. The amplitude and log-likelihood methods are outlined, and the first two-sided experimental limit on the B_s oscillation frequency is presented.
- Chapter 6 provides a summary and outlook.

In this thesis natural units are used such that $\hbar \equiv c \equiv 1$ and energy, momentum and mass values are given in GeV. In addition charge conjugation is implied throughout the B-meson analyses described in Chapters 4 and 5.

Chapter 1

The DØ experiment at the Tevatron

The Tevatron collider at Fermilab is the highest energy particle accelerator in operation. It first collided 900 GeV proton-antiproton beams in 1985. The DØ experiment was proposed in 1983 in order to study high mass states and high pT phenomena. The first data taking period Run I, took place between 1992 and 1996. During this time the Tevatron operated with 6 bunches of protons / antiprotons with 3500 ns between the bunch crossings. The beams collided with a centre of mass energy of 1.8 TeV and the peak luminosity was typically $\sim$1–2$\times 10^{31}$ cm^{-2}s^{-1}. In total 120 pb^{-1} data was recorded by the experiment.

Many important results were made from the Run I dataset. These included the discovery of the top quark[1] and measurement of its mass; a precision measurement of the mass of the W boson; detailed studies of gauge boson couplings and jet production; and limits on new phenomena including leptoquarks and supersymmetry.

At the end of Run I major upgrades were made to the Tevatron accelerator including a new Main Injector and the antiproton Recycler[2]. These upgrades enable the instantaneous luminosity to be increased by an order of magnitude. This is necessary if the DØ experiment is to accumulate the much greater integrated luminosity needed to pursue a more ambitious physics programme. The Run II goals include making precise measurements of the top quark and W-boson masses; studies of CP violation and mixing in B-physics; searches for the Higgs boson; and physics beyond the standard model.

Run IIa of data collecting took place between March 2001 and April 2006. During this time the Tevatron operated with 36 bunches of protons / antiprotons and a bunch spacing of 396 ns. The beams collided with a combined energy of 1.96 TeV in the centre of mass frame. At the end of Run IIa the instantaneous luminosity regularly exceeded 1×10^{32} cm^{-2}s^{-1}, and in total approximately 1 fb^{-1} of data were recorded by the DØ experiment.

1.1 The Tevatron

There are several stages to producing the proton-antiproton beams which collide at the DØ detector. The components of the accelerator can be seen in Figure 1.1.

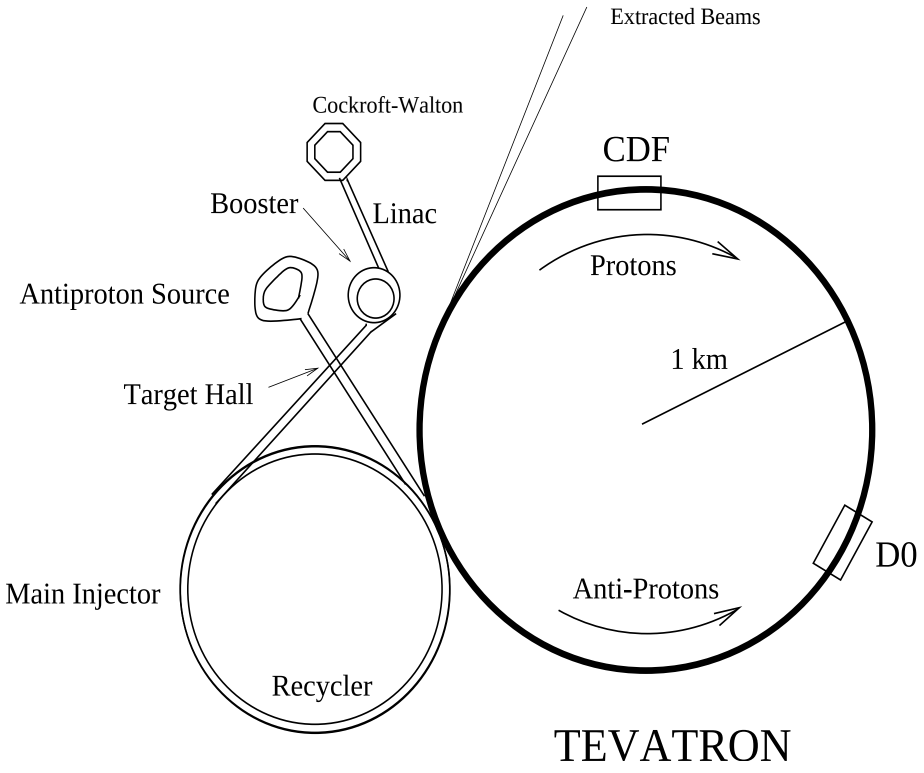

Figure 1.1: The Tevatron accelerator complex.

Proton production begins with the acceleration of negatively charged hydrogen ions to 750 KeV in a Cockcroft-Walton accelerator. They are boosted to 400 MeV in the Linac, a 150 m linear accelerator, and then fired through a thin carbon foil to produce protons. These are accelerated to 8 GeV in a synchrotron called the Booster, then passed into the Main Injector. Here the protons are boosted to 150 GeV for injection into the Tevatron, or to 120 GeV for antiproton production.

Antiprotons are produced by firing the 120 GeV protons into a fixed nickel target. The resulting shower of particles is focused with a lithium lens and passed through a charge-mass spectrometer to separate out the antiproton component. This is passed into the Debuncher where the antiprotons are cooled stochastically and formed into a continuous beam. This beam is delivered to the Accumulator where the antiprotons are further cooled. Once a sufficient number has been collected, the antiprotons are passed into the Recycler, a fixed energy ring in the same tunnels as the Main Injector, used as storage for antiprotons. Before injection into the Tevatron the Main Injector is used to accelerate the antiprotons to 150 GeV.

The protons and antiprotons are injected into the Tevatron in bunches and travel around it in opposite directions. Each proton bunch contains approximately 10^{11} protons and each antiproton bunch contains approximately 10^{10} antiprotons. The beams are kept separate while they are accelerated to energies of 0.98 TeV, then focused to cross at the DØ and CDF detectors, where antiproton-proton collisions occur with a centre of mass energy of 1.96 TeV.

At a luminosity of 0.5×10^{32} cm^{-2}s^{-1} there are on average 2 proton-antiproton interactions per bunch crossing. At the projected luminosity of 2×10^{32} cm^{-2}s^{-1} this would increase to 7 interactions. The increased level of occupation could lead to saturation in some parts of the detector. To prevent this it has been decided to use lumi-levelling, which is the process of dynamically changing beam focus to limit the peak luminosity. This reduces the number of interactions per bunch crossing but allows the luminosity to be maintained for a longer period, so that the integrated luminosity is reduced by only 15%.

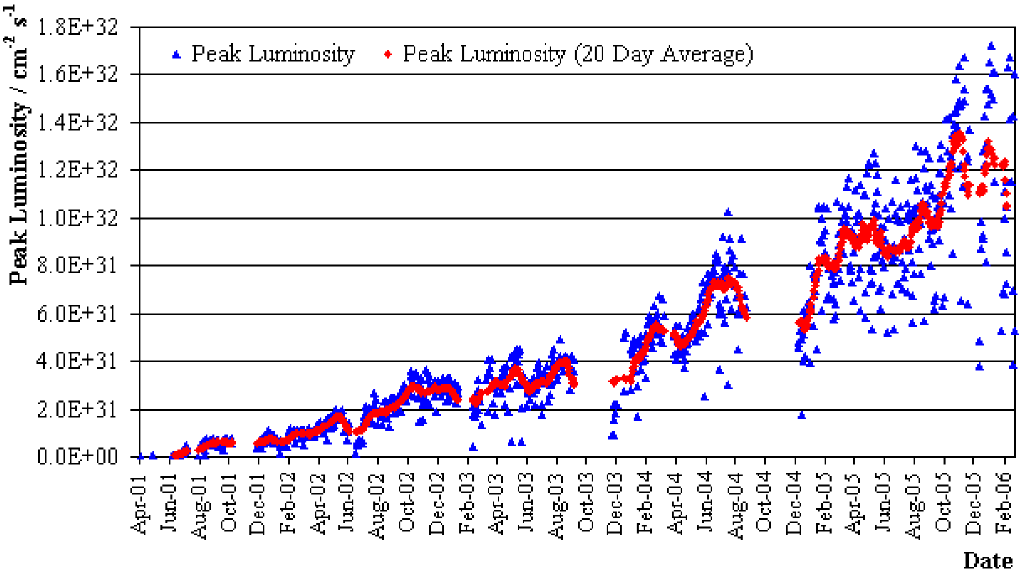

Figure 1.2: The peak luminosity produced by the Tevatron during the course of Run IIa, (April 2001 to February 2006).

Figures 1.2 and 1.3 show the peak and integrated luminosity delivered to the DØ detector. The Tevatron is now operating according to the Run II design specifications, reaching peak luminosities close to 2×10^{32} cm^{-2}s^{-1} and delivering an integrated luminosity of $\sim$ 20pb^{-1}/week. Increases to the luminosity are planned up to 2007 by increasing the number of antiprotons in each bunch. This will be achieved by improving the cooling in the Debuncher and Accumulator, and once commissioning of the Recycler ring is completed. Run II is scheduled to last until 2009. In total an integrated luminosity of between 4.4fb^{-1} (baseline) and 8.5fb^{-1} (design) should be collected.

1.2 The DØ detector

The upgraded DØ detector can be seen in Figures 1.4 and 1.5. It is described in detail in [3]. It is a multipurpose high energy physics detector, with a cylindrical layered structure that is symmetrical about the interaction region.

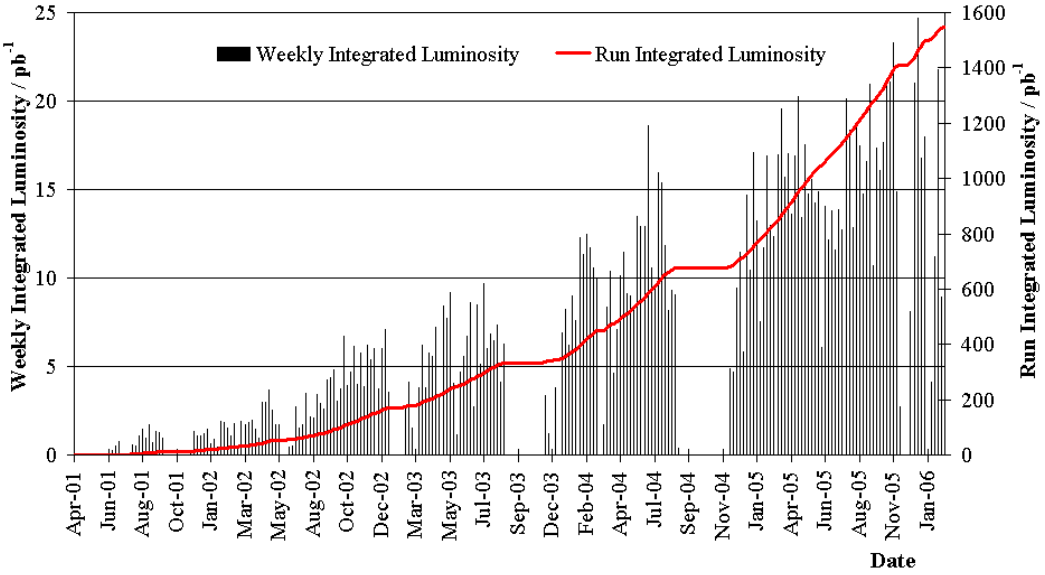

Figure 1.3: The integrated luminosity produced by the Tevatron over the course of Run IIa, (April 2001 to February 2006).

1.2.1 Coordinate system

The experiment has adopted a right handed coordinate system. The z-axis is along the proton direction, the y-axis is upwards, and the x-axis points towards the centre of the Tevatron. For many purposes the azimuthal angle ϕ and the pseudorapidity η are used. The pseudorapidity is given by $\eta = -\ln[\tan(\theta/2)]$ where θ is the polar angle. In the high energy limit ($E >> mc^2$) this approximates the Lorentz invariant true rapidity given by $y = 0.5\ln[(E + pz)/(E - pz)]$. The term "forward" is used to describe regions at high $|\eta|$.

1.2.2 Central tracking

The central tracking system of the DØ detector was completely replaced in preparation for Run II. The system shown in Figure 1.5 consists of a high resolution silicon microstrip tracker (SMT) surrounded by a scintillating fibre tracker (CFT) both enclosed within a 2 T solenoidal magnet. The combined system covers a region out to $|\eta| \leq 3$. It allows the measurement of charged particle momenta, electron identification, e/π rejection, and B-tagging on displaced secondary vertices.

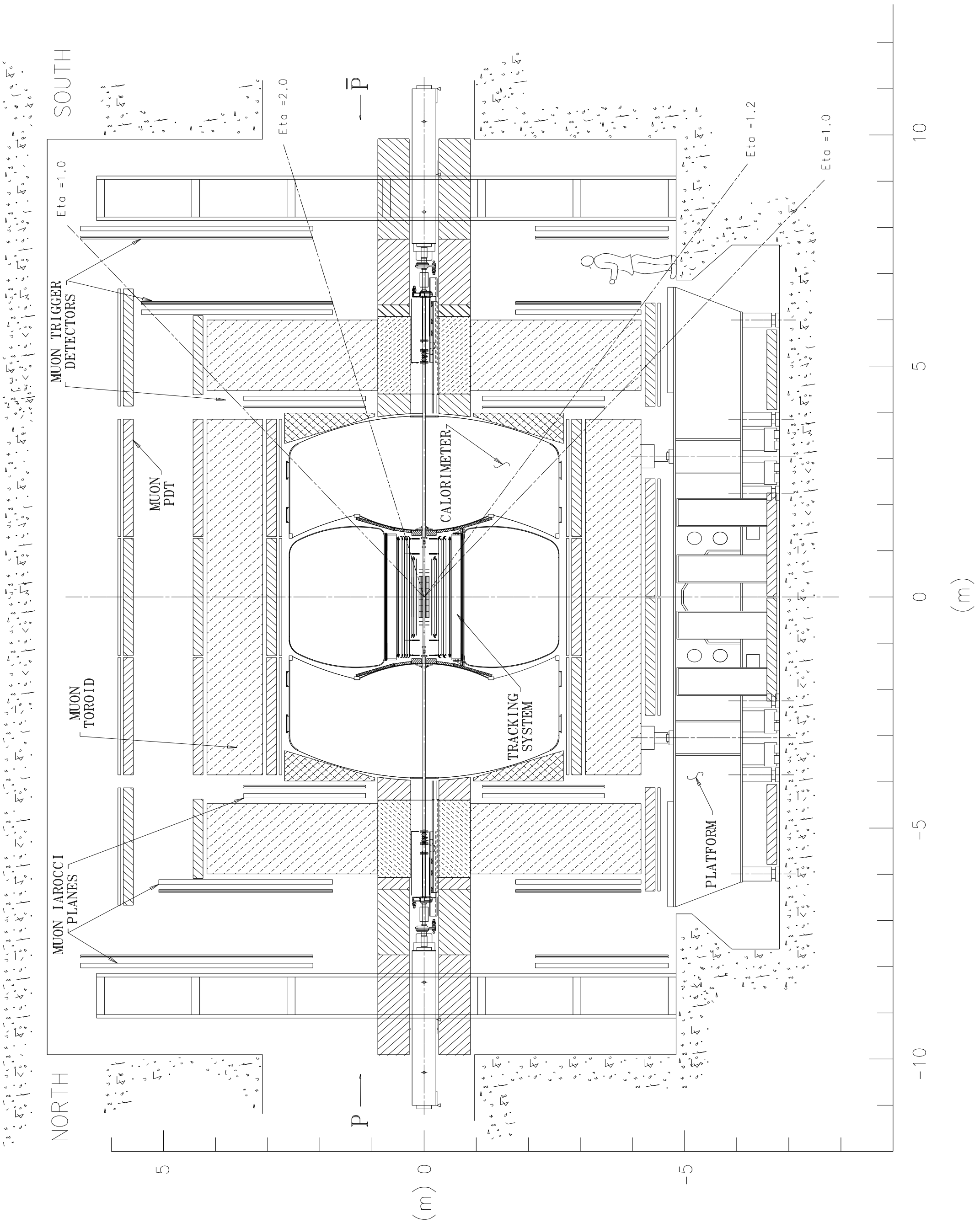

Figure 1.4: Cross section of the DØ Run II detector. An enlarged view of the inner sections is shown in Figure 1.5.

Silicon microstrip tracker

The high resolution SMT is situated closest to the interaction region. It provides tracking, primary vertexing and the capability for secondary vertex reconstruction

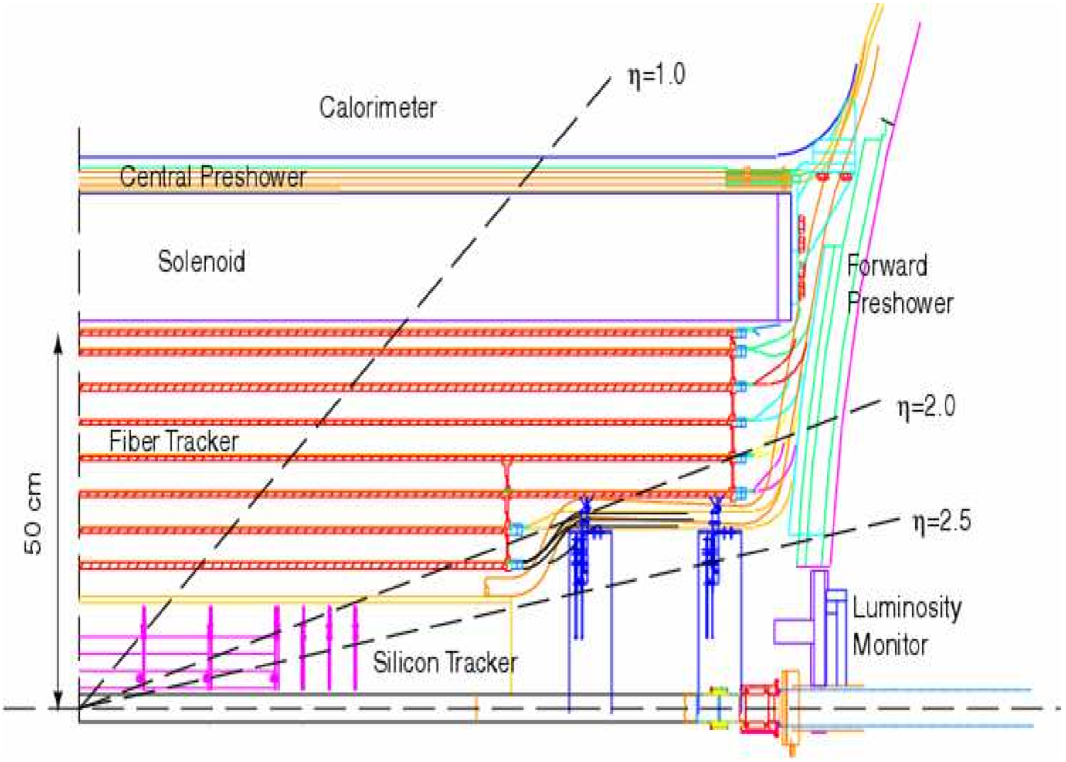

Figure 1.5: The central tracking region.

used in the identification of B decays. It is built with 50 μm pitch silicon microstrip modules. In order to optimise the tracking resolution, tracks should intercept the detector surfaces perpendicularly for all η. The extended z-length of the interaction region ($\sigma_z \approx 25$ cm) motivated the hybrid design of barrel and disks shown in Figure 1.6. Three barrels are placed on either side of the interaction region. Each barrel unit is made with four concentric readout layers of silicon modules individually known as “ladders”. An “F-disk” consisting of 12 wedge shaped detectors caps the end of each barrel. There are three additional F-disks at each end of the central region followed by two larger “H-disks” which provide coverage at high $|\eta|$.

Layers 2 and 4 of the barrels consist of double-sided ladders. On one side the strips run parallel to the beam and on the other the strips run at ±2° to provide a “stereo” measurement. Layers 1 and 3 consist of double-sided ladders with stereo strips which run perpendicular to the beam direction, except for the ladders in

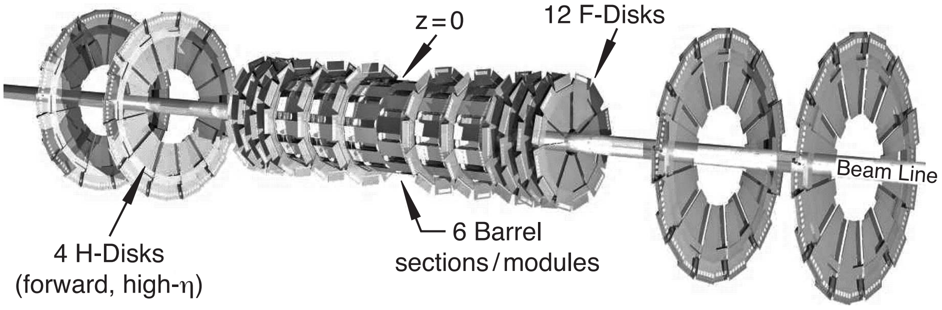

Figure 1.6: The DØ Silicon Microstrip Tracker.

the outer two barrels which are single-sided. The wedges in the F-disks are also double-sided, with the strips on each side running parallel to one of the long edges to produce a 30° stereo angle. Each wedge in the H-disks is formed from two back to back single-sided detectors with a stereo angle of 15°. In total there are 912 readout modules and almost 800,000 channels.

Central fibre tracker

The CFT provides track reconstruction and momentum information out to $|\eta| < 1.6$. It consists of eight cylindrical layers of scintillating fibres mounted on a carbon-fibre frame. Each cylinder has an axial and a stereo doublet layer of fibres. In the axial doublet both layers of fibres run parallel to the z-axis, while in the stereo doublet both layers are orientated at $\pm 3°$. The six outer CFT cylinders are 2.52 m in length. The two innermost cylinders are 1.66 m to accommodate the H-disks of the SMT.

The layers of fibres are built using "ribbons". Each ribbon has two layers of 128 fibres, offset by half a fibre spacing to provide maximum coverage. The scintillating fibres are 835 μm in diameter and made of a polystyrene core covered in two claddings which enhance the optical transmission and mechanical properties. The core is doped with 1% by weight paraterphenyl which has a rapid fluorescence decay and emits light at a wavelength of 340 nm. This wavelength is poorly transmitted in polystyrene, so the core is also lightly doped with a wave-shifter dye, (1500 ppm

3-hydroxyflavone). This absorbs the 340 nm radiation and re-emits it at 540 nm which is well transmitted in polystyrene.

The scintillating fibres connect to clear fibre waveguides that carry the light to visible light photon counters (VPLCs). These are extremely sensitive with a quantum efficiency $\geq 75\%$, a gain of 22,000 to 65,000, and are capable of detecting single photons. The VPLC cartridges are housed in a cryostat under the detector and operate at a temperature of 8 K. In total the CFT system has 76,800 channels and comprises of 200 km of scintillating fibre and 800 km of clear fibre. It has a hit efficiency of 98%.

The combined system of SMT and CFT allows the measurement of transverse momentum with resolution $\Delta P_T/P_T = (2 + 0.2 \times P_T)\%$[5]. The position of primary vertices can be reconstructed with a resolution of 35μm in the xy-plane. The transverse track impact parameter resolution is dependant on the track P_T, it is ~ 50 μm for a track with $P_T = 1$ GeV, decreasing asymptotically to ~ 15 μm at 10 GeV [28].

Solenoid

A superconducting solenoidal magnet surrounds the CFT and SMT. The 2 T field was chosen to optimize the momentum resolution and track pattern recognition of the central tracking system, while fitting within the available space of the pre-existing central calorimeter vessel (2.70 m length, 1.42 m diameter). The magnet can be operated in both polarities and is alternated at regular intervals. The solenoid is wound with 2 layers of superconducting Cu:NbTi cable. Larger windings are used towards each end of the solenoid to produce a uniform field throughout the tracking volume, such that the variation in the integrated field ($\sin\theta \times \int \mathbf{B}_z \mathrm{d}l$) along a path reaching the solenoid is less than 0.5% [6]. The solenoid operates within a helium cryostat and has a total stored energy of 5.3 MJ. The combined system of solenoid and cryostat has a thickness of 1.1 radiation lengths (X_0) at normal incidence.

1.2.3 Preshower detectors

The preshower detectors aid electron identification and background rejection. In addition they are used to improve the spatial matching between central tracking and the calorimeter, and to correct the electromagnetic energy measured in the calorimeter due to losses in the solenoid and other upstream material. The position of these detectors can be seen in Figure 1.5. The central preshower detector (CPS) fits in the ~5 cm gap between the solenoid and central calorimeter, covering the region $|\eta| < 1.3$. The two forward preshower detectors (FPS) are attached to the end calorimeters and cover the region $1.5 < |\eta| < 2.5$.

The CPS consists of three layers of prismatic scintillator strips 6 mm wide. The inner layer is axial, followed by stereo layers at ±24°. The strips are doped with 1% p-terphenyl and 150 ppm diphenyl stilbene, and optically insulated with aluminized mylar. Embedded in the centre of each strip is a wavelength shifting fibre that collects and transmits the light to the end of the detector, where it is transferred to a VLPC cartridge via a clear waveguide. A lead sheet between the solenoid and CPS provides a total path of $2X_0$ upstream of the CPS for tracks at normal incidence, increasing to about $4X_0$ at the largest angles.

The FPS consists of two double layers of scintillator strips separated by a stainless steel/lead absorber which provides $2X_0$ of material for showering. The "minimum ionizing particle" (MIP) layer upstream of the absorber covers the region $1.6 < \eta < 2.5$. The shower layer beyond the absorber covers the region $1.5 < \eta < 2.5$. Both are made of eight wedge shaped modules with dual layers of scintillator strips set at a stereo angle of 22.5°.

The MIP layer in the FPS aids particle identification. Charged particles passing through the MIP layer will leave a minimum ionizing signal, allowing measurement of the track location. Electrons will shower in the absorber leading to a cluster of energy recorded in the shower strip. Heavier charged particles are less likely to shower and will leave another minimum ionizing signal in the shower layer. High energy photons will pass through the MIP layer without interacting, but shower in the absorber. The MIP layer covers the region beyond $|\eta| > 1.6$ as tracks with $|\eta| < 1.6$ pass through the solenoid, which provides ample material for showering.

1.2.4 Calorimeter

The DØ calorimeter is used to study the transverse energy balance in events and for the energy measurement and identification of electrons, photons, jets and muons. It was left largely unchanged from Run I except for the readout electronics which have been upgraded to deal with the shorter bunch crossing time. The system, shown in Figure 1.7, consists of three separate uranium/liquid argon sampling calorimeters and intercryostat detectors. The central calorimeter (CC) covers the region $|\eta| \leq 1$. The two end calorimeters (EC) extend this coverage to $|\eta| \leq 4$. Each calorimeter is housed in a separate cryostat and operated at 90 K.

The calorimeters are segmented into cells of size $\Delta\eta \times \Delta\phi \approx 0.1 \times 0.1$, except in the region $|\eta| > 3.2$ where segmentation in η and ϕ increases to avoid very small cells. Each cell contains a layer of absorbing material to induce showering and a layer of liquid argon in which shower particles deposit their energy through ionization. The ionised charge is collected by copper plates at high voltage (2.0 kV) within each cell, with a typical electron drift time of 450 ns. The design is known as a compensating calorimeter because neutrons interact with the uranium absorbing plates through nuclear fission, resulting in an equalised calorimeter response to hadronic and electromagnetic showers.

The calorimeters each contain electromagnetic, fine hadronic and coarse hadronic sections, built with different absorbers. The inner electromagnetic section consists of four layers of cells, containing depleted uranium absorbing layers 3 mm (CC) or 4 mm (EC) thick. In the third layer, which corresponds to the EM shower maximum, the cells are twice as finely segmented ($\Delta\eta \times \Delta\phi \approx 0.05 \times 0.05$) to

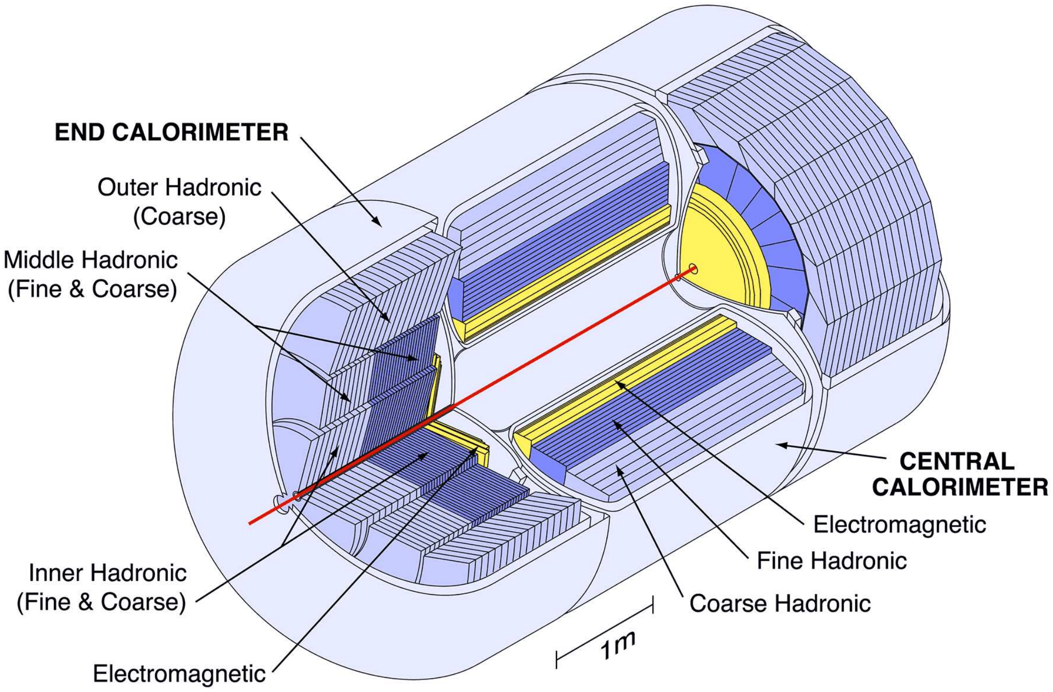

Figure 1.7: The DØ Calorimeter.

allow accurate location of the shower centroid. The fine hadronic section has 6 mm uranium niobium absorbing layers. It is here that the majority of hadronic energy is deposited. Beyond this section there is the coarse hadronic sections with 46.5 mm absorbing layers of copper (CC) or stainless steel (EC) which collect any leakage from the fine hadronic section.

The energy resolution of the calorimeter was measured to be [4]:

$$\begin{aligned} \text{EM: } (\sigma_E/E)^2 &= (0.16/\sqrt{E})^2 + (0.003)^2 \\ \text{Hadronic: } (\sigma_E/E)^2 &= (0.41/\sqrt{E})^2 + (0.032)^2 \qquad (1.1) \end{aligned}$$

The central calorimeter has 7.2 nuclear absorption lengths of material at normal incidence and the end calorimeters have 10.3 nuclear absorption lengths at the smallest angle of incidence. In total there are around 50,000 calorimeter readout channels.

Massless gaps and intercryostat detectors

In the region where the cryostats overlap $0.8 < \eta < 1.4$ there is incomplete calorimeter coverage and a substantial amount of unsampled material. The massless gaps and intercryostat detectors provide additional sampling and enable a correction for energy loss in this region. The massless gaps refer to a layer of calorimeter readout cells located before the first absorbing layer in the central and end calorimeters. The intercryostat detectors are made up of scintillating tiles mounted on the exterior surface of the end cryostats which cover the region $1.1 < |\eta| < 1.4$. Each tile is divided into twelve subtiles which cover an area $\Delta\eta \times \Delta\phi \approx 0.1 \times 0.1$. The light from each subtile is transferred via wavelength shifting fibres, then clear waveguides to a photomultiplier tube for readout.

1.2.5 Muon system

The muon system enables muon triggering and measurement. Central coverage in the region $|\eta| \leq 1.0$ is provided by the central muon system which incorporates original Run I proportional drift tubes (PDTs) and the central scintillation counters. For Run II the forward muon system has been added. This extends coverage to $|\eta| \leq 2.0$ and consists of mini drift tubes (MDTs) and trigger scintillation counters.

The muon system includes the toroidal magnets visible in Figure 1.4. These cause muon trajectories to bend in the x-y plane and allow an independent measurement of momentum to be made. This enables muon triggering with a lower p_T cutoff; cleaner matching of muons to their central tracks; better rejection of π/K decays; and improves momentum resolution for high p_T muons.

Central muon detector

There are three layers of drift chamber PDTs in the central muon system. The A-layer of PDTs is closest and is located within the central toroidal magnet. The B- and C-layers are located outside the magnet. Approximately 55% of the central region $|\eta| \leq 1.0$ is covered by all three layers, and 90% is covered by at least two layers. The A-layer has four decks of PDTs except for the bottom section which has three. The B- and C-layers have three decks of PDTs. Each deck is typically 2.8 m × 5.6 m, and made from extruded rectangular aluminium tubes 10.1 cm wide and 5.5 cm in height. The tubes contains a central anode wire, with vernier cathode pads above and below that help determine the hit position along the wire. The gas mixture used is argon, methane, CF_4 $(84\%, 8\%, 8\%)$ which has an electron drift velocity of $\simeq$ 10 cmμs^{-1}. This results in a maximum drift time of ~500 ns and drift distance resolution of 1 mm. The gas mixture is faster than that used in Run I. This is necessary to reduce the number of beam crossings within the drift time interval, but also leads to an increased uncertainty in hit position due to diffusion.

There are two sets of scintillation counters in the central muon system: the cosmic cap and bottom, and the Aϕ counters. The cosmic cap and bottom counters are mounted on the outer layer of the PDTs. The accurate timing signal from these counters is used to associate a muon to a particular bunch crossing and reject out-of-time background hits, e.g. due to cosmic rays. The counters are 25” wide, 81.5-113” long and made of 0.5” Bicron 404A scintillator. Wavelength shifting fibres glued into grooves in the Bicron transmit the signal to one of two PMTs mounted on each counter. A typical muon signal produces between 18 and 30 photoelectrons. In total the cosmic cap and bottom contain 372 counters.

The Aϕ scintillation counters cover the inner surface of the A-layer PDTs. They are of a similar design to the counters in the cosmic caps, and have a segmentation in ϕ of approximately 4.5° to match the CFT trigger sectors. This enables in-time scintillation hits to be combined with CFT tracks in low level muon triggers. In addition the Aϕ scintillation counters provide timing information for low momentum muons which do not penetrate the toroid to the cosmic counters.

Forward muon detector

The forward muon system covers the region $1.0 \leq |\eta| \leq 2.0$. It consists of three layers of mini drift tubes and three layers of scintillation counters at either end of the detector. The MDTs were chosen because of their short electron drift time (<130 ns) and high segmentation. This means that they have a low occupancy and good coordinate resolution ($\lesssim$1 mm). The innermost A-layer has four decks of MDTs and is located within the end toroidal magnets. The B- and C- layers are located outside the magnets and have three decks of MDTs each. Each MDT consists of eight 9.4 mm × 9.4 mm cells formed from an extruded Aluminium comb and stainless steel cover. A 50 μm W-Au anode wire runs down the centre of each cell. The gas mixture used is CF_4-CH_4 (90%-10%) which is non-flammable, fast and causes minimal aging of the anode in the high radiation environment. In order to save the cost of individual time-to-digital converters for each channel, the signal arrival time is measured with respect to the beam crossing timebin. The resulting accuracy of 18.8 ns limits the co-ordinate resolution to 1.9 mm. The FAMUS MDTs enable a standalone momentum measurement with a resolution of approximately 20% for muons $P_T^\mu < 40$ GeV. This can improve the resolution of the central tracking measurement for muons with $P_T^\mu > 100$ GeV. It is also important for muons which do not pass through all the layers of the CFT in the region $1.6 \leq |\eta| \leq 2.0$.

The FAMUS scintillation counters are mounted on the inner surface of the A-layer MDTs and the outer surfaces of the B- and C- MDT layers. The counters are trapezoidal and have a ϕ segmentation of 4.5° to match the CFT trigger sectors, and η segmentation of 0.12 or 0.07. Each counter is made from 0.5" Bicron-404A scintillator, with wavelength shifting strips of Kumarin-30 along two of the edges which transmit light to an attached PMT. There are almost 5,000 scintillation counters which range in size from 9 cm×14 cm to 60 cm×110 cm.

1.2.6 Trigger system

The collision rate for Run II is ∼1.7 MHz. The cost of storage media and the processing time required for reconstruction limits the rate at which events can be stored to 50Hz. This means that for every event stored approximately $35,000$ events are discarded. The trigger system performs this task and is vital in ensuring that the physics events of interest are saved. The DØ trigger was upgraded significantly to cope with the increased collision rate of Run II and to incorporate the new central tracking system and preshower detectors. The system consists of three stages of event selection in which each successive stage examines fewer events, but with increasing sophistication.

The first stage of the trigger is Level-1 which examines basic information about each event to make a decision within 3.6 μs. The Level-1 triggers are implemented with specialised hardware and associated to subdetectors. The Level-1 central track trigger reconstructs tracks using information from the CFT and preshower detectors. It considers the CFT axial hit information in 4.5° sectors, and compares the patterns with approximately 2 million pre-defined boolean equations to identify tracks. It triggers on CFT tracks with a P_T greater than threshold which have consistent hits in the preshower detectors. The Level-1 calorimeter trigger divides the calorimeter into EM and H (hadronic) towers ($\Delta\eta \times \Delta\phi = 0.2 \times 0.2$) and calculates the transverse energy (E_T) for each tower. It triggers when a set number of towers with have E_T greater than threshold, on a global (summed) E_T threshold and on a global missing E_T threshold. The Level-1 muon trigger uses the identified CFT tracks and combines this information with MDT, PDT and scintillator hits to trigger on muon tracks.

Events which pass the Level-1 trigger are passed to the Level-2 system which accepts events at a rate of ∼1.6 kHz and makes a trigger decision within 100μs. The Level-2 triggers utilise hardware engines with embedded microprocessors. Information from the Level-1 triggers and additional data from the subdetectors are processed in the Level-2 preprocessors. The preprocessors identify physics objects such as jets, electrons, and muons. These are then passed to L2Global which forms higher quality objects by combining different subdetector objects (e.g. central tracks leading to a signature energy deposition in calorimeter) and examines event wide correlations. Events that pass the L2 trigger are fully digitised and passed to the Level-3 trigger at a rate of ∼0.8 kHz.

The Level-3 trigger uses a farm of microprocessors to perform a limited reconstruction of each event that has passed the Level-1 and Level-2 triggers. Physics algorithms are applied, and the final decision to store or reject the event is made within a timeframe of 50-100 ms. The output rate of the Level-3 trigger is 50 Hz.

Chapter 2

The Standard Model and CP violation

The Standard Model is well described in [7]. It is a highly successful theory used to describe particle physics phenomena in terms of constituent fermions (quarks and leptons) interacting through exchange of gauge bosons (gluons, W^+, W^-, Z and γ).

It is a renormalisable, relativistic quantum field theory based on the gauge symmetry group $SU(3)_C \otimes SU(2)_L \otimes U(1)_Y$, where $SU(2)_L \otimes U(1)_Y$ describes the electroweak interaction, and $SU(3)_C$ the strong interaction. The spontaneous symmetry breaking of the $SU(2)_L \otimes U(1)_Y$ group gives mass to the W^+, W^-, Z bosons and the fermions via the Higgs mechanism[8].

2.1 Discrete symmetries in the Standard Model

In addition to continuous symmetry of gauge invariance, the Standard Model lagrangian is invariant under the discrete Charge-Parity-Time (CPT) transformation. This is a combination of three operations:

Charge Conjugation (C)

Charge conjugation inverts the sign of all internal quantum numbers such as charge, baryon/lepton number, strangeness. Each particle transforms to its antiparticle. Other quantities such as spin, mass and momentum are unchanged.

Parity Inversion (P)

Parity inversion inverts spatial coordinates, such that $(t, x, y, z) \rightarrow (t, -x, -y, -z)$. Under this operation a right handed coordinate system transforms to a left handed system. Consequently angular momentum and spin have opposite direction relative to the particle momentum, after the parity transform.

Time Reversal (T)

Time reversal acts to invert the time coordinate such that $(t, x, y, z) \rightarrow (-t, x, y, z)$.

C, P, and T are 2-fold and discrete transformations, such that acting twice on a system returns it to the original state. It was originally believed that any physical process would be invariant under individual C, P or T transformations. This is found to be true for strong and electromagnetic interactions, but not weak interactions.

In 1957 Wu *et al.* [9] observed P violation in the radioactive beta decay of spin-polarised cobalt nuclei. Further experiments showed that C and P were maximally violated in the weak sector but suggested the symmetry was preserved under the combined transformation of CP. For example, the charged W boson couples to the left-handed electron and to its CP conjugate (right-handed positron), but not to the P conjugate (right-handed electron) or C conjugate (left-handed positron).

The observation by Christenson *et al.* of CP violation in neutral kaon decays in 1964 [10] demonstrated that this CP symmetry was only approximate. Neutral kaons are observed as two species, K_S^0 and K_L^0, distinguished by their lifetimes of 0.9×10^{-10} s and 5×10^{-8} s respectively. The short-lived K_S^0 decay mainly into two pion states (π^+, π^-) and (π^0, π^0), which are even eigenstates of CP. The long-lived K_L^0 decay mainly into three pion states (π^+, π^-, π^0) and (π^0, π^0, π^0) which are CP odd eigenstates[1]. It was therefore believed that the K_S^0 and K_L^0 physical eigenstates

---

[1] The three pion system (π^+, π^-, π^0) can be in an even CP eigenstate for excited states with non-zero orbital angular momentum

corresponded to the even and odd CP eigenstates respectively. However Christenson *et al.* observed that a small fraction of K^0_L particles ($1.95 \pm 0.2 \times 10^{-3}$) decayed into two pion even CP states, and so K^0_L and K^0_S could not be CP eigenstates.

As a result the assumption of CP-symmetry was replaced with the weaker condition of CPT symmetry. The CPT Theorem[11] states that any quantum field theory, such as the Standard Model, which obeys certain properties including Lorentz invariance, local (anti-)commutation relations, and spin-statistics, is CPT invariant. A consequence of CPT theory is that the masses of any particle and its antiparticle are equal. This has been experimentally verified with a high precision in the K^0 system [12]:

$$\frac{m_{K^0} - m_{\overline{K}^0}}{m_{average}} < 10^{-18} \tag{2.1}$$

CP violation means that the symmetry between matter and antimatter is broken, which allows a possible explanation for the observed dominance of matter in the universe[13]. However these studies indicate that level of CP violation described by the Standard Model is too low to account for this, providing a hint that further sources of CP violation must exist in the physics beyond the Standard Model.

2.2 The CKM Matrix

In the Standard Model CP violation occurs via the weak interaction. This couples the quark doublets (u, d'), (c, s'), (t, b') and allows transitions between quark generations. Here d', s' and b' are linear combinations of the physical mass eigenstates d, s and b, formed through a rotation in flavour space. The Cabibo-Kobayshi-Maskawa matrix [14] is the matrix representation of this rotation:

$$V_{CKM} = \begin{pmatrix} V_{ud} & V_{us} & V_{ub} \\ V_{cd} & V_{cs} & V_{cb} \\ V_{td} & V_{ts} & V_{tb} \end{pmatrix} \tag{2.2}$$

In a 3×3 complex matrix there are 18 parameters. The constraint of unitarity on the CKM matrix reduces this to 9 free parameters. Of these parameters five phases between the elements are physically unobservable and therefore arbitrary, (the global phase, the two relative phases between the *uct* quarks, and the two relative phases between the *dsb* quarks). This means the CKM matrix can be described by 4 independent parameters: three real numbers and a complex phase which parameterises CP violation.

At the time of development of the quark mixing matrix, only two quark generations had been discovered. The 2 × 2 Cabibo matrix that describes the weak interaction in this case has only one free parameter and does not describe CP violating interactions. It was to provide a mechanism for CP violation that Kobayashi and Maskawa proposed the existence of a third quark generation.

A standard parameterisation of the CKM matrix is to set the relative phases so that V_{ud} and V_{cb} are real. The rotation in flavour space can then be described by three real angles $(\theta_{12}, \theta_{13}, \theta_{23})$ in the range $[0,\frac{\pi}{2}]$ and a CP violating phase (δ_{13}) in the range $[0,2\pi]$.

$$V_{CKM} = \begin{pmatrix} c_{12}c_{13} & s_{12}c_{13} & s_{13}e^{-i\delta_{13}} \\ -s_{12}c_{23} - c_{12}s_{23}s_{13}e^{i\delta_{13}} & c_{12}c_{23} - s_{12}s_{23}s_{13}e^{i\delta_{13}} & s_{23}c_{13} \\ s_{12}s_{23} - c_{12}c_{23}s_{13}e^{i\delta_{13}} & -c_{12}s_{23} - s_{12}c_{23}s_{13}e^{i\delta_{13}} & c_{23}c_{13} \end{pmatrix}, \tag{2.3}$$

where $c_{ij} = \cos\theta_{ij}$ and $s_{ij} = \sin\theta_{ij}$.

The Wolfenstein paramterisation[15] expands the parameterisation as a Taylor expansion in $\lambda = |V_{us}| \simeq 0.22$:

$$V_{CKM} = \begin{pmatrix} 1-\frac{\lambda^2}{2} & \lambda & A\lambda^3(\rho - i\eta) \\ -\lambda & 1-\frac{\lambda^2}{2} & A\lambda^2 \\ A\lambda^3(1-\rho-i\eta) & -A\lambda^2 & 1 \end{pmatrix} + O(\lambda^4) \tag{2.4}$$

where $\lambda \equiv s_{12}, \quad A \equiv s_{23}/\lambda^2, \quad \rho + i\eta \equiv s_{13}e^{i\delta_{13}}/A\lambda^3$.

In this form the dominance of the diagonal elements, and the suppression of quark transitions between different generations is explicit.

The six unitarity relations of the CKM matrix can be drawn as triangles in the complex plane. The triangle representing the orthonormal relation between the first and third columns is shown in Figure 2.2. This triangle is an especially useful graphical representation since its sides are similar in length, and it is often referred to as *the unitarity triangle*. The area of the triangle represents the amount of CP violation in the Standard Model, and the internal angles must sum to 180^o for the Standard Model to be consistent.

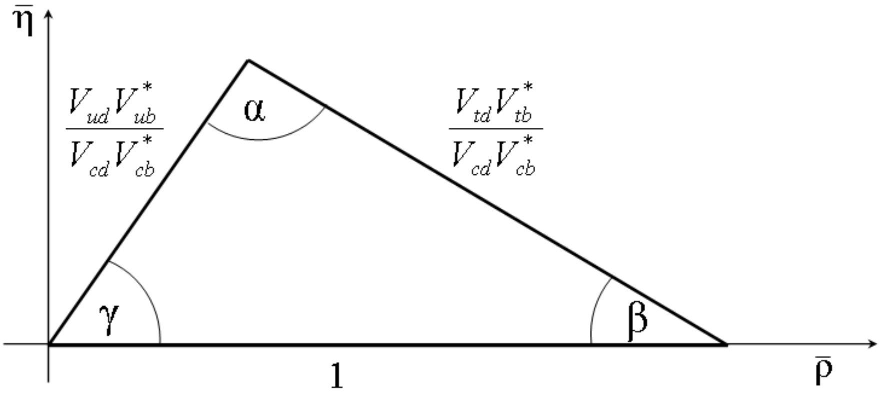

Figure 2.1: The unitarity triangle.

2.3 Constraints on the CKM matrix from B^0-oscillations

$|V_{td}|$ and $|V_{ts}|$ cannot be measured from tree-level decays of the top quark so the best experimental constraints on these parameters are made using measurements of the B_d^0 and B_s^0 oscillation frequencies. B^0–$\bar{B}^0$ mixing proceeds via box diagrams (Figure 2.3) which are dominated by the diagrams containing top quarks. The theoretical

Figure 2.2: Dominant box diagrams for B_q^0–$\bar{B}_q^0$ mixing[22].

SM prediction for this process can be found using QCD lattice calculations [17]:

$$\Delta m_q = (\text{known factor}) \times f_{B_q}^2 B_{B_q} |V_{tb}^* V_{td}|^2 \qquad q = d,\ s \tag{2.5}$$

Here Δm_q is the B_q-meson mixing frequency, f_{B_q} is the B_q-meson decay constant and B_{B_q} is the B_q-meson bag parameter, with a current theoretical calculation prediction[19]:

$$f_{B_d}\sqrt{B_{B_d}} = 244 \pm 11 \pm 24 \text{ MeV} \tag{2.6}$$

Using the assumption[2] $V_{tb} = 1$, and the world averaged value [16] ($\Delta m_d = 0.507 \pm 0.004\text{ps}^{-1}$) this results in the constraint[19]:

$$|V_{td}| = (7.4 \pm 0.8) \times 10^{-3} \tag{2.7}$$

Here the uncertainty is dominated by the theoretical uncertainty $\sigma(f_{B_d}\sqrt{B_{B_d}})$.

This constraint can be translated to place limits on the Wolfenstein parameters ρ and η using:

$$|V_{tb}^* V_{td}| \simeq |V_{td}| = A\lambda^3\sqrt{(1-\rho)^2 + \eta^2} \tag{2.8}$$

where approximation has been taken from the Wolfenstein parameterisation of the CKM matrix to $\mathcal{O}(\lambda^3)$.

The theoretical uncertainties in the lattice calculation can be reduced by taking the ratio $(f_{B_s}\sqrt{B_{B_s}})/(f_{B_d}\sqrt{B_{B_d}})$. The current calculations predict this ratio to be $1.21 \pm 0.04^{+0.04}_{-0.01}$. This can be used to place a constraint on $|V_{td}/V_{ts}|$[19]:

$$\frac{\Delta m_d}{\Delta m_s} = \frac{M_{B_d}}{M_{B_s}} \frac{f_{B_d}^2 B_{B_d}}{f_{B_d}^2 B_{B_d}} \frac{|V_{tb}^* V_{td}|^2}{|V_{tb}^* V_{ts}|^2} \propto \frac{|V_{td}|^2}{|V_{ts}|^2} = \lambda[(1-\rho^2) + \eta^2] \tag{2.9}$$

Using the Summer 2005 world averaged limit $\Delta m_s > 16.6\text{ps}^{-1}$ (95% CL) this translates to the constraint [19]:

$$|V_{td}/V_{ts}| < 0.22 \quad (95\%\text{CL}) \tag{2.10}$$

2.3.1 CKM parameter values

The Summer 2005 constraints[3] on the unitarity triangle using experimental measurements and limits on ΔM_d, ΔM_s, ϵ and $\sin 2\beta$ are shown in Figure 2.3. The

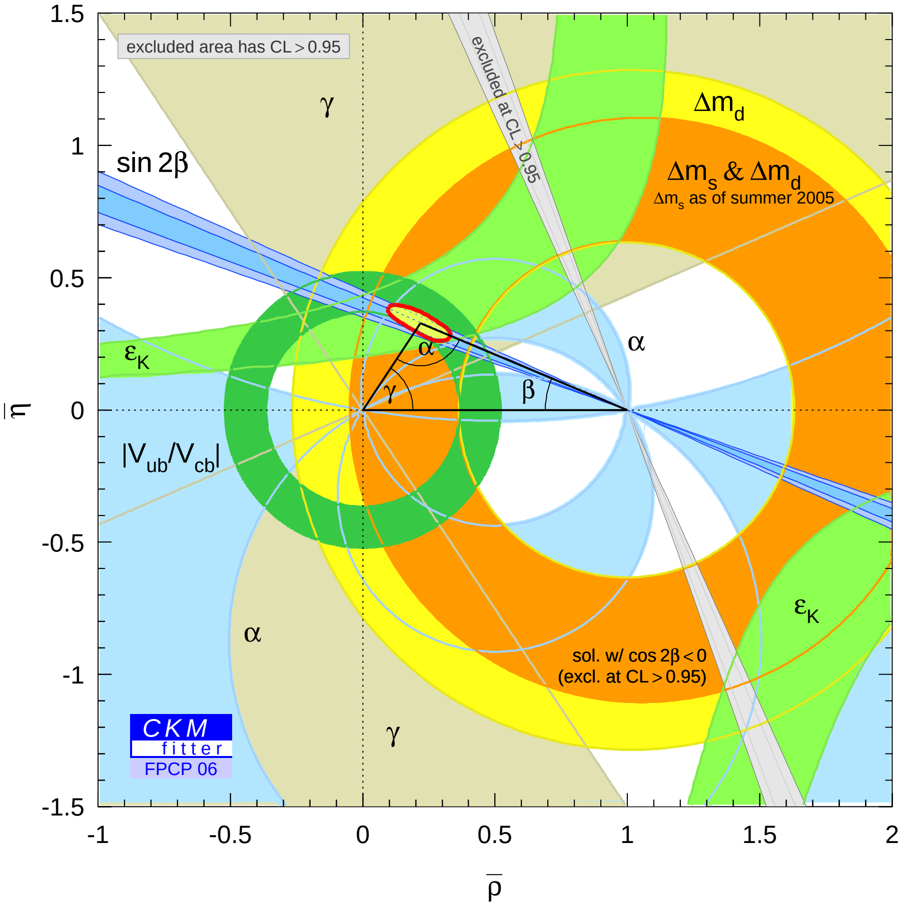

Figure 2.3: Constraints on the unitarity triangle, Summer 2005[20]

limits from the B-mixing parameters arise from Equations 2.9 and 2.8. This current constraints on the Wolfenstein parameters are [18]:

$$\begin{aligned}
\lambda &= 0.2272^{+0.0010}_{-0.0010} \\
A &= 0.809^{+0.014}_{-0.014} \\
\overline{\rho} &= 0.197^{+0.026}_{-0.030} \\
\overline{\eta} &= 0.339^{+0.019}_{-0.018}.
\end{aligned} \tag{2.11}$$

To date the measurements of CP violation are consistent with the CKM model of CP violation in the Standard Model.

---

[2] $V_{tb} = 1$ in the Wolfenstein parameterisation of the CKM matrix to $\mathcal{O}(\lambda^3)$.

[3] the current constraints are shown in Figure 5.8

2.4 Mixing in the neutral B-meson system

The neutral B-meson systems B_d^0 and B_s^0 mix with their antiparticles via 2nd order flavour changing weak interactions. The theoretical description of B^0 oscillations is as follows [21]:
Let $|B_q^0(t)\rangle$ $\left(|\bar{B}_q^0(t)\rangle\right)$ be the state vector of a B-meson tagged B_q^0 $\left(\bar{B}_q^0\right)$ at time t=0:

$$\begin{aligned}|B_q^0(t=0)\rangle &\equiv |B_q^0\rangle \\ |\bar{B}_q^0(t=0)\rangle &\equiv |\bar{B}_q^0\rangle\end{aligned} \tag{2.12}$$

The initial state evolves according to the Schrodinger equation:

$$i\frac{d}{dt}\begin{pmatrix}|B_q^0(t)\rangle \\ |\bar{B}_q^0(t)\rangle\end{pmatrix} = \left(\mathbf{M} - i\frac{\mathbf{\Gamma}}{2}\right)\begin{pmatrix}|B_q^0(t)\rangle \\ |\bar{B}_q^0(t)\rangle\end{pmatrix}. \tag{2.13}$$

where the mass matrix $\mathbf{M}$ and decay matrix $\mathbf{\Gamma}$ are time independent Hermitian 2×2 matrices.

CPT invariance places the following constraints on the matrix elements:

$$\begin{aligned}M_{11} = M_{22}, \quad M_{12} = M_{12}^* \\ \Gamma_{11} = \Gamma_{22}, \quad \Gamma_{12} = \Gamma_{12}^*\end{aligned} \tag{2.14}$$

Mixing occurs if the off-diagonal elements are non-zero and the flavour eigenstates are not eigenstates of mass. In this case the heavy and light mass eigenstates (B_{qH} and B_{qL}) can be found by diagonalizing the matrix $\mathbf{M}-i\mathbf{\Gamma}/2$ and expressed in terms of the flavour eigenstates:

$$\begin{aligned}|B_{qH}\rangle &= p|B_q^0\rangle + q|\bar{B}_q^0\rangle \\ |B_{qL}\rangle &= p|B_q^0\rangle - q|\bar{B}_q^0\rangle\end{aligned} \tag{2.15}$$

where $|p|^2 + |q|^2 = 1$. In the case that $|p/q| = 1$ the mass eigenstates correspond to the CP eigenstates, in the case that $|p/q| \neq 1$ the mass eigenstates are not eigenstates of CP and CP violation may occur via the mixing process.

The solution of Schrodinger's equation for the time evolution of the mass eigenstates is trivial:

$$|B_{qH,L}(t)\rangle = e^{-(iM_{H,L}+\Gamma_{H,L}/2)t}|B_{qH,L}\rangle, \tag{2.16}$$

This can then be substituted into the inverted form of Equation 2.15 to describe the time evolution of the flavour eigenstates:

$$\begin{aligned} |B_q^0(t)\rangle &= \frac{1}{2p}\left[e^{-iM_Lt-\Gamma_Lt/2}|B_{qL}\rangle + e^{-iM_Ht-\Gamma_Ht/2}|B_{qH}\rangle\right] \\ |\bar{B}_q^0(t)\rangle &= \frac{1}{2q}\left[e^{-iM_Lt-\Gamma_Lt/2}|B_{qL}\rangle - e^{-iM_Ht-\Gamma_Ht/2}|B_{qH}\rangle\right] \end{aligned} \tag{2.17}$$

This can be rewritten in terms of the time independent flavour eigenstates $|B_q^0\rangle$ and $|\bar{B}_q^0\rangle$ using Equation 2.15:

$$\begin{aligned} |B_q^0(t)\rangle &= g_+(t)|B_q^0\rangle + \frac{q}{p}g_-(t)|\bar{B}_q^0\rangle \\ |\bar{B}_q^0(t)\rangle &= g_+(t)|\bar{B}_q^0\rangle + \frac{p}{q}g_-(t)|B_q^0\rangle \end{aligned} \tag{2.18}$$

$$\begin{aligned} g_+(t) &= e^{-imt}e^{-\Gamma_qt/2}\left[\cosh\frac{\Delta\Gamma_qt}{4}\cos\frac{\Delta m_qt}{2} - i\sinh\frac{\Delta\Gamma_qt}{4}\sin\frac{\Delta m_qt}{2}\right] \\ g_-(t) &= e^{-imt}e^{-\Gamma_qt/2}\left[-\sinh\frac{\Delta\Gamma_qt}{4}\cos\frac{\Delta m_qt}{2} + i\cosh\frac{\Delta\Gamma_qt}{4}\sin\frac{\Delta m_qt}{2}\right] \end{aligned}$$

Here $\Delta m_q = M_H - M_L$, $\Delta\Gamma_q = \Gamma_L - \Gamma_H$ and $\Gamma_q = (\Gamma_L + \Gamma_H)/2$. It is useful to note that:

$$|g_\pm(t)|^2 = \frac{e^{-\Gamma_qt}}{2}\left[\cosh\frac{\Delta\Gamma_qt}{2} + \cos\Delta m_qt\right] \tag{2.19}$$

Now consider the flavour specific decay $B_q^0 \to f$, for which the $\bar{B}_q^0 \to f$ is forbidden, *i.e* $\langle f|\bar{B}_q^0\rangle = 0$ and there is no direct CP violation, *i.e.* $\left|\langle f|B_q^0\rangle\right| = \left|\langle\bar{f}|\bar{B}_q^0\rangle\right|$. For a population of initial B_q^0 the time dependent decay rates into f and $\bar{f}$ can be expressed as:

$$\begin{aligned} \Gamma\left(B_q^0(t) \to f\right) &= N_f\left|\langle f|B_q^0(t)\rangle\right|^2 \\ \Gamma\left(B_q^0(t) \to \bar{f}\right) &= N_f\left|\langle\bar{f}|B_q^0(t)\rangle\right|^2 \end{aligned} \tag{2.20}$$

Where N_f is a time independent normalisation factor.

Substituting in equation 2.18 we find:

$$\begin{aligned}\Gamma(B_q^0(t) \to f) &= N_f \left|\langle f|B_q^0\rangle\right|^2 \frac{e^{-\Gamma_q t}}{2}\left[\cosh\frac{\Delta\Gamma_q t}{2} + \cos\Delta m_q t\right] \\ \Gamma(B_q^0(t) \to \bar{f}) &= N_f \left|\langle \bar{f}|\bar{B}_q^0\rangle\right|^2 \left|\frac{p}{q}\right|^2 \frac{e^{-\Gamma_q t}}{2}\left[\cosh\frac{\Delta\Gamma_q t}{2} - \cos\Delta m_q t\right] \qquad (2.21)\end{aligned}$$

For the B_d^0 and B_s^0 systems the magnitude of $(|p/q|^2 - 1)$ is expected to be small $\sim \mathcal{O}(10^{-3})$. In addition the ratio $\Delta\Gamma_i/\Delta m_i$ is expected to be $\simeq \mathcal{O}(m_b^2/m_t^2)$ [22]. Therefore in B^0 oscillation analyses the following approximation is usually taken:

$$\begin{aligned}\Gamma(B_q^0(t) \to f) &= N_f \left|\langle f|B_q^0\rangle\right|^2 \frac{e^{-\Gamma_q t}}{2}\left[1 + \cos\Delta m_q t\right] \\ \Gamma(B_q^0(t) \to \bar{f}) &= N_f \left|\langle f|B_q^0\rangle\right|^2 \frac{e^{-\Gamma_q t}}{2}\left[1 - \cos\Delta m_q t\right] \qquad (2.22)\end{aligned}$$

where $\left|\langle f|B_q^0\rangle\right| = \left|\langle \bar{f}|\bar{B}_q^0\rangle\right|$ has been used.

Experimentally it is the asymmetry which is measured, defined as:

$$\begin{aligned}A_0(t) &= \frac{N^{non-osc}(t) - N^{osc}(t)}{N^{non-osc}(t) + N^{osc}(t)} \\ &= \frac{\Gamma(B_q^0(t) \to f) - \Gamma(B_q^0(t) \to \overline{f})}{\Gamma(B_q^0(t) \to f) + \Gamma(B_q^0(t) \to \overline{f})} \qquad (2.23)\end{aligned}$$

where $N^{non-osc}$ and N^{osc} refer to the number of non-oscillating and oscillating signal events respectively.

Using Equation 2.22 the evolution of asymmetry for a population of initial B_q^0-mesons as a function of time can be written:

$$A_0(t) = \cos\Delta m_q t \qquad (2.24)$$

2.5 B-Physics at the Tevatron

2.5.1 B-production at the Tevatron

The QCD production mechanisms for b-quarks at the Tevatron are well described in [23]. These mechanisms all produce $b\bar{b}$-quark pairs, and it is expected that single

b-quarks are not produced. The leading order QCD production mechanisms for b-quarks are shown in Figure 2.4. These are flavour creation processes in which a $b\bar{b}$-quark pair is produced via annihilation of a light quark pair shown in Figure 2.4 (a) or gluon-gluon fusion shown in Figures 2.4 (b),(c) and (d). At the $p\bar{p}$ collision energy of $\sqrt{s} = 1.96$ TeV gluon-gluon fusion processes dominate b-pair production[4]. In such flavour creation processes the b and $\bar{b}$ quarks are produced with equal and opposite momenta in the collision center-of-mass frame, and are observed approximately back-to-back in the x-y plane.

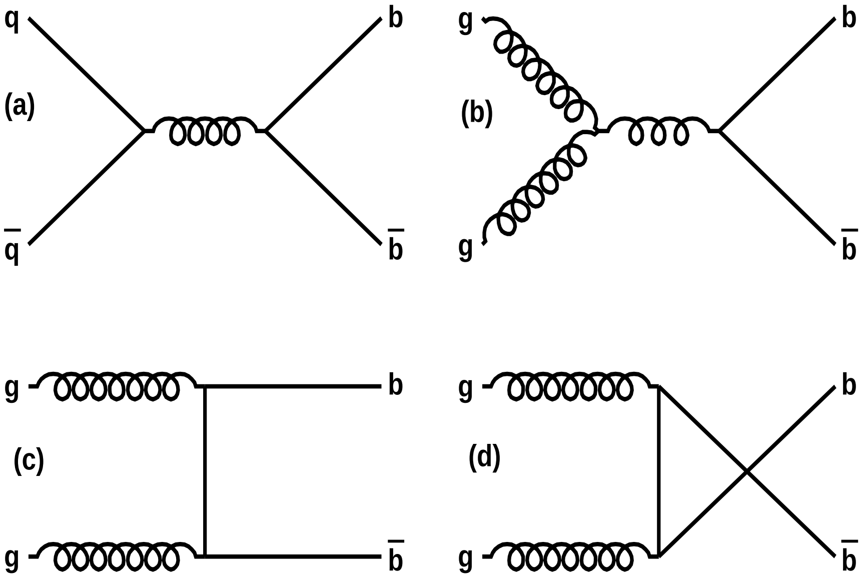

Figure 2.4: Leading order QCD production mechanisms for b-quarks at the Tevatron.

The next-to-leading-order production mechanisms of flavour excitation and shower / fragmentation are also thought to make a significant contribution to the production cross section[23]. Flavour excitation occurs when a b-quark from the “proton sea” is scattered by a gluon or light quark. Shower/fragmentation refers to the production of a $b\bar{b}$-pair after the initial $p\bar{p}$ collision, either within the parton shower or during

---

[4] c.f. top quark pair production which is dominated by $q\bar{q}$-pair annihilation[24].

the fragmentation process. In both these production mechanisms the $b\bar{b}$-quark pair are not produced back-to-back in the collision centre of mass frame, but follow an angular distribution specific to the production mechanism.

Studies comparing the measured b-production cross section with theoretical predictions are summarised in [25]. Analysis of the Run I dataset found that the measured b-production cross section was significantly greater than the predicted rate by a factor of $\sim$ 2–4. A revised theoretical study [26] including the next-to-leading-order processes reduced this discrepancy, and predicted a cross section which was consistent with the measured values in the low $P_T < 20$ GeV region. It is hoped that further improvements to the calculation will reduce the discrepancy further, but it is also possible that new physics plays a significant role in b-production[27].

Each quark in a $b\bar{b}$-pair hadronises independently into a B-meson (B_u, B_d, B_s, B_c) or B-baryon. The relative fractions (f_u, f_d, f_s and f_{bary}) were measured by CDF using Run I data. Using the assumption[5] that $f_u = f_d$ the branching fractions were calculated to be $f_u = f_d = 0.375 \pm 0.023$, $f_s = 0.160 \pm 0.044$, $f_{bary} = 0.090 \pm 0.029$.

B-hadrons decay via the weak charged current interactions. Decays proceed via off-diagonal elements in the CKM matrix. This suppresses decay and results in a $\sim \mathcal{O}(1\text{ ps})$ lifetime.

2.5.2 Collecting and reconstructing B-decays

The cross section ($\sigma_{b\bar{b}}$) for $b\bar{b}$-quark pair production at the Tevatron is approximately 0.1 mb. This can be compared to a total hadronic cross section of $\sigma_{tot} \simeq 75$ mb, and the cross section for $c\bar{c}$ production of $\sigma_{c\bar{c}} \simeq 1$ mb, which often forms a significant background in B-physics analyses.

Triggering

The DØ muon system forms the crux of the B-physics trigger strategy and the majority of the B-physics dataset is collected on single muon and di-muon triggers.

---

[5] The measurement made without this assumption found $f_d/f_u = 0.84 \pm 0.16$

Muons can be reconstructed over a wide range $|\eta| \leq 2$ (or $|\eta| \leq 1.5$ for triggers requiring a central track match) and are typically required to have a transverse momentum $P_T > 4$ GeV. The muon triggers collect semileptonic B-decays directly and hadronic B-decays by triggering on events in which the other quark in the $b\bar{b}$-pair decays semileptonically.

Topology

The long lifetime of the B-hadrons provides the means to isolate B-physics events from background processes. For the typical momentum spectra at the Tevatron, B-hadrons have a decay length of a few millimetres and the secondary decay vertex is usually well separated from the 30 μm diameter beamspot. These tracks can be identified by the high resolution central tracking system which is able to measure axial track impact parameters with a resolution[6] of $\sim 20\mu$m [28].

The B-hadrons decay via the weak interaction: 85% decay to one charmed hadron and long lived particles such as pions, kaons, muons, and neutrinos; 15% decay into two charmed hadrons and long lived particles; and 1% decay into long lived particles only [29]. Charmed hadrons have a lifetimes of order 0.1–1.0 ps and also decay within the beampipe. A typical B-physics event therefore may contain five decay vertices within the beampipe: the primary vertex, two B-decay vertices and two C-decay vertices.

Reconstruction of semileptonic B-decays

The B^0-meson mixing analyses described in this thesis utilise the semileptonic $B \rightarrow \mu^+\nu_\mu X$ decay channels. These channels play an important part in the DØ B-physics programme because the detector has an excellent muon system enabling the reconstruction of muons over a wide range ($|\eta| < 2$) with high efficiency (∼94%

---

[6] The impact parameter resolution is dependant on the track P_T, the resolution is ~ 50 μm at 1 GeV and decreases asymptotically to ~ 15 μm at 10 GeV.

in the central region) [30]. However semileptonic B-decays cannot be fully reconstructed due to the unmeasured neutrino momentum. To account for this effect when calculating the proper decay length the *visible particle decay length* (VPDL) x is defined:

$$x \equiv \left(\boldsymbol{L_{xy}} \cdot \boldsymbol{P_{xy}^{rec}}\right) / \left(P_T^{rec}\right)^2 \cdot M_B \tag{2.25}$$

Here $\boldsymbol{L_{xy}}$ is defined as the vector in the xy-plane from the primary to B-decay vertex. $\boldsymbol{P_T^{rec}}$ is the "visible" momentum of the B-candidate calculated as the vector sum of transverse momenta of the reconstructed daughter particles. The PDG value for the B-meson mass is used for M_B.

The VPDL can be converted into the proper decay lifetime t using:

$$ct = x \cdot K \tag{2.26}$$

The K-factor is the correction factor P_T^{rec}/P_T^B, representing the distribution of reconstructed transverse B-momenta (P_T^{rec}) for a given true total transverse B-momentum (P_T^B). This distribution is specific to each decay mode since it accounts for decay kinematics and for the missing momenta carried by neutrinos or other unreconstructed particles. Each K-factor distribution is determined through Monte Carlo studies.

Background processes

There are several sources of background events in the B-physics samples.

- Combinatorial background arises when random tracks in an event can be combined to form a reasonable B-vertex candidate. This background can be suppressed using mass cuts because the mass distribution for fake events will not peak at the correct B-mass. In addition cuts on the significance of the track impact parameters can be used so that tracks consistent with the primary vertex are ignored. However impact parameter cuts will not be able to eliminate combinatorial background events which are formed using the daughter particles of B- or charmed hadrons, and the contribution from such events must be considered carefully.

- Peaking backgrounds may occur through the misidentification of B-decay products. These can be particularly problematic since the reconstructed mass distribution of these events may peak in the signal region. An example is the misreconstruction of the decay $B^0 \rightarrow K^+\pi^-$ as $B^0 \rightarrow \pi^+\pi^-$. Peaking backgrounds are mode specific and must be accounted for (usually through Monte Carlo simulation) in order to correctly determine the number of signal events.
- Other sources of displaced vertices which can mimic B-decays are: decays of strange and charmed hadrons; multiple interactions per beam crossing; interactions with the detector material; and misreconstructed tracks.

Chapter 3

Distributed Computing and the DØ experiment

The initial development of the World Wide Web was largely driven by the HEP community at CERN who needed an efficient way to share information. In an analogous way the HEP community is currently driving the effort to enable "grid" computing, in order to exploit the globally distributed computing and storage resources of collaborating institutions, so that the data from the current and future HEP experiments can be processed and analysed.

The work described in the chapter took place between December 2002 and March 2004. It centred around enabling DØ specific tasks to run within the SAMGrid [33] framework, and management of the Winter 2003/2004 DØ data reprocessing at the UK sites. Work on the SAMGrid project included modifications to allow job monitoring of Monte Carlo production, the development of a storage management tool, and the incorporation of the *recocert* package into the generic job manager RunJob[41].

3.1 The DØ computing model

3.1.1 DØ computing requirements

Data taking

During data taking approximately 1 TB of data is produced daily (Figure 3.1). The format of this data is known as RAW, since it contains the raw information produced by the various sub-detectors. The raw data must be analysed to reconstruct the underlying physics objects. This is done using a dedicated central reconstruction farm located on the FNAL site. The farm operates at full capacity when data is being taken, so that the physics events are available promptly for quality checks. The Data Summary Tier or DST format is used to store the full details of the reconstructed events. For the purposes of performing many physics analyses only a subset of this information is required, and so a more manageable thumbnail or TMB format file, containing only the most relevant data is produced.

The reconstruction algorithms undergo constant revision to increase their performance, and so in order to maximise the size of the physics dataset, previously reconstructed data must be reprocessed with the latest software. It is planned that a complete reprocessing of all data will be performed with every major release of the reconstruction tools, on an approximately biannual basis.

Production of Monte Carlo data

Monte Carlo simulated data is vital in order to understand the detector and so extract the best physics results. It is also essential for testing and improving the software tools used to collect and process real data. In the period from January 2000 to June 2003 approximately 100 TB of data totalling 350 million Monte Carlo events were produced, and the production rate of approximately 3 TB a month was expected to continue (Figure 3.2).

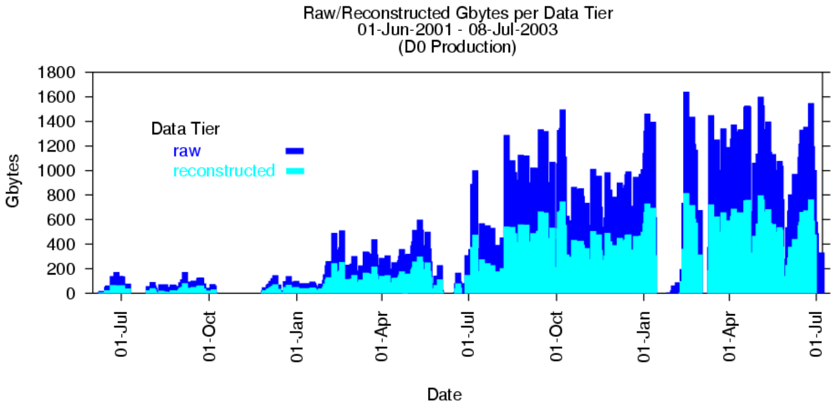

Figure 3.1: The amount of raw and reconstrued data/GB produced per day between July 2001 and July 2003. Periods in which no raw/reconstructed data are produced correspond to the detector shutdowns.

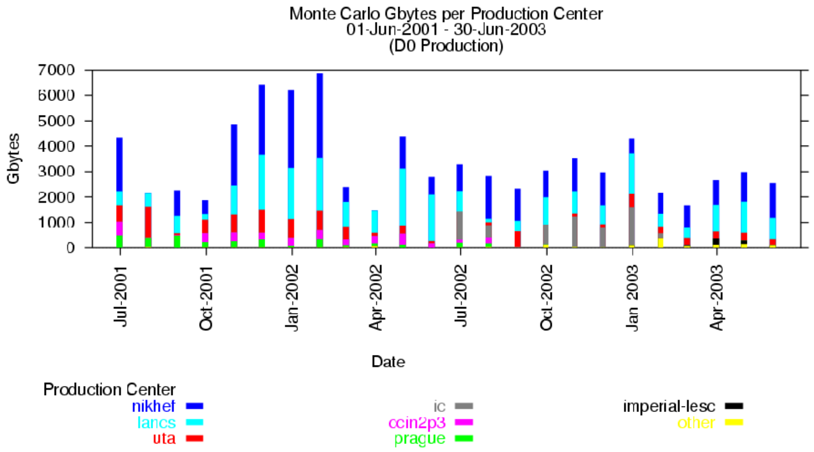

Figure 3.2: The monthly Monte Carlo production/GB for DØ between July 2001 and June 2003

Physics analysis

The analysis of the Run II data is one of the largest computing projects to date in the field of high energy physics. This necessitates a computing infrastructure which enables all collaboration members to run physics analyses on the data. In preparation for user analysis the data must be skimmed by the different physics groups. This is the process of "skimming" through the dataset, saving a subset of interesting events into a new dataset.

These tasks require computing power and data handling on an unprecedented scale in high energy physics.

3.1.2 Grid computing

Definition

A computing "grid" is a massive distributed computing resource which[34]:

Coordinates heterogenous resources not under centralised control.

It enables a collection of computers to work together in a sensible way, and perform a given task even though they may be in different locations and have different architectures, operating systems, software packages etc.

Utilises standard, open, general purpose protocols and interfaces.

The computing grid projects will be compatible with each other, with the ultimate aim that a single computing grid standard will evolve.

Delivers non-trivial qualities of service.

Users can rely on the grid to run a job, and monitor its progress. When a job finishes the output should be delivered back to the user. In the case of failure the user should be sent a suitable error report.

The Grid and DØ

Grid computing is well matched to meet the demands of the DØ experiment. The construction of a computing grid enables the collaboration to efficiently use local resources belonging to individual institutions[35]. It also allows the experiment to use external resources e.g. those in LHC Computing Grid project [36] through use of the standard grid protocols. In addition a mature computing grid will reduce the manpower required to run computing tasks, since many tasks that otherwise are done manually can be automated.

3.2 SAMGrid

The aim of the SAMGrid project is to extend the SAM data management system in use by the experiment with job and information management tools in order that a functional computing grid for the DØ experiment can be constructed. This work is focused around the development of the **J**ob and **I**nformation **M**anager (JIM) package.

3.2.1 SAM

SAM stands for **S**equential **A**ccess to data via **M**eta-data[37]. It was developed by the DØ collaboration and the FNAL computing division, and it is the sole data management tool for storing and retrieving data files at DØ. Its primary function is to serve the files associated with a given physics dataset to users from a mass storage system (MSS). The SAM system uses a database of metadata to relate files to physics datasets. This contains information such as: physics run type, trigger configuration, time and date, version of software used for processing and data format. SAM also manages the storage of files produced by the experiment onto tape and is responsible for the management of disk caches at each site. The disk caches store a copies of recently used or popular data for fast accessibility. A simplified diagram of the SAM system is shown in Figure 3.3. SAM stations are set up at each computing site. A single database at Fermilab serves all the SAM stations and contains the location and metadata of all the files stored on SAM.

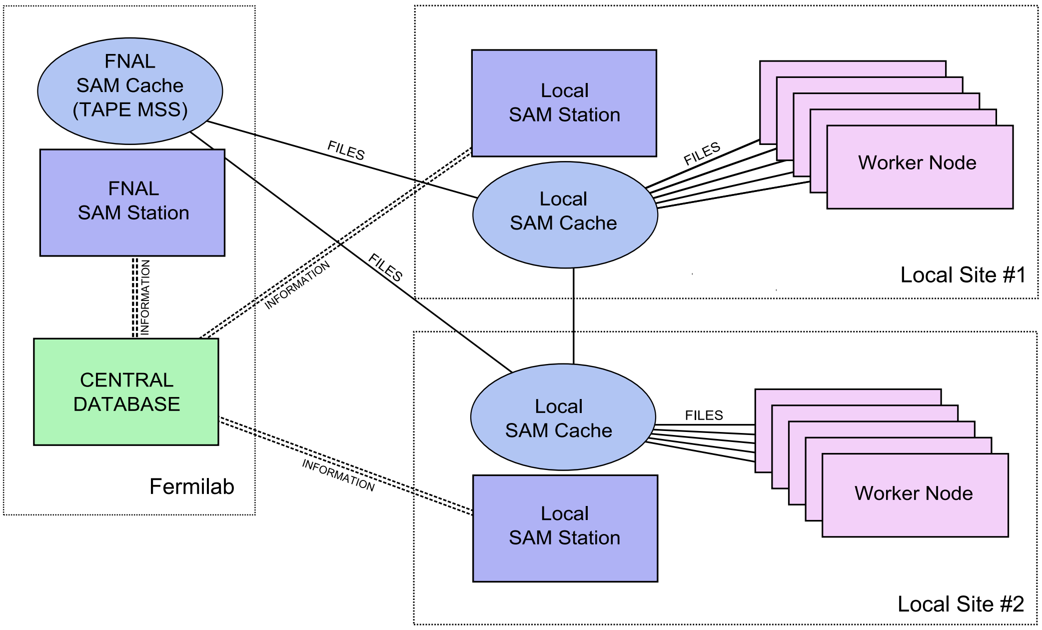

Figure 3.3: A simplified schematic of the SAM system

3.2.2 JIM v1

Run II of the DØ experiment was already underway when development of the SAMGrid began. In order that project could be functional and usable by the collaboration in the shortest possible timescale the JIM software incorporated pre-existing and proven technology wherever possible:

- The Condor[39] project provides much of JIMs underlying infrastructure. Condor is a sophisticated batch queueing system, designed for high throughput computing. Condor-G has been developed by the Condor team and Globus[40] project in close partnership with the HEP community. It modifies the Condor job management system to support the standard set of grid protocols and interfaces that make up the Globus toolkit.
- The Grid Security Infrastructure (GSI) is used to implement a secure system and authenticate users and machines.
- Job submission uses the standard Globus Resource Allocation Manager (GRAM)

protocol. Small files such as the executable or input cards are transferred to the job using the Global Access to Secondary Storage (GASS) mechanism.

- Job broking uses the Condor Matchmaking Service (MMS) to allocate submitted jobs to a suitable computing resource.

3.3 SAMGrid and DØ Run II

The release of JIM v1 in March 2003 enabled prototype SAMGrid sites to be set up. Work at Imperial College focused on making the necessary modifications to provide job management and monitoring for DØ specific tasks, in particular Monte Carlo production and reprocessing. This work centered on the integration of the RunJob tool[41]. This is a generalised version of the MC_RunJob Monte Carlo production job management tool which is able to manage generic workflows and handle data reprocessing and physics analysis. RunJob runs each DØ software executables in succession, handling the file input/output and automatically generating the associated metadata for storage into SAM if required.

3.4 Job management

3.4.1 Monitoring Monte Carlo jobs

The initial development of the JIM monitoring system was to publish the information produced by the local SAM stations. This information was collected by grid sensors and distributed using LDAP [42] before being collected and presented to users through dynamic web pages written in PHP (PHP-Hypertext-Preprocessor). In order to manage Monte Carlo production a user needs additional information, such as the location of the job, the number of events that have been processed through each stage and the status of file storage.

Following the release of JIM v1, work was undertaken to extend the existing JIM service to include this information. The first step was the inclusion into the LDAP schema of data types and objects to describe the Monte Carlo jobs, shown in Table 3.1.

Object	associated data types
DØ-MC-Request	**MUST:** DØMC-Request-ID. **MAY:** DØMC-Jobs-Total, DØMC-Jobs-Error. DØMC-Events-Requested, DØMC-Events-Stored, DØMC-Events-Done.
DØ-Local-Job	**MUST:** DØMC-Request-ID , DØMC-Local-Job-ID. **MAY:** DØMC-Nevt-DØgstar, DØMC-Nevt-DØsim, DØMC-Nevt-DØreco, DØMC-Nevt-recoanalyze. DØMC-Local-Job-Status, DØMC-Local-Start-Time.

Table 3.1: The LDAP objects which contain Monte Carlo job information, along with their associated mandatory and optional attributes

Grid sensors to collect this data were written in shell script. These typically searched through the directories in the Monte Carlo working area, parsing output log files for relevant details. This information was then converted into the LDAP format and stored. A separate branch in the LDAP tree at the local site level was used to store the Monte Carlo job details. This allowed development to continue without interfering with the existing system. The PHP code was then modified to read the Monte Carlo LDAP data and produce a useful table of information on the monitoring webpages.

The resulting system worked well, and it was easy for users to see the up to date status of their Monte Carlo jobs. However even minor changes to the data schema required multiple changes in the other layers of the system. In particular work could be done to make the PHP webpages more modular in design and dynamic with respect to changes in the LDAP schema.

3.4.2 Advertisement of resources

Condor uses a matchmaking service to send jobs to suitable computing resources. This is based on a classad system[43]. A computing resource advertises a list of resource classads that describe its attributes, *e.g.* operating system, number of

CPUs, memory per CPU. During the job submission process a corresponding job classad must be created, listing the requirements placed on the computing resources by the job. Both classads are processed by the Condor Matchmaking Service (MMS), which compares classads to decide which is the best resource for the job.

The computing resource classads are generated by the jim_advertise package. This runs on the gatekeeper node of a computing cluster. It converts an XML document containing the cluster configuration into classad form. It then executes additional scripts to generate dynamic classads, *e.g.* information such as the number of free CPUs. In order to run DØ jobs the specific DØ software releases installed at each site must be advertised, and the corresponding requirement set in the job classad. A script d0products2Classad.sh was written to generate the DØ software specific classads.

This had to support the two methods in use for installing the DØ software. The official method of installation for DØ software is via the UNIX Product Support/Distribution (UPS/UPD) system[44]. The name, version and location of all UPS installed products are recorded in a database. For Monte Carlo production the software is also released as a compressed TAR archive. The archives contain a cut down version of the full DØ software release area tailored for Monte Carlo production. This ensures that the Monte Carlo data produced at all sites is consistent. A template setup script is distributed alongside the archive. This is customised by each site to set the local software environment correctly.

The d0products2Classad.sh script deals with both cases. To find UPS/UPD installed software the *ups list* command is used. To find software installed from a TAR archive, the environmental variable SRT_DIST is called which points to the root directory for the unpacked TAR archives. This directory is then queried to determine the various versions of the software and cardfiles installed.

The best way to encode the software installation into classad form would be for the computing resource to advertise an *attribute=value* pair containing the *soft-*

ware name=version. However each machine may have several versions of the same software package installed, and at present classads must form unique attribute value pairs. Lists are not yet supported. This means that it is not possible to use a single classad to describe each software product *e.g.* so that the computing resource advertises:

```
d0software_DORun_II={ "p15.03.00", "p13.08.00", "p14.03.00" }
```

Instead it is necessary to use a less elegant solution of one classad per version of each software package, i.e. the computing resource advertises:

```
d0software_DORun_II_p15.03.00="installed"
d0software_DORun_II_p14.03.00="installed"
d0software_DORun_II_p13.08.00="installed"
```

A python module Req2Requirements was written to generate a job classad for Monte Carlo jobs. This queries the SAM database which holds a record of the specifications for each Monte Carlo request, and determines which software and cardfiles versions are required. Modifications were made so that this script is called by the mc_job module in the jim_client package. An example of the job classad produced for a request requiring DORunII release p13.08.00 with cardfile version v00_04_29 is:

```
Requirements =
    TARGET.d0software_D0RunII_p13.08.00=="Installed"
    && TARGET.d0software_cardfiles_v00_04_29=="Installed"
```

3.5 Data management

Any data produced is useless unless it is properly registered in the SAM database and made available to users. The SAM system automates much of the procedure, but a DØ “farmer” producing Monte Carlo data with the RunJob package needs to spend a significant fraction of time overseeing and managing the storage process.

SAM has been designed to automatically check that the associated metadata is valid before the file is declared to the SAM database. For Monte Carlo data files the metadata is compared to the specifications set in the Monte Carlo request. This prevents incorrectly produced data from being stored. In addition any parent files referenced must have been registered into the SAM database. This ensures that the entire set of input parameters used to generate the final data is recorded. This means that a DØ "farmer" must declare files to the database in the correct order, whilst taking care not to declare files associated with failed jobs.

Files may pass through several stages before reaching their final destination. This is usually a tape storage system at FNAL for Monte Carlo data. For example, files produced at the London e-Science Centre are staged to a storage element local to the Imperial College HEP group in order to satisfy the firewall configuration. The files then are staged onto a disk cache at FNAL, ready for permanent storage on tape. An intermediate stage might be the routing of files through an additional UK site that has a fast transatlantic connection (*e.g* RAL).

At any of these stages the file transfer is susceptible to network failure or a problem at an intermediate SAM station. SAM has been designed to cope with such failures, and will retries any transfer that has not completed after a predefined time limit. However in the case of persistent failures it is sometimes necessary for the user to intervene and manually restart the file transfer. The time taken for a file to store can be up to 24 hours when the SAM system is busy, and it is not until a file has been permanently recorded onto tape that it is safe to delete it from local disk.

At the time of JIM v1 there was no unique tool to manage the storage of Monte Carlo data files into SAM. Instead each Monte Carlo production site developed its own set of adhoc scripts tailored for the specific local configuration. The *Storemgr* package was developed at Imperial College to be a more general file storage tool which could enable jobs to run on the SAMGrid which required final file storage into SAM. It was envisaged that this tool would be used to store files during the Winter 2003/2004 reprocessing project via SAMGrid.

3.5.1 Specification

The store manager tool must:

- Select the files that are associated with jobs that have finished successfully.
- Declare the files to the SAM database in the correct order (i.e. parent files declared first).
- Initialise the SAM store for files that need to be stored.
- Check that each file reaches its destination, and restart the store in case of failure.
- Handle SAM exceptions and other errors, and deal with them intelligently.
- Delete files from disk when they are no longer needed.
- Maintain proper logs of actions, output and errors.
- Be able to run at all SAMGrid sites.

3.5.2 Design

The easiest way to implement a store manager would have been to add a file storage stage to Runjob. This was not practical because each individual job would have to remain active while the file is stored, occupying a worker node which could otherwise be doing useful work. In addition it would be difficult to recover and resume the storage process in the case of job failure. For these reasons it was decided that a single independent store manager process running on a single node would provide a much better solution.

The store manager needs a way of collecting the information concerning the files which are to be stored, and a method to log its own information about the storage status. The adhoc storage scripts used simple shell commands to list the job directories and scan log files to find successful jobs. This system could not be used in a more general tool because directory structure and the behaviour of shell commands differ significantly from site to site. Many of the JIM components, in particular the job manager, use an XML database to store job information. It seemed sensible to use the same solution to store the information needed by the store manager tool. XML is a highly structured language ideal for storing and transporting information. The following example illustrates some of the features of XML:

```
<univeristy name="Imperial College" location="London">
    <department name="Chemistry"/>
    <department name="Physics">
        <group="High Energy Physics">
            <member name="Bloggs, J." status="student"/>
            <member name="Smith, R." status="student"/>
            <member name="Jones, W." status="student"/>
        </group>
        <group="Theoretical Physics"/>
        <group="Optics"/>
    </department>
</university>
```

An XML node, e.g. the university, can have single valued attributes *e.g.* name, and can contain multiple sub-nodes e.g. departments, which in turn can have their own attributes and sub-nodes.

The structure of XML documents makes it easy to find and use the information within. Xindice[45], a native XML database was used to store the XML documents.

The standard XPath[46] and XSLT[48] protocols were used to access and process the XML data. The use of such standards mean that the tool is independent of the XML database package used.

The store management tool was written in python for compatibility with the SAM python modules. The functions needed to access the Xindice database were imported from the xmldb python module[47].

In order to maximise efficiency of the database the amount of XML used was kept to a minimum. An example of the XML file object is:

```
<file
    name="d0gstar_p13.08.00_glsqpairs-njmet_imperial_4011"
    created="Jun 13 2003 14:49:54"
    meta="import_kw_d0gstar_p13.08.00_glsqpairs-njmet_imperial_4011.py"
    mode="store"
    lastborn="false"
    valid="true"
    >
    <location host="localhost" path="/stage/d0/6105/dest/d0gstar" />
    <parent name="pythia_p13.08.00_glsqpairs-njmet_imperial_4011" />
    <status time="Jun 13 2003 14:57:59" context="validate" code="validated"/>
    <status time="Jun 13 2003 14:58:01" context="declare" code="declared" />
    <status time="Jun 13 2003 14:58:02" context="store" code="storing" />
    <status time="Jun 13 2003 16:32:45" context="store" code="stored" />
    <status time="Jun 13 2003 16:32:45" context="remove" code="success" />
</file>
```

KEY:

meta (*attribute.*)

name of file containing the metadata.

mode (*attribute.*)

designates whether the file should be stored or declared to SAM.

lastborn (*attribute.*)

designates the file as the end product of a Monte Carlo job.

valid (*attribute.*)

designates the file as ready for processing by the store manager.

location (*node.*)

contains the host and path to the file.

parent (*node.*)

contains the name of a parent file.

status (*node.*)

contains logging information written by the *Storemgr* tool.

The code used to enter the initial XML file information into the database was written by Rod Walker. This is incorporated as part of the Runjob tool. After each stage in the Monte Carlo chain finishes successfully, the information about the new file is inserted into the XML database.

3.5.3 The *Storemgr* module

The functionality needed to manage file storage is provided by the *Storemgr* python module. It contains two object classes. The *store_obj* class deals with operations on the collection of files that belong to a cluster job. The *file_obj* class deals with operations on an individual file. When a *store_obj* or *file_obj* is created the associated XML data are cached into memory in order to reduce the number of queries made to the XML database (which may be remote).

A cycle of the store manager consists of four main processes:

1. the validation of files ready to be stored
2. the declaration of new files to the SAM database
3. checking status of previous SAM stores
4. initialising new SAM stores

Logging

Common to all the stages is the use of logging. XML status objects are inserted by *Storemgr* to log each action and its outcome. These status objects are then used to track the file through the stages of the storage process.

Validation

It is not until the full Monte Carlo chain has finished without errors that files produced can be declared and stored into SAM. In order to do this *Storemgr* uses the *lastborn* attribute. This is set to true for files that are at the end of a Monte Carlo chain. A *lastborn* file that appears in the XML indicates that the job finished successfully. *Storemgr* searches for these files in the database and uses the *get_family* function which generates a list of all the parent files. These are then validated (i.e. valid attribute set to TRUE)

Declaration

Files must be declared to the SAM database in order of parentage, e.g. reconstructed data cannot be declared until the simulated data it was produced from have been declared. This is not trivial as files may have multiple parents e.g. merged thumbnail files. In order to do this *Storemgr* again searches the valid *lastborn* files using the *get_family* function. This returns a list of parents in the correct order for declaration to the SAM database. Each file is then declared. The *SAM status* object returned by the declare command is analyzed. In the case of success, a *declared* status is recorded. Otherwise the code and details are extracted from the *SAM status* object and recorded in an *error* status. An exception is the case in which a SAM error is raised because the file is already declared to the SAM database. In this case the status in the XML database is corrected. Files that are not marked for storage into SAM are deleted once they have been declared successfully.

Storage

Once the files have been declared there is no requirement on the order in which they are stored. SAM stores are initiated for those files marked to store and not already in the process of storing. Any SAM errors are recorded in the log.

Updating the store status

The *update_status* function is called with an argument AGE given in hours, (default=12). It checks files in the *storing* state and calculates the age of the status. If a file has been storing for more than AGE hours it checks to see if the file has been stored onto tape, using *sam locate*. If so it inserts a *stored* status and deletes the file from disk. If the file is not yet on tape and the status age is greater that the variable STORE_TIMEOUT (default=24 hours) an *error* status is inserted.

Overall store status

The *store_status* function checks the status of the overall job returning the number of files still in the process of declaring/storing. A file is considered finished if it has mode=declare and it has been declared, or mode=store and it has been stored. If a file is still being processed the number of errors recorded is checked. If this is greater than the variable MAX_ATTEMPTS (default=5) the file is also considered finished. In this case the file remains on disk and manual intervention is required.

Implementation

The Globus job manager runs on the gatekeeper node until the cluster-job is considered finished. Rod Walker modified the polling script to incorporate the *Storemgr* tool. Every few minutes the job manager polls each job in the cluster-job and checks if any files still need to be processed by the *Storemgr*. If all the jobs have finished running and there are no more files to be processed, the cluster-job is considered finished. Otherwise, if it is not already running, the polling script executes a new instance of the *Storemgr*.

3.5.4 Performance and Conclusions

A development version of the *Storemgr* tool was used to store much of the Monte Carlo data that was produced at Imperial from February 2003. The tool was successful in declaring and storing the files into SAM. Some stores did fail but the approach of retrying failed SAM stores after 24 hours, was successful in the large majority of cases.

The time taken to query the XML database was directly related to the number of entries it had to search through, and when the database contained several hundred files the query time became prohibitive. This problem was resolved by the creation of database indexers which cache the information necessary to search the databases. This reduced the query time to a few seconds, irrespective of the size of the database.

In a few cases the individual jobs ran on the worker nodes successfully, but the job manager process crashed. When this happened it was simple to restart the *Storemgr* tool, and resume the file store process.

It was noted that farm configuration must be such that the *Storemgr* process on the gatekeeper node must have read/write access to the files produced by the worker nodes.

Improvements could have been made to the error handling capability, in particular it would be useful to recognise when manual intervention is essential, and send an email or raise a flag on the monitoring page to that effect. This would be the case if the files are not accessible, have incompatible metadata, or the SAM station is not running.

Development on the *Storemgr* tool was halted when the decision was made not to use the SAMGrid framework in the Winter 2003/2004 reprocessing task.

3.6 p14 reprocessing (Winter 2003/2004)

The reconstruction software (RECO) algorithms undergo constant revision in order to attain the best physics performance. The p14 release contained significant improvements in the tracking algorithms and a new set of alignment measurements leading to much improved track reconstruction, as can be seen in Table 3.2. In order to make use of the 100 pb^{-1} of data reconstructed with superseded RECO versions, a round of reprocessing was planned for Winter 2003/2004. This corresponded to 300 million events, equivalent to 75 TB of RAW data stored on tape. Reconstruction of an event takes approximately ∼50 s on a 1 GHz PIII CPU. If reprocessing was to be completed within the desired timescale of three months 2,000 CPUs would have been required. This was almost double the number of CPUs in the central reconstruction farm at this time, which would only be available for reprocessing during the scheduled 8 week shutdown period.

Version	Tracks/event	Hits/track	Track efficiency ($\phi = 0$)	Tracks/primary vertex
p14.01.00	47.7	18.1	0.89	23.3
p13.06.01	35.3	16.0	0.71	12.3

Table 3.2: Table showing the improvement in tracking from p13 to p14 [49].

The members of the DØ collaboration already had access to substantial computing resources used for production of Monte Carlo events. The collaboration decided that the these resources should be appropriated for remote data reprocessing. This mode of operation posed several logistical difficulties:

- Each RAW event typically takes 250 kB of data. The DST reconstructed event takes up 150 kB. This amounts to 75 TB of input data which must be distributed over wide area networks to the computing centres, and 45 TB of produced data that must be permanently stored and made available for use by the collaboration.

- In addition to the DST file, the associated TMB file is produced. This condensed event has a size of ∼20kB. To ensure the efficient use of the SAM storage system, the small thumbnail files must be merged together with other files from the same dataset before storage into SAM.
- In Monte Carlo production events are generic, and any failed jobs can be discarded. This is not the case with reprocessing since every datafile is unique and so failed jobs must be recovered and restarted.
- This would be the first time that the reconstruction software was to be used "in production" offsite, and any dependencies on the FNAL environment had to be removed, and communication with central databases dealt with carefully.
- In order to ensure that the reprocessed dataset is consistent, the data produced by each remote sites must be monitored and certified.

3.6.1 Organisation

DØ software was preinstalled at each site using the UPS/UPD system. The data files were staged from the tapes at DØ using SAM. The workflow shown in Figure 3.4 was managed by the upgraded RunJob package. This executes each stage of reprocessing sequentially and tracks the metadata required for storage into SAM. It is configured locally at each site to correctly initialise the FNAL environment and to interface to the batch system.

Six groups contributed resources towards the reprocessing effort. Table 3.3 shows a breakdown of the centres and the number of CPUs provided. The 340 CPUs in the UK contribution were located in the London eScience Centre computing farm,

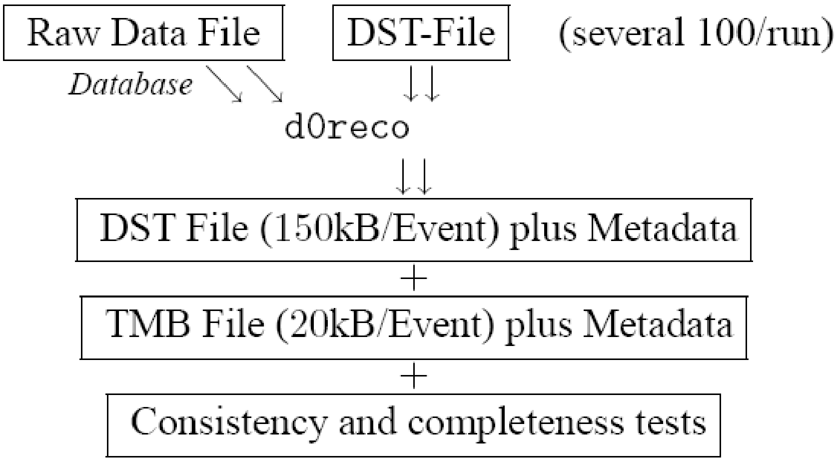

Figure 3.4: Workflow for reprocessing.

Centre	Location	Size (/1GHz PIII CPU equivalent)
GridKa	Karlsruhe, Germany	300
IN2P3	Lyon, France	220
Nikef	Amsterdam, Netherlands	80 local, 220 EDG
SAR	Texas, USA	130
UK	London, Rutherford, Manchester	340
WestGrid	Canada	300

Table 3.3: Computer centres which participated in the Winter 2004 reprocessing.

the Tier 1A farm at the Rutherford Appleton Laboratory (RAL), and the HEP farm at Manchester University. A detailed breakdown of the UK resources is shown in Table 3.4. The deployment of SAM and installation of the DØ software was made difficult by the fact that these resources were remote to the Imperial HEP group and "root" administrative privileges were unavailable.

Preliminary testing revealed that during bulk reprocessing the volume of calls to the central database at DØ was unworkable. This database holds the calibration constants in an Oracle[50] database, with 700,000 rows for the SMT, 100,000 rows for the CFT and 55,000 rows for the calorimeter. The problems arose because the caching system was optimised for reconstruction of a single physics run, and could

Site	Imperial	Manchester	Rutherford
CPU (1GHz PIII equivalent):	160	90	90
RAM/CPU:	512MB	1GB	512MB
SAM Cache:	100GB	300GB	1.2TB
Stageout disks:	300GB	300GB	420GB

Table 3.4: Breakdown of UK reprocessing resources.

not cope with requests for a range of runs over the wide area network.

It is possible to reprocess data from DST files using the calibrations recorded during the original reconstruction, without accessing the database. For this round of reprocessing the calibrations had not been significantly updated and so this mode of operation offered the best solution. The size of the DST format is smaller than the RAW format and so this had the additional benefit of reducing the amount of data to be transported to the remote sites by ∼30%. For future reprocessing rounds the problem was solved by increasing the cache of the central database and installing proxy databases at each reprocessing site.

3.6.2 Operation

It was originally intended that reprocessing could use the SAMGrid framework to submit and manage jobs. However it was clear that JIM release v1 was not yet ready for deployment to all remote centres, nor robust enough to deal with the heavy workloads involved. Instead local system administrators were responsible for the management and running of jobs at each site.

SAM datasets containing the sets of files to be reprocessed were produced manually at DØ and assigned to each site. Each dataset had at most one complete physics data run, with the number of files in dataset tailored to the disk and CPU resources at each site, e.g. each UK dataset contained around 200 files totalling 100 GB. These datasets were generally prestaged into local SAM caches before job submission to ensure that the necessary file was immediately available to a running job. The files for the UK datasets were staged to a SAM cache at RAL, which has a fast transatlantic link and the largest SAM cache (1.2 TB). At each site the local administrator submitted the reprocessing jobs using RunJob.

Upon completion of a dataset the thumbnail metadata files and job logs were transferred to DØ using a manual SAM copy command, which called GridFTP or a local copy mechanism. This was so that consistency checks could be applied at Fermilab before files were declared to the SAM database, merged and permanently stored. Most sites had sufficient permanent storage space to keep the DST files locally. However this was not the case for the UK sites and the produced DST files were stored back to FNAL using SAM.

Submission and management of jobs at the UK sites was performed with a set of shell and python scripts. A submission script set up the correct environment and submitted a dataset using RunJob. Another script was used to parse the output log files and check jobs had finished successfully. The list of successful jobs was then compared with the input dataset and if necessary a recovery dataset was generated. A third script initialised the storage of DST files into SAM and checked that file transfers were successful.

Job failures were a common occurrence. These were mainly due to inherent memory leaks in the DØ reconstruction software. This typically affected 5% of jobs, although the failure rate was as high as 20% for the highest luminosity datasets.

3.6.3 Certification

It was required that each of the participating sites be certified before production began. This involved reprocessing a predefined certification dataset which contained 66 files. The resulting data files and logs were sent to FNAL where they were analysed. Each file was compared with the corresponding file that had been reprocessed on the central farm, and with the file reconstructed from raw data. The data files contain time-stamps and logging information and so cannot be compared bitwise.

Instead the *RecoCert*[51] package was used. This produces various physics plots and is used to check new data as it is reconstructed. For the purposes of certification, site plots were overlayed onto reference plots from the central farm, and published on a website[52]. It was discovered that tiny differences between the output of sites occurred in certain plots. Examples can be seen in Figure 3.5. The cause of these differences was found to be the different treatment of floating point decimals by Intel Pentium processors in use at most centres and AMD Athlon processors used in the Manchester farm and a portion of the Nikhef farm. Experts ruled that these differences were insignificant to the physics results.

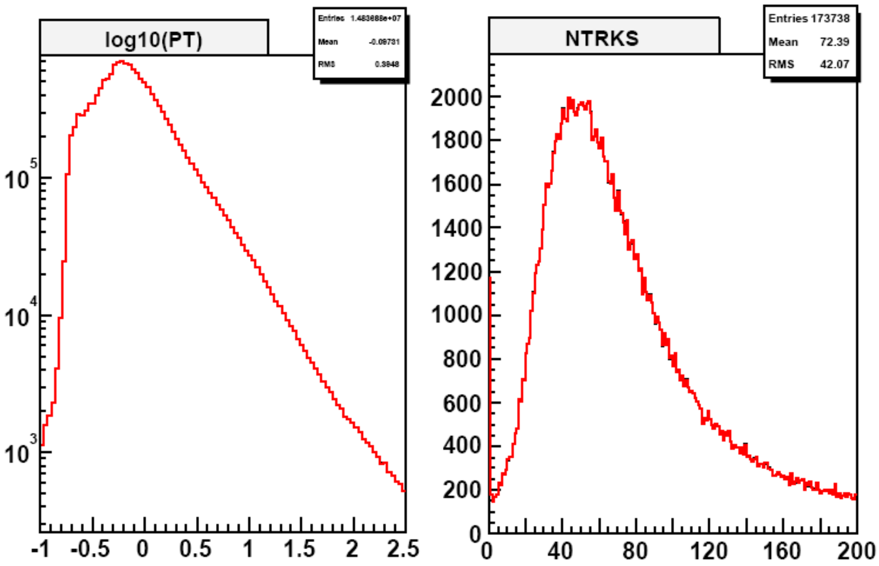

Figure 3.5: Overlay of RecoCert plots from Lyon (Red) and Manchester (Black). Plots overlap almost exactly, and experts ruled that the small differences which arose due to the CPU type used for reprocessing were negligible.

3.6.4 Results

The central reconstruction farm was available for reprocessing events during the Autumn shutdown beginning in September 2003. It was also able to contribute its spare capacity in the period immediately after the shutdown during the commissioning phase. The certification of sites began in November 2003 and reprocessing began at sites shortly afterwards. Reprocessing was completed in mid January with 300 M events totalling 45 TB of data had been processed. The five remote sites GridKa, IN2P3, Nikef, WestGrid and the UK farms all contributed significantly to the effort, reprocessing approximately 100 M events in total. The breakdown of the contributions is shown in Figure 3.6. The UK reprocessed 23 M events, corresponding to 5.4 TB of data and 11,500 files.

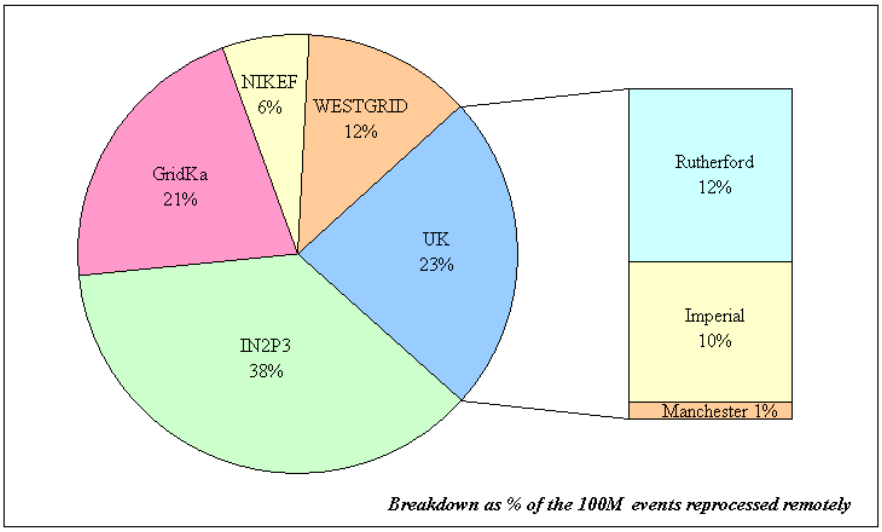

Figure 3.6: Pie chart showing the percentage of remotely reprocessed events at each site. In total 100 M events were reprocessed remotely.

3.7 *p*17 reprocessing

3.7.1 Preparation

Following the successful round of *p*14 reprocessing further work was performed on the farms managed by the Imperial HEP group in order to contribute to the *p*17 reprocessing from RAW [53] and Monte Carlo production using SAMGRID. This involved deploying and tailoring the updated SAM and JIM packages. In particular the SAMGrid batch adapter had to be written to interface to the Sun Grid Engine [54] (SGE) batch system used on the farm at the London eScience centre. The scripts translated the SAMGrid commands used to submit, query and delete jobs into corresponding SGE commands. This included processing the necessary input arguments and capturing any relevant output or error information resulting from the command. In addition a proxy database for the UK sites was installed and tested on the LeSC cluster.

3.7.2 Operation

The $p17$ reprocessing task used SAMGrid to submit and monitor reprocessing jobs. All sites used a common set of scripts to submit reprocessing jobs, initiate TMB merging, and recover failed jobs.

3.7.3 Results

Reprocessing took place between March and November 2005. In total ∼1000 M events were reprocessed, corresponding to ∼250 TB of data. The number of events reprocessed by each participating site is shown in Figure 3.7. Approximately 75% of events were reprocessed using off site using SAMGrid. In total 470 pb^{-1} of $p17$ data was produced. This doubled the size of the physics dataset available for analysis.

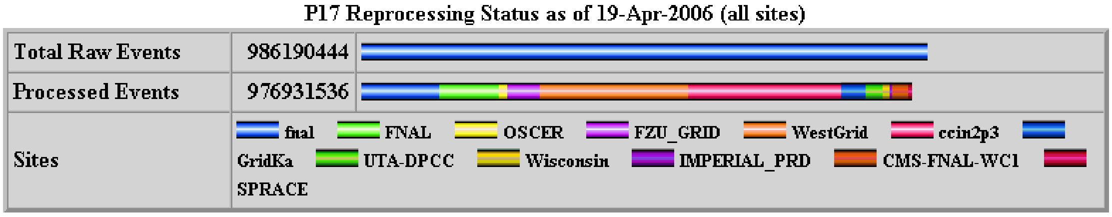

P17 Reprocessing Status as of 19-Apr-2006 (all sites)

Total Raw Events	986190444	
Processed Events	976931536	
Sites	🟦 fnal 🟩 FNAL 🟨 OSCER 🟪 FZU_GRID 🟧 WestGrid 🟥 ccin2p3 🟦 GridKa 🟩 UTA-DPCC 🟨 Wisconsin 🟪 IMPERIAL_PRD 🟧 CMS-FNAL-WC1 🟥 SPRACE	

Figure 3.7: Breakdown of the number of events reprocessed with $p17$ at each participating site.

3.8 Conclusions

3.8.1 Summary

The work on DØ distributed computing projects described in this thesis covered the period in which Grid software and technologies were making the transition from development to production tools. Imperial College has made significant contributions to the development of the SAMGrid packages, and was one of the first operational remote sites. The work performed to extend the job broking and monitoring facilities, and the development of the *Storemgr* tool demonstrated the ability to run full Monte Carlo production using SAMGrid.

The $p14$ data reprocessing project was successful. The certification of all sites was managed at Imperial College. In total 300 M events were reprocessed over a 6 week period, with 100 M of these processed remotely. This was the first time that the reconstruction software had been used for official production offsite. The UK sites installed and managed by Imperial College made a significant contribution reprocessing 23 M events. The experience gained in the $p14$ data reprocessing was an essential input to the $p17$ data reprocessing project. This round of data reprocessing used SAMGrid to submit and monitor reprocessing jobs, and a common set of scripts to manage production. In total 470 pb^{-1} was reprocessed. This corresponds to almost 1000 M events or 250 TB of data and is the largest grid project to date in the field of high energy physics.

The successful completion of $p17$ reprocessing marked the maturation of the SAMGrid technologies and it is now the default for all production activities. A second round of $p17$ reprocessing took place in February 2006 in order to apply corrections to the hadronic calorimeter calibrations. Seven sites processed a data set of 1.5 billion events over a five week period. SAMGrid has been used for the production of Monte Carlo data in bulk [55]. Testing is now taking place to use SAMGrid to run primary processing both onsite and remotely [56].

Chapter 4

B_d Mixing Analysis

The determination of the mixing frequency in neutral B_d^0 and B_s^0-meson systems provide important constraints on the elements of the CKM matrix. The mixing frequency of the B_d^0-meson has been well measured at the B-factories BaBar[57] and Belle[58]. However these experiments are unable to study the higher mass B_s^0-mesons, which at present are only produced in sufficient quantities at the Tevatron.

Performing a measurement of the B_d^0 mixing parameter is a valuable step in the development of a B_s^0 mixing analysis. The larger statistics and less rapid oscillations mean that the B_d^0 decays are an excellent proving ground to understand and calibrate the tagging algorithm and show that the sample composition and Monte Carlo inputs result in a measurement of Δm_d consistent with other measurements. This work has also been described in a DØ Note [59].

4.1 Sample selection

The B_d^0 mixing analysis was based around two decay channels[1]. The D^0-sample consisted mainly of B^0 mesons and was reconstructed from the decay channel $B \to \mu^+ \nu \bar{D}^0 X$ where $D^0 \to K^+ \pi^-$. The D^*-sample consisted mainly of charged B^+ mesons and was reconstructed from the related decay channel $B \to \mu^+ \nu \bar{D}^{*-} X$ where $\bar{D}^{*-} \to \bar{D}^0 \pi^-$ and $D^0 \to K^+ \pi^-$.

---

[1] The use of charge conjugates is implied thoughout this analysis.

The events in the D^0-sample were used in the construction of the flavour tagger. The D^*-sample was then used to make a statistically independent measurement of the flavour tag performance. The measured tagging performances for the B_u^+ and B_d^0 components were compared to verify that performance was independent of the reconstructed B-species and the Δm_d mixing parameter was found using a fit to the B_d^0 component across both samples.

The data set used totalled almost 1 fb^{-1} of data, which had been collected between April 2002 and October 2005. Approximately half of this data set had been reconstructed with version $p14$ software[60] and half with version $p17$ software[61]. The analysis was performed using the BANA[62] package. This is an extension of the DØ AATrack code[63], inspired by the B-physics analysis software used at the DELPHI experiment[65].

4.1.1 Selection cuts

The BANA package includes several sets of predefined selection cuts developed during previous DØ B-physics analyses. The cuts used in this analysis were based on the standard `SelectBD0Mu` BANA tight selection criteria for $B \to \mu^+ \nu \bar{D}^0 X$ events. The use of the standard selection cuts means that the analysis will be easily reproducible for future studies of novel flavour taggers.

The `SelectBD0Mu` selection procedure is as follows:

- The event must contain a muon candidate classed “loose” or better by the DØ muon identification code[66] which passes the kinematic cuts $P_T^\mu > 2$ GeV, $P^\mu > 3$ GeV, and $|\eta| < 2$.
- The tracks in these events were clustered into jets using the DURHAM[67] algorithm. Events were rejected if the jet containing the candidate muon also contained additional muon candidates.

- The BANA `SelectJPsi` code was used to search for $J/\psi \to \mu^+\mu^-$ decays. Events were containing any such J/ψ candidates were rejected.

- $D^0 \to K\pi$ vertex candidates were constructed using pairs of particles drawn from the muon jet. The two particles were required to have opposite charge and pass the kinematic cuts $P_T > 0.7$ GeV and $|\eta| < 2$.

- The axial (ϵ_T) and stereo (ϵ_L) projections of the track impact parameter with respect to the primary vertex were calculated for the both tracks. These were required to pass the cut $\sqrt{(\epsilon_T/\sigma(\epsilon_T))^2 + (\epsilon_L/\sigma(\epsilon_L))^2} > 2$.

- The K and π tracks were used to form a common D-vertex. This was required to have a χ^2-fit < 9. The assignment of the K and π masses was made with reference to the candidate muon charge, in accordance with the requirement that the $\mu^+K^+\pi^-$ system or its charge conjugate was formed.

- The distance in the transverse plane from the primary vertex to the D-vertex ($D_T^{PV\to D}$) and its associated error were measured. These were required to satisfy $\sigma(D_T^{PV\to D}) < 500\ \mu$m and $D_T^{PV\to D} > 4\cdot\sigma(D_T^{PV\to D})$. The angle ($\alpha_T^D$) in the axial plane between the D^0 momentum and the direction from the primary to D-vertex was required to satisfy $\cos(\alpha_T^D) > 0.9$.

- The muon and D^0 candidate were combined to form a common B-vertex candidate. This was required to have a χ^2-fit < 9. The mass and momentum of the B-candidate was estimated using the muon and reconstructed D^0-candidate. This mass was required to fall within the range $2.3 < M(\mu^+\bar{D}^0) < 5.2$ GeV.

- The distance in the transverse plane from the primary vertex to the B-vertex ($D_T^{PV\to B}$) was calculated. In the case that $D_T^{PV\to B} > 4\cdot\sigma(D_T^{PV\to B})$ an additional cut was made on the angle (α_T^B) in the axial plane between the direction from the primary to B-vertex and the B-candidate momentum: $\cos(\alpha_T^B) > 0.95$.

- The distance in the transverse plane between the primary and B-vertex ($D_T^{PV\to B}$) was required to be less than the transverse distance between primary and D-vertex ($D_T^{PV\to D}$) only if the precision of the vertex positions was such that, $D_T^{B\to D} < 3\cdot\sigma(D_T^{B\to D})$, where $D_T^{B\to D}$ is the measured transverse distance from the B- to D-vertex.

In addition to these cuts, a requirement that $P_T^{D^0} > 5$ GeV was made. This reduced the level of background and enabled the re-use of sample composition studies made in the B^0/B^+ lifetime ratio analysis [68]. The set of selected events was then subdivided into the D^0- and D^*-samples.

D^*- and D^0-sample selections

To form the D^*-sample a search was made for an additional pion candidate resulting from the $D^{*-} \to D^0\pi^-$ decay. This was required to have opposite charge with respect to the muon candidate and $P_T^{\pi} > 0.18$ GeV. If such a candidate was present it was combined with the D^0 candidate to form a D^{*-} candidate. The mass difference between the reconstructed D^{*-} and D^0 masses $\Delta M = M(\bar{D}^0\pi) - M(\bar{D}^0)$ is shown in Figure 4.1. The events in the signal region $0.1425 < \Delta M < 0.1490$ GeV formed the D^*-sample. All other events formed the D^0-sample.

The $K\pi$ mass distribution for each sample is shown in Figures 4.2 and 4.3. The D^0-sample contained 230551±1627 events, and the D^*-sample contained 73532±304 events.

4.2 Flavour tag construction

The initial flavour of the reconstructed B-meson at production can be tagged using “same side” or “opposite side” tags:

Same side tagging methods reconstruct tracks from the primary vertex which are associated with the production of the reconstructed B-meson. The initial flavour of

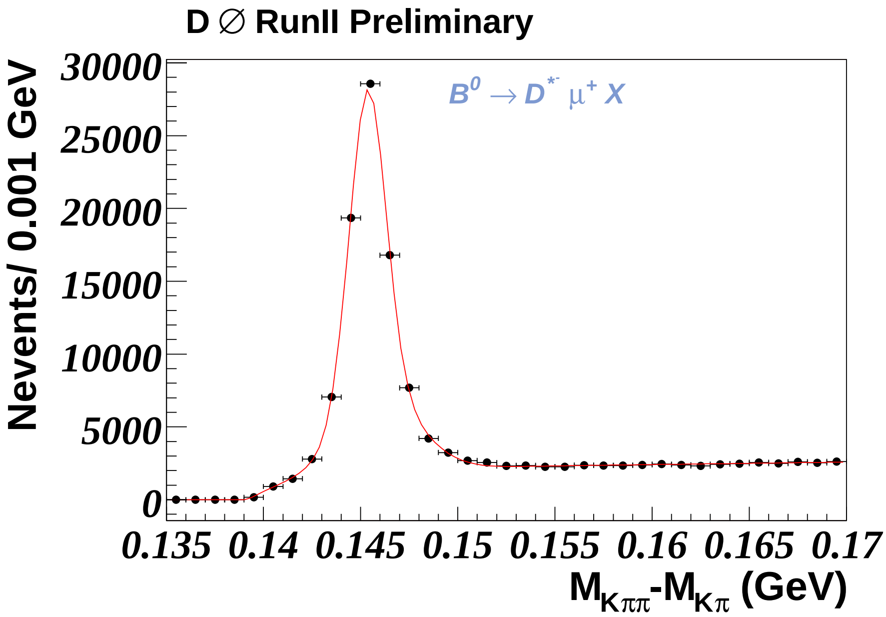

Figure 4.1: The $K\pi\pi - K\pi$ invariant mass for selected μD^* candidates. The curve shows the result of the fit with a double Gaussian signal, and exponential plus linear background function.

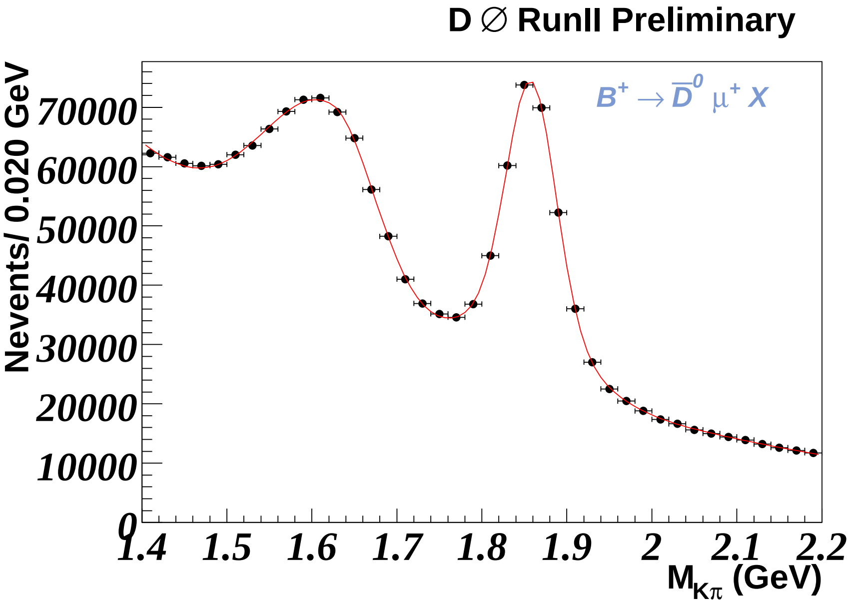

Figure 4.2: The $K\pi$ invariant mass for selected μD^0 candidates. The curve shows the result of the fit described in Section 4.3.1.

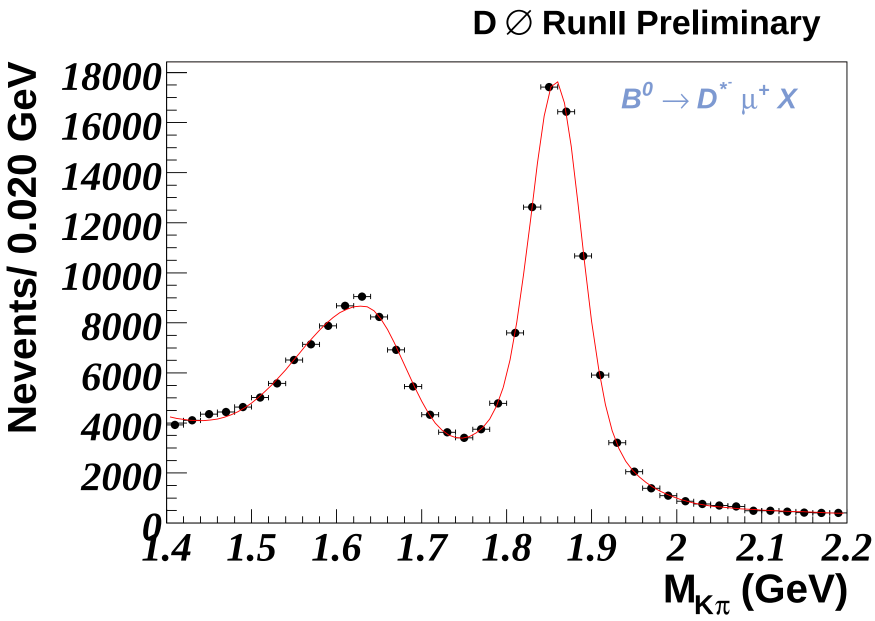

Figure 4.3: The $K\pi$ invariant mass for selected μD^* candidates. The curve shows the result of the fit described in Section 4.3.1.

the B-meson at production can be determined from the first particle in the fragmentation chain or from the decay products of an excited B^{**} state. The properties of the tag particle are specific to each reconstructed B-meson species, therefore same side tags have to be tailored individually for each B-species. This makes same side tags difficult to implement.

Opposite side tagging methods utilise the fact that all b-quarks are produced as part of a $b\bar{b}$-quark pair and so a B-hadron with opposite flavour will be produced on the "opposite side" of the event. The majority (∼90%) of B-hadrons are the same flavour at production and decay, and so reconstructing the flavour of opposite side B-hadron at decay provides a strong indication of the initial flavour of the reconstructed B-meson. Hadronisation of the $b\bar{b}$ quark pair is independent in $p\bar{p}$ collisions, so the performance of opposite side tag variables should be identical for B^+, B_d^0 and B_s^0 decays. This principle enables the application of studies made on B^+ and B_d^0 decays to B_s^0 analyses.

The combined flavour tagger constructed in this analysis uses opposite side tagging methods. In the challenging environment typical of a hadron collidors a full reconstruction of the opposite side B-hadron decay is impossible. Instead the opposite side flavour is estimated using discriminating variables associated with an identified $b \rightarrow l^-$ lepton candidate or secondary vertex candidate.

4.2.1 The likelihood ratio method

The tag variables were combined to form the combined flavour tagger using the "likelihood ratio" method.

Consider a set of discriminating variables X_i which each obey different distributions according to the initial b-flavour. For a given value of X_i the two distributions can be compared to evaluate the probability P_b^i of an initial b-flavour, and the probability $P_{\bar{b}}^i$ of an initial $\bar{b}$-flavour. In order to combine the information from different tag variables the likelihood ratio (R^i) calculated as the ratio of these probabilities is considered:

$$R^i = \frac{P_b^i}{P_{\bar{b}}^i} = \frac{P_b^i}{1 - P_b^i} \tag{4.1}$$

where R^i takes values between 0 (when $P_b^i = 0$) and ∞ (when $P_b^i = 1$).

For statistically independent tag variables the combined likelihood ratio (R) is equal to the product of the individual likelihood ratios:

$$R = \prod_{i=1}^{n} R^i \tag{4.2}$$

It is useful to convert R to the variable d:

$$d = \frac{1 - R}{1 + R} \tag{4.3}$$

where d takes values between -1 (when $P_b = 0$) and 1 (when $P_b = 1$). The most probable flavour is indicated by the sign of d, such that negative values imply initial b-flavour and positive values imply initial $\bar{b}$-flavour. The probability of a mistag is correlated to the magnitude of $|d|$ such that higher values imply greater tagging accuracy. For the idealised case in which there are no correlations between the tagging variables and perfect modeling of each X_i distribution, d corresponds to the tag dilution $\mathcal{D}$ defined as,

$$\mathcal{D} = \frac{n^{correct} - n^{wrong}}{n^{correct} + n^{wrong}} \tag{4.4}$$

where $n^{correct}$ is the number of events tagged correctly, and n^{wrong} is the number of events tagged incorrectly.

The significance of a frequency measurement for a B^0 mixing analysis is dependent on the following relation [69] :

$$\text{Significance} = \sqrt{\frac{S\varepsilon D^2}{2}} e^{-\frac{(\Delta m_d \sigma_\tau)^2}{2}} \sqrt{\frac{S}{S+B}} \tag{4.5}$$

Here S is the number of signal events, B is the number of background events, Δm_d is the B_d^0 mixing frequency, σ_τ is the proper time resolution, D is the tag dilution and ε is the efficiency to tag events:

$$\varepsilon = \frac{n^{tagged}}{n^{total}} \tag{4.6}$$

where n^{total} is the total number of events and n^{tagged} is the number of tagged events. In order to compare the performance of different flavour tagging methods the value $\varepsilon\mathcal{D}^2$ is often quoted.

4.2.2 Construction of probability distributions

Events drawn from the D^0-sample of events were used to construct probability density functions (PDFs) associated with each flavour discriminating variable. In order to accurately model the distributions it is necessary to select a set of non-oscillating events in which both the initial and final flavours are known. The D^0-sample consists mainly of non-mixing charged B^+-mesons, but there is also a significant fraction (∼16%) of neutral B_d^0 mesons[2]. In order to suppress the fraction of mixed decays, only events in the short VPDL region between 0 and 500 μm were used. A Monte

---

[2] see Section 4.3.2 for sample composition study.

Carlo study estimated that for these events the initial flavour is correctly determined in $(98 \pm 1)\%$ of cases, where the error is associated to the uncertainty in the B-decay branching rates.

A "signal-band" sample was constructed using events from the D^0-sample with $1.80 < M(K\pi) < 1.92$ GeV. The PDFs constructed from this sample contain contributions from both signal and background events. To extract the PDF for signal events only the contribution from background events was subtracted. This was performed using a sample of "side-band" events taken from the region $1.94 < M(K\pi) < 2.22$ GeV. This set of events contains purely background events and was used to construct the background PDFs. The relative number of background events in the signal- and side-bands was determined using an equivalent mass fitting procedure to that described in Section 4.3.1.

4.2.3 Discriminating variables

Two types of opposite side flavour tags were used:

- The "lepton tags" tag opposite side B-hadrons which undergo semileptonic decays where $b \to l^-$ and $\bar{b} \to l^+$. The total branching ratio for $B \to l^+ \nu_l X$ is $\sim 20\%$, where 10% of decays are to electrons and 10% of decays are to muons.
- The "secondary vertex" and "event charge tags" are applicable to secondary vertex decays. These estimate the opposite side flavour using momentum weighted summed charges of opposite side tracks.

Same side tracks associated with the reconstructed B-meson were excluded in the construction of all tag variables. This was achieved by removing all daughter particles used to reconstruct the B-candidate and any tracks contained within the cone $\cos[\phi(\mathbf{P}^i, \mathbf{P}^B)] > 0.8$, where $\mathbf{P}^i$ and $\mathbf{P}^B$ are the 3-momentums of the ith candidate track and the reconstructed B-candidate respectively.

Muon jet charge

The muon jet charge was constructed for those events containing an additional muon candidate. These candidates were required to satisfy the following cuts:

- $\cos[\phi(\mathbf{P}^{\mu}, \mathbf{P}^{B})] < 0.8$, where $\mathbf{P}^{\mu}$ and $\mathbf{P}^{B}$ are the momentum of tag muon and B-candidate respectively.
- be designated “loose” or better by the reconstruction algorithm.
- have hits in at least one layer of the muon system.

The directional cut ensures that daughter particles of the reconstructed B-meson are not included. The other cuts are on the quality of the candidates, made to suppress the number of fake muons found. It was not necessary to make tight selection cuts at this stage, since the likelihood ratio method assigns a relative weight based on the tag quality of each tagged muon.

If more than one muon was found to pass the above cuts, the candidate with hits in the most layers of the muon system was chosen. In the case that two or more muons had hits in the same number of layers, the muon with greatest absolute transverse momentum was chosen.

The jet of particles around the selected muon was constructed using opposite side tracks which satisfied the requirement:

$$\Delta R = \sqrt{(\Delta\phi)^2 + (\Delta\eta)^2} < 0.5 \tag{4.7}$$

where $\Delta\phi$ and $\Delta\eta$ refer to the angles between the candidate track and tag muon momenta. The *muon jet charge* or Q_J^{μ} was then calculated:

$$Q_J^{\mu} = \frac{\sum_i q^i P_T^i}{\sum_i P_T^i} \tag{4.8}$$

where the sum was taken over all tracks including the tag muon, in the muon jet.

Separate distributions for Q_J^μ were made for muons with hits in all layers of the muon system (*NSEG*= 3 muons) and those which did not register in every layer (*NSEG*< 3 muons). This was because the number of fake muons is considerably greater in the set of *NSEG*< 3 muons and so tagging dilution is worse.

Electron jet charge

The electron jet charge was calculated for events which contained a candidate electron. The identification of the low P_T electrons which result from semileptonic B-decay was performed using a "road" method[70]. Candidate tracks identified in the central tracking system were extrapolated into the calorimeter, and the energy deposited along a narrow "road" around this track was considered.

The candidate electron tracks had to satisfy the following cuts:

- at least one hit in the SMT
- $|\eta| < 1.1$
- $P_T^e > 2.0$ GeV
- $\cos\phi(\mathbf{P}^e, \mathbf{P}^B) < 0.5$

The variables E/P and EMF were then used to discriminate between the signal electrons and background tracks. E/P is defined as the ratio of transverse energy (E_T) measured in first three layers of the calorimeter to the measured P_T of the track. EMF is defined as the ratio of the E_T deposited in first three calorimeter layers to the summed E_T deposited in all layers. The distributions of E/P and EMF are dependant on the P_T^e and so the candidates were divided into "high" and "low" P_T samples using a cut at 3.5 GeV. Different cuts on E/P and EMF were made, such that the ratio of signal electrons to background tracks was the same for both samples:

- for electrons $P_T^e < 3.5$ GeV:
  $EMF > 0.8, \quad 0.55 < E/P < 1.0$
- for electrons $P_T^e > 3.5$ GeV:
  $EMF > 0.7, \quad 0.5 < E/P < 1.1$

The DURHAM algorithm was then used to group all tracks in the event into jets. If more than one electron candidate was found, the candidate with the largest P_T^e measured relative the summed momentum of the surrounding jet was used. In the case that no electrons were associated with a jet, the electron which had the greatest absolute P_T^e was selected. For the tag electron the *electron jet charge* or Q_J^e was calculated:

$$Q_J^e = \frac{\sum_i q^i P_T^i}{\sum_i P_T^i} \tag{4.9}$$

Secondary Vertex Charge

The secondary vertex charge was calculated for events in which a candidate for the displaced B-decay vertex on the opposite side was identified. The secondary vertex finder formed candidate vertices from each possible pair of tracks, rejecting those with a χ^2-fit > 4. For each of the remaining candidates a search was made for additional daughter tracks. Each track was added into the vertex individually, and the track causing the least increase to the χ^2-fit was identified; if this increase satisfied $\Delta\chi^2 < 5$ the track was added into the vertex; this process was repeated until all eligible tracks were incorporated into the vertex.

Each secondary vertex candidate was then subject to the following requirements:

- two tracks with axial impact parameter $\epsilon_T > 3 \cdot \sigma(\epsilon_T)$
- transverse distance from primary to secondary vertex $D_T^{PV\rightarrow SV} > 4{\cdot}\sigma(D_T^{PV\rightarrow SV})$.
- $\cos\phi(\mathbf{P}^{SV}, \mathbf{P}^B) > 0.8$, where $\mathbf{P}^{SV}$ is the summed momentum of each track in the secondary vertex candidate and $\mathbf{P}^B$ is the reconstructed momentum of the B-candidate.

The *secondary vertex jet charge* or Q_{SV} was calculated using all tracks forming secondary vertex candidates:

$$Q_{SV} = \frac{\sum_i (q^i P_L^i)^k}{\sum_i (P_L^i)^k} \tag{4.10}$$

where P_L^i is the longitudinal momentum component of the ith track with respect to the direction of the summed secondary vertex momentum. The value $k = 0.6$ was used. This was taken from the flavour tag studies at LEP[71], and confirmed by a study of the discriminating performance over a range of k, illustrated in Figure 4.4.

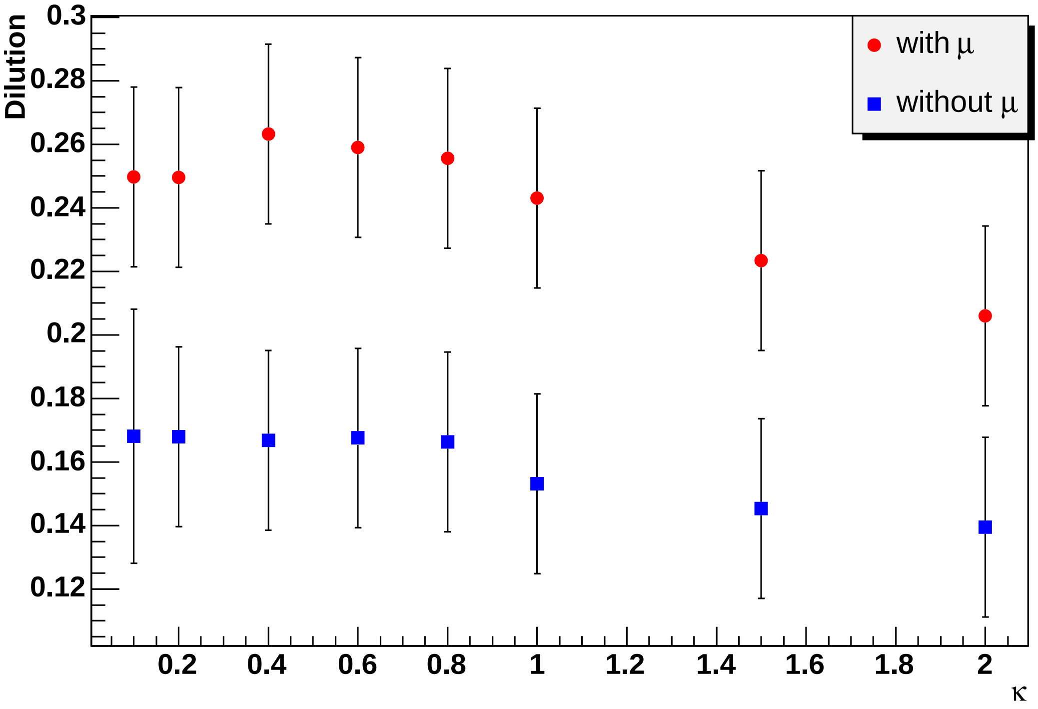

Figure 4.4: Dilution of events tagged by Q_{SV} versus the coefficient k. Distribution shown for events which included a muon tag candidate (red circles) and those without a muon tag candidate (blue squares). The statistical errors shown for different k coefficients are correlated.

Event Charge

The *event charge* or Q_{EV} was calculated as the P_T weighted charge sum over all opposite side tracks with $0.5 < P_T < 50$ GeV.

$$Q_{EV} = \frac{\sum_i q^i P_T^i}{\sum_i P_T^i} \tag{4.11}$$

This variable possesses a weak discriminatory power, but is still able to improve tagging performance, particularly in the absence of an opposite side lepton candidate.

Combining tags

The combined tagger was formed by combining the individual tag likelihood ratios according to the following prescription:

- If a muon candidate is found the muon jet charge Q_J^μ is used. If a secondary vertex candidate is found, the likelihood is combined with the secondary vertex charge Q_{SV}.
- If no muon candidate is present but an electron candidate found, the electron jet charge Q_J^e tag is used. If a secondary vertex candidate is found, the likelihood is combined with the secondary vertex charge Q_{SV}.
- If no muon or electron candidates are found, but a secondary vertex candidate is present, the secondary vertex Q_{SV} tag is used in conjunction with the event charge Q_{EV} tag.

4.2.4 Results

The signal event PDFs for the tag variables are shown in Figures 4.5 and 4.6. The distributions for events with reconstructed b- and $\bar{b}$-flavours are drawn separately. The error on each point arises from the limited statistics, for clarity these are only shown for the b-flavour PDFs. The likelihood ratio R is calculated as the ratio of the b- and $\bar{b}$-flavour PDFs at a given tag value.

For all tag variables the distributions for reconstructed b- and $\bar{b}$-flavours differ significantly. Artifacts can be seen at ±1.0 in the lepton jet charge and secondary vertex charge PDFs. These are caused by events in which all tracks in the jet charge sum have identical charge. Figures 4.5 (a) and (b) show the muon jet charge PDFs for $NSEG = 3$ and $NSEG < 3$ muons. The jet charge for $NSEG = 3$ muons has much better discriminatory power, as expected since this sample contains fewer fake muons.

The resulting PDF for the combined tag variable d is shown in Figure 4.7. The shape of the distribution arises from the combination of the separate likelihood ratios; the peaks in the combined tagging variable at ±0.4 result from the artifacts at ±1.0 in the individual tag PDFs.

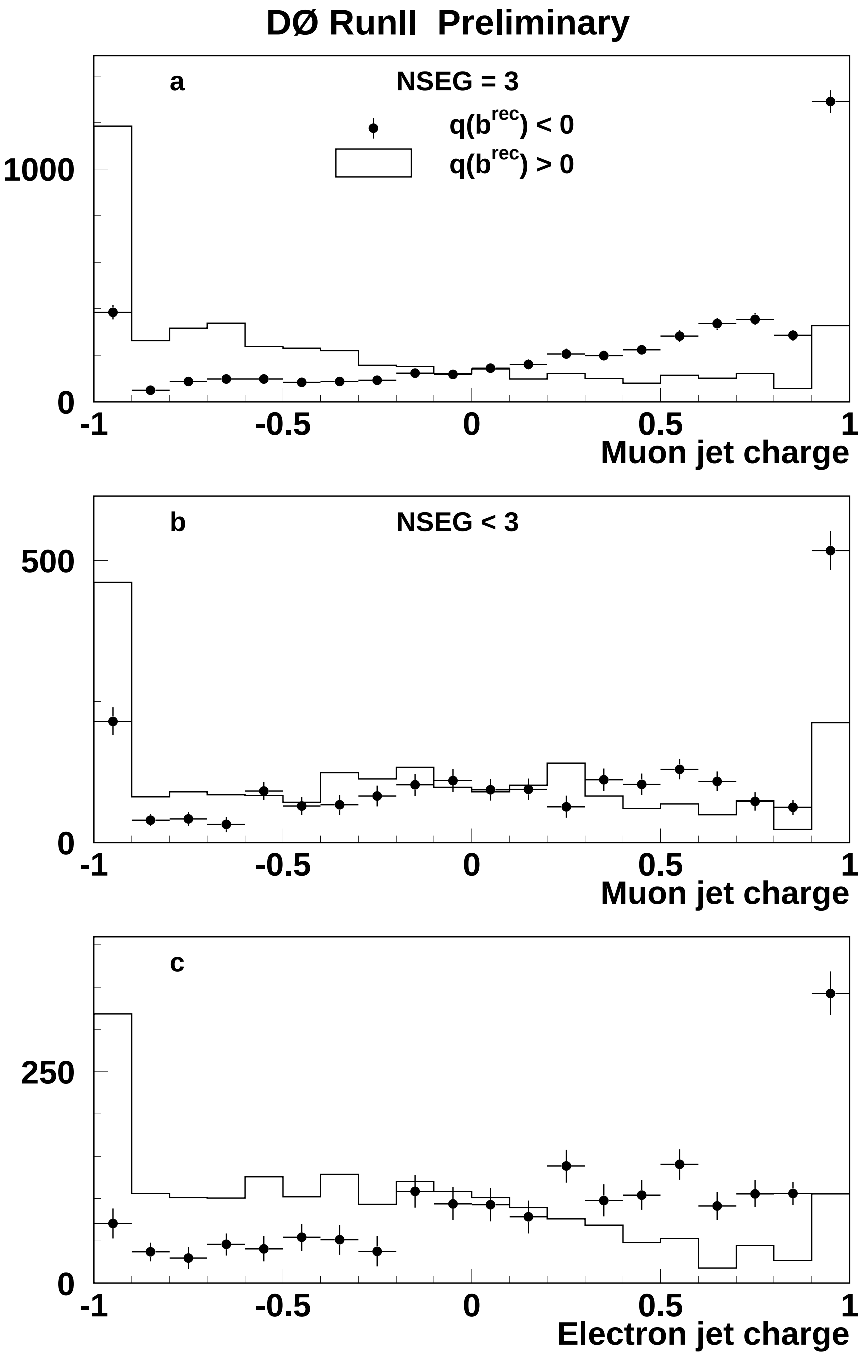

Figure 4.5: a) Distribution of muon jet charge for muons with $NSEG = 3$. b) Distribution of muon jet charge for muons with $NSEG < 3$. c) Distribution of electron jet charge. The $q(b^{rec})$ is the charge of the b quark from the reconstruction side. The tag variable distributions for events with reconstructed b-flavour (drawn as points) and $\bar{b}$-flavour (drawn as a histogram) should be symmetrical within statistical fluctuations, and the ratio of the distributions at each point is used to calculate the likelihood ratio R.

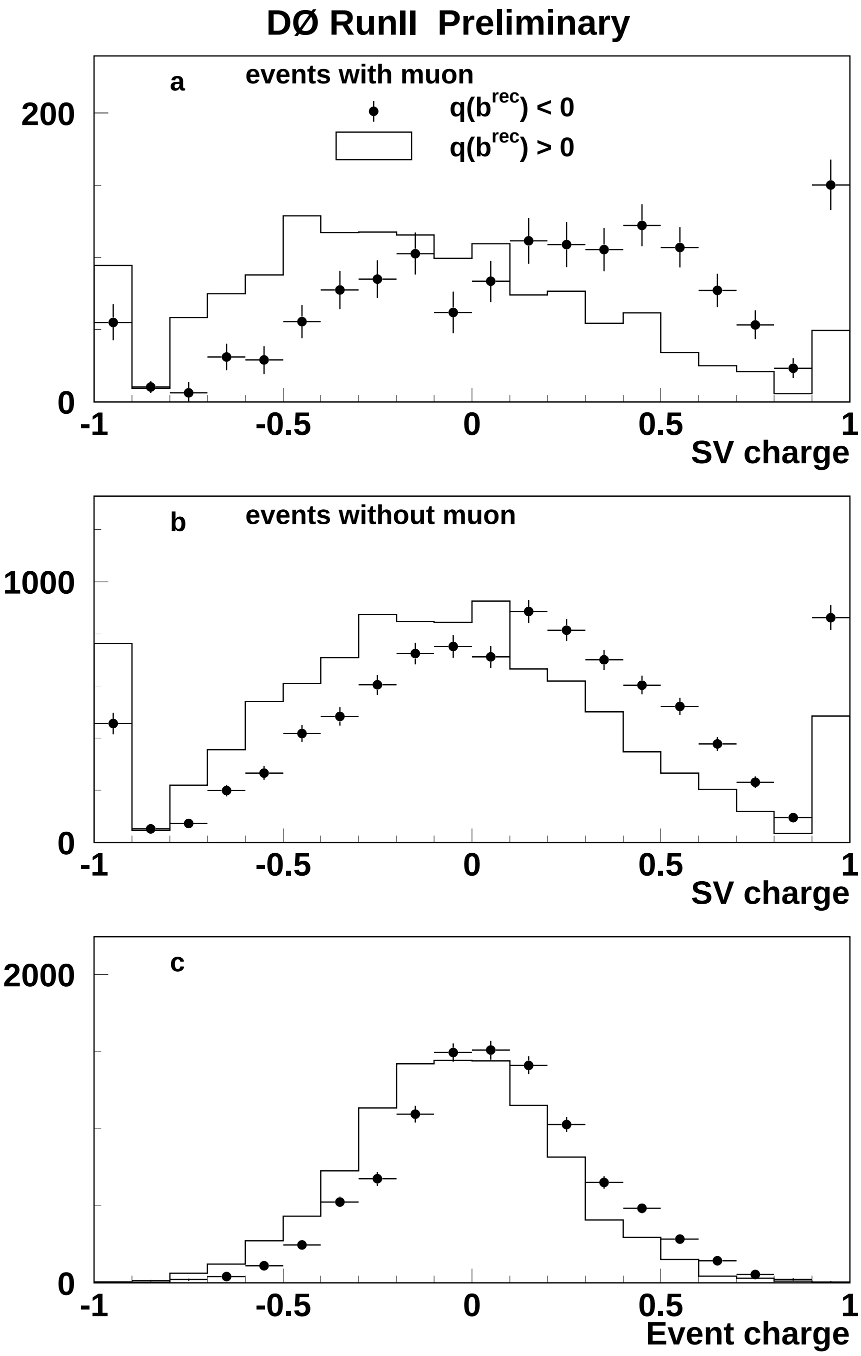

Figure 4.6: a) Distribution of secondary vertex charge for events with muon. b) Distribution of secondary vertex charge for events without muon. c) Distribution of event jet charge. The $q(b^{rec})$ is the charge of the b quark from the reconstruction side. The tag variable distributions for events with reconstructed b-flavour (drawn as points) and $\bar{b}$-flavour (drawn as a histogram) should be symmetrical within statistical fluctuations, and the ratio of the distributions at each point is used to calculate the likelihood ratio R.

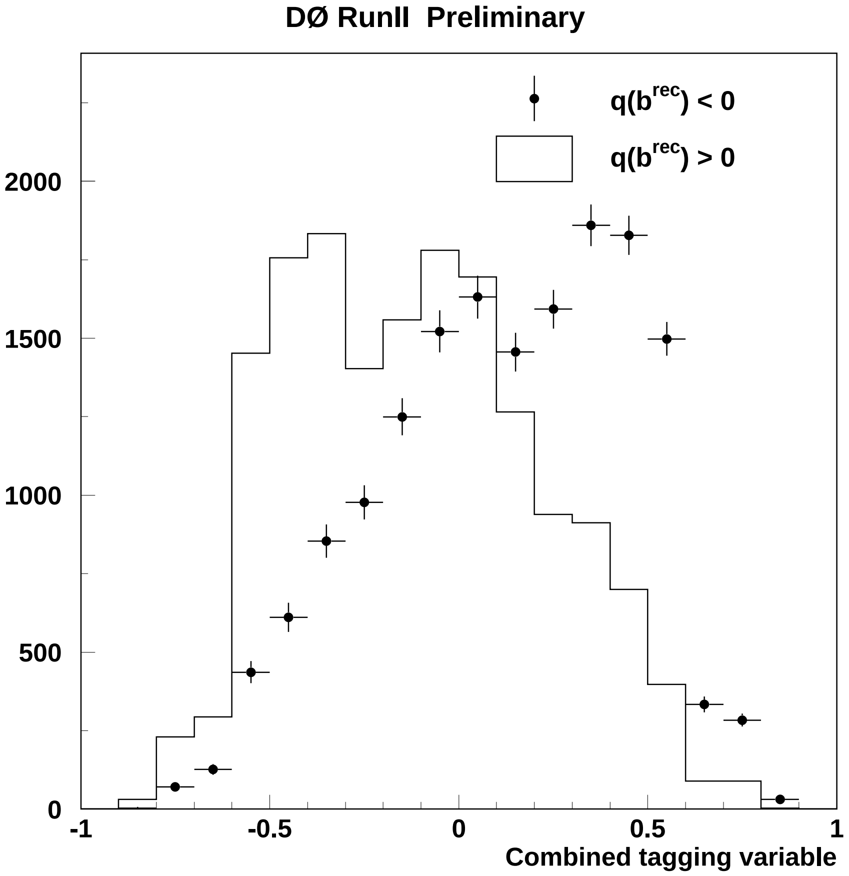

Figure 4.7: Normalised distributions of the combined tagging variable. The $q(b^{rec})$ is the charge of the b quark from the reconstruction side. The clear separation of the two distributions illustrates the power of the combined tag to discriminate between events with b- and $\bar{b}$-flavour.

4.3 B_d^0 mixing analysis

The measurement of Δm_d and tag performance is made using a binned likelihood fit of the flavour asymmetries as a function of VPDL (visible particle decay length). Each data sample is divided into seven VPDL bins and tagged using the combined flavour tagger. The number of tagged oscillated N^{osc} and tagged non-oscillated N^{nos} events in each bin is found by fitting to the $K\pi$ mass distributions. These are then used to calculate flavour asymmetry (A_i) in the ith VPDL bin.

$$A_i = \frac{N_i^{nos} - N_i^{osc}}{N_i^{nos} + N_i^{osc}}, \tag{4.12}$$

The procedure to fit the $K\pi$ mass distributions is described in section 4.3.1. The set of asymmetry measurements is then fitted using the procedure described in Section 4.3.2.

4.3.1 Mass fitting procedure

Development of the fit function

The distribution of $M(K\pi)$ for events in the D^0-sample is shown in Figure 4.2. The choice of fitting function was made to optimise the χ^2-value of a fit to the full D^0-sample. The $K\pi$ mass distribution consists of three components: the D^0 signal peak at ∼1.85 GeV, a background peak at ∼1.6 GeV and the combinatorial background which falls off approximately exponentially across the region considered.

Several different functions to fit the signal peak were assessed. The results of this study are shown in Table 4.1. The best fit to the signal peak was provided by a double Gaussian function without a constraint that both Gaussians share the same mean.

The peak in background in the lower mass region corresponds to decays in which $D^0 \to K\pi X$, where X is not included in the D^0 reconstruction. This peak was studied using Monte Carlo data. Two samples of $B_d^0 \to \mu^+\nu\bar{D}^0X$ decays were

Fit function	$N^{sig}/1000$	μ/GeV	Chi-squared	degrees of freedom
Single Gaussian	210.5 ± 0.8	1.8571±0.0001	769	31
Double Gaussian means constrained	226.0±1.0	1.8569±0.0001	117	29
Double Gaussian means free	230.5 ± 0.9	1.8676±0.0017 1.8487±0.0017	57	28

Table 4.1: Table showing the Chi-squared of different fits to the $B^+ \rightarrow \mu^+\nu\bar{D}^0 X$ signal peak at 1.85GeV. The background fit functions are taken from Equations 4.15 and 4.16

generated, one in which $D^0 \rightarrow K\pi$ and one in which $D^0 \rightarrow K\pi\pi^0$. The reconstructed $K\pi$ invariant mass distributions for both samples are shown in Figure 4.8. The position of the $D^0 \rightarrow K\pi\pi^0$ signal peak in simulated Monte Carlo events corresponds closely to the background peak observed in the D^0-sample. It is also apparent that the peak is asymmetrical. A bifurcated Gaussian function (Equation 4.16) was found to provide the best fit to the background peak in data.

Results

The result of the studies was the following functional form:

$$\begin{aligned}
f &= f^{sig} + f_1^{bkg} + f_2^{bkg} && (4.13)\\
f^{sig} &= A \cdot \frac{(1+R)}{2} \exp\left(-\frac{(x-\mu_1)^2}{2\sigma_1^2}\right) + && (4.14)\\
& \quad A \cdot \frac{(1-R)}{2} \exp\left(-\frac{(x-\mu_2)^2}{2\sigma_2^2}\right) \\
f_1^{bkg} &= a_0 \cdot \exp\left(-\frac{x}{b_0}\right) && (4.15)\\
f_2^{bkg} &= N_0 \cdot \exp\left(-\frac{(x-\mu_0)^2}{2\sigma_R^2}\right) \quad \text{for} \quad x-\mu_0 > 0.0 && (4.16)\\
&= N_0 \cdot \exp\left(-\frac{(x-\mu_0)^2}{2\sigma_L^2}\right) \quad \text{for} \quad x-\mu_0 < 0.0
\end{aligned}$$

The signal peak (f^{sig}) is described by two Gaussians with six parameters: μ_1 and μ_2 are the means, σ_1 and σ_2 are the widths, R lies in the range {-1,1} and controls the relative contributions between the two Gaussians, and A is related to the number

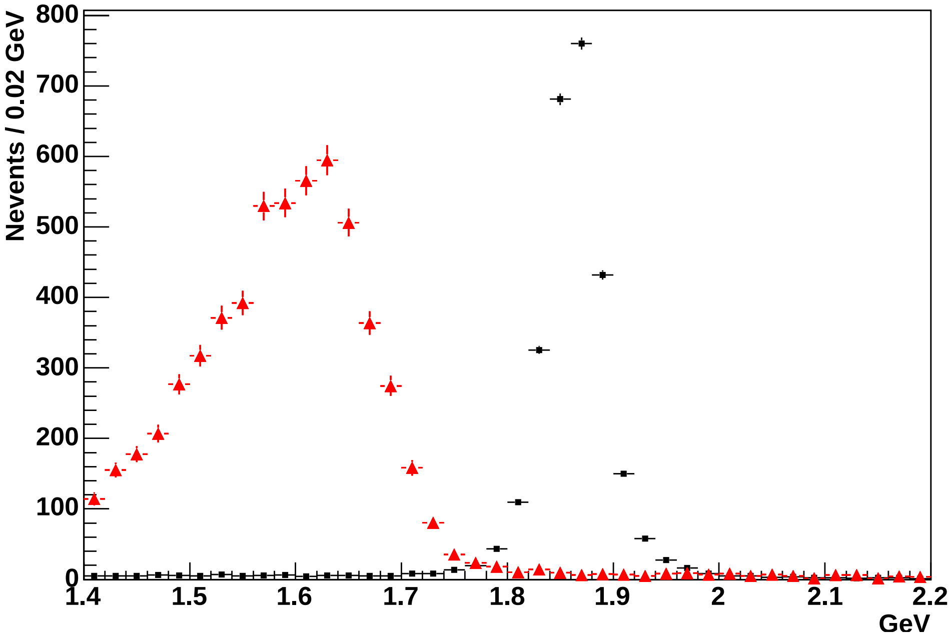

Figure 4.8: The $K\pi$ invariant mass for reconstructed $B \rightarrow \mu D^* X$ Monte Carlo events. The square black markers correspond to events in which $D^0 \rightarrow K^+\pi^-$. The triangular red markers correspond to events in which $D^0 \rightarrow K^+\pi^-\pi^0$.

of signal events N^{sig} according to:

$$A = \frac{N^{sig}\sqrt{2/\pi}}{(1+R)\sigma_1 + (1-R)\sigma_2} \tag{4.17}$$

The exponential background (f_1^{bkg}) is described by the decay constant b_0 and a normalisation constant a_0. The peaking background (f_2^{bkg}) is described by a bifurcated Gaussian with four parameters: μ_0 is the mean, σ_L and σ_R are the widths, and N_0 is the normalisation constant.

Constraining the fit function

The chosen fit function has twelve free parameters. The large statistics of the D^0- and D^*-samples mean that fitting the full distributions with this function is straightforward. However the mixing analysis requires that the fit must be applied to several sub-samples of the full data set. The full samples contain $\sim \mathcal{O}(100,000)$ events; once the sample has been divided according to VPDL interval and the result of flavour tagging there can be as few as $\sim \mathcal{O}(100)$ events. This corresponds to an increase in the level of expected statistical fluctuations from 0.3% to 10%.

The problem of fitting such sub-samples robustly was solved by constraining the fit parameters using values taken from a fit to the full statistic sample. In order to demonstrate that this process would not bias the results, a study was made investigating the dependance of the fitted parameter values on the VPDL interval and the result of flavour tagging. This involved making free fits to sub-samples of events and comparing the result with the reference fits made to the full statistic samples.

VPDL dependence

The dependance of the fit parameters on visible particle decay length (VPDL) was studied using all events (without applying flavour tagging). These were divided into the seven VPDL bins used in the asymmetry fit {-0.025, 0, 0.025, 0.05, 0.075, 0.1, 0.125, 0.25}.

Flavour tag dependence

The dependance of the fit parameters on the result of the flavour tag was studied using four samples:

- all tagged events with $|d| > 0.3$.
- all untagged events.
- events tagged mixed with $|d| > 0.3$ in VPDL region $0 < x^M < 0.05$.
- events tagged unmixed with $|d| > 0.3$ in VPDL range $0 < x^M < 0.05$.

The majority of events in the VPDL interval {0,0.05} are unmixed. Therefore the tagged unmixed/mixed samples from this region should highlight any differences in the parameters for events which have been tagged correctly/incorrectly. Such differences are possible because the act of flavour tagging increases the sample purity. This is because background events are less likely to contain an “opposite side” B-hadron which can be tagged.

Fitted parameters

The fitting function contains three parameters (A, N_0 and a_0) which control the magnitude of the three component functions (f^{sig}, f_1^{bkg} and f_2^{bkg}). The remaining parameters control the shape of the function. For the fit study the widths of the double signal Gaussian and bifurcated background Gaussian were recast with "average" and "difference" width terms. This was so that any trend in the shape could be more easily identified. The fitted parameters were then:

$$b_0, \quad \mu_0, \; \frac{\sigma_R + \sigma_L}{2}, \; \frac{\sigma_R - \sigma_L}{\sigma_R + \sigma_L}, \quad \mu_1, \; \frac{\sigma_1 + \sigma_2}{2}, \; \frac{\sigma_1 - \sigma_2}{\sigma_1 + \sigma_2}, \; R \tag{4.18}$$

Table 4.2 shows the correlation between the parameters, calculated during the MINUIT [75] fit to the $B^+ \to \mu^+ \nu \bar{D}^0 X$ sample. The largest correlations of parameters are found between the widths and R which describe the signal double Gaussian, between the position and shape of the bifurcated background peak, and between the magnitude of the exponential background and its decay constant.

Results

The results of the study can be seen in Tables 4.3, and 4.4. The parameters describing the background and signal peaks display no significant trends at the 3σ level. This was not the case for the decay constant, b_0, which describes the exponential background component. It shows significant trends: b_0 increases consistently across the VPDL bins, and with the increases to sample purity caused by flavour tagging. This implies that the parameter b_0 can not be fixed when fitting the sub-sample distributions.

Conclusions

The $K\pi$ mass distributions for the D^0- and D^*-samples can be modelled using Equation 4.13. The parameters which control the shape of the signal peak and peaking background (μ_0, σ_L, σ_R, μ_1, μ_2, σ_1, σ_2, R) can be fixed to values taken

	f_1^{bkg}	f_2^{bkg}	f^{sig}	b_0	μ_0	$\frac{\sigma_R+\sigma_L}{2}$	$\frac{\sigma_R-\sigma_L}{\sigma_R+\sigma_L}$	μ_1	$\frac{\sigma_1+\sigma_2}{2}$	R	$\frac{\sigma_1-\sigma_2}{\sigma_1+\sigma_2}$
f_1^{bkg}	1.00	-0.31	-0.08	-0.98	-0.26	-0.66	0.41	-0.09	-0.01	0.02	0.02
f_2^{bkg}		1.00	0.13	0.22	0.17	0.00	-0.29	0.05	0.24	0.15	-0.29
f^{sig}			1.00	0.04	0.08	0.15	-0.10	0.07	-0.12	-0.15	-0.08
b_0				1.00	0.21	0.60	-0.34	0.10	-0.06	-0.07	0.06
μ_0					1.00	0.13	-0.91	0.14	0.33	0.24	-0.38
$\frac{\sigma_R+\sigma_L}{2}$						1.00	-0.22	-0.05	-0.19	-0.23	0.17
$\frac{\sigma_R-\sigma_L}{\sigma_R+\sigma_L}$							1.00	-0.16	-0.52	-0.41	0.57
μ_1								1.00	-0.04	-0.06	0.01
$\frac{\sigma_1+\sigma_2}{2}$									1.00	0.96	-0.94
R										1.00	-0.84
$\frac{\sigma_1-\sigma_2}{\sigma_1+\sigma_2}$											1.00

Table 4.2: Table showing the correlations between the fitted variables to the $K\pi$ mass distribution of the $B^+ \rightarrow \mu^+\nu\bar{D}^0X$ sample. Large correlations are found between the widths and R which describe the signal double Gaussian; between the position and shape of the bifurcated background peak; and between the magnitude of the exponential background and its decay constant

		VPDL							Tag		
Parameter	All *(values)*	(-0.025, 0.000)	(0.000, 0.025)	(0.025, 0.050)	(0.050, 0.075)	(0.075, 0.100)	(0.100, 0.125)	(0.125, 0.250)	All	Mixed	Unmixed
b_0	0.464 ±0.001 GeV	-28	-21	-2.5	13	24	26	35	-14	-7.6	4.3
μ_0	1.620 ±0.001 GeV	-0.5	-1.2	-1.8	0.3	1.4	2.6	1.4	-1.3	1.9	-1.2
$\frac{\sigma_R+\sigma_L}{2}$	0.0669 ±0.0005 GeV	1.4	0.1	0.0	-1.7	-1.0	0.8	-1.7	0.1	0.9	0.4
$\frac{\sigma_R-\sigma_L}{\sigma_R+\sigma_L}$	-0.17 ±0.01	0.9	-0.3	-1.8	-0.3	1.3	1.8	0.8	-1.6	1.6	-1.0
μ_1	1.8570 ±0.0001 GeV	0.5	-2.9	-0.1	1.4	-0.5	1.7	3.0	1.0	1.2	3.4
$\frac{\sigma_1+\sigma_2}{2}$	0.042 ±0.001 GeV	0.2	0.0	-0.7	-0.3	-0.6	-0.5	-0.6	-0.6	-0.3	-0.5
R	0.47 ±0.04	1.2	-0.1	-0.7	0.1	-0.6	-0.4	0.1	-0.5	-0.2	-0.4
$\frac{\sigma_1-\sigma_2}{\sigma_1+\sigma_2}$	-0.34 ±0.01	1.2	-0.1	-0.7	0.1	-0.6	-0.4	0.1	-1.4	-0.9	-1.1

Table 4.3: Table showing the results of a free fit to $B^+ \rightarrow \mu^+\nu\bar{D}^0X$ samples. The first column contains parameter values from the fit to all events. Subsequent columns show the significance of the deviation from this value for the fits to sub-samples. The parameters describing the background and signal peaks display no significant trends at the 3σ level. The decay constant b_0 shows significant variation across the samples.

		VPDL							Tag		
Parameter	All *(values)*	(-0.025, 0.000)	(0.000, 0.025)	(0.025, 0.050)	(0.050, 0.075)	(0.075, 0.100)	(0.100, 0.125)	(0.125, 0.250)	All	Mixed	Unmixed
b_0	0.337 ±0.003 GeV	-5.9	-6.2	1.6	1.8	6.2	6.5	9.0	-3.9	-2.1	-0.0
μ_0	1.628 ±0.001 GeV	0.4	-1.0	-0.4	-0.1	0.9	0.2	0.9	0.4	0.4	1.2
$\frac{\sigma_R+\sigma_L}{2}$	0.069 ±0.001 GeV	-0.4	0.2	1.3	-1.1	-0.6	-0.2	-0.7	1.9	-3.2	-0.7
$\frac{\sigma_R-\sigma_L}{\sigma_R+\sigma_L}$	-0.12 ±0.02	-0.4	0.3	-0.2	-0.2	0.5	-0.1	-0.1	-0.9	-1.2	-1.1
μ_1	1.8565 ±.0002 GeV	-0.7	-3.9	0.7	0.4	2.0	2.5	1.5	-0.3	0.1	-0.3
$\frac{\sigma_1+\sigma_2}{2}$	0.042 ±0.001 GeV	-1.2	0.4	0.0	0.8	0.1	-0.7	-1.2	-0.6	-0.9	-0.2
R	0.39 ±0.04	2.3	0.0	0.2	0.7	0.3	-0.5	-1.0	-0.9	-1.1	-0.3
$\frac{\sigma_1-\sigma_2}{\sigma_1+\sigma_2}$	-0.36 ±0.01	-0.6	-0.4	-1.2	0.3	0.0	-0.7	0.2	1.1	0.7	2.2

Table 4.4: Table showing the results of a free fit to $B_d^0 \rightarrow \mu^+\nu D^{*-}X$ samples. The first column contains parameter values from the fit to all events. Subsequent columns show the significance of the deviation from this value for the fits to sub-samples. The parameters describing the background and signal peaks display no significant trends at the 3σ level. The decay constant b_0 shows significant variation across the samples.

from fits to the full statistic samples without biasing the resulting fit. The variable b_0 used to describe the exponential background component must be fitted to each sub-sample distribution separately, as it depends significantly on VPDL and on the result of flavour tagging.

4.3.2 Asymmetry fitting procedure

The D^0- and D^*-samples were divided into seven VPDL bins using the bin boundaries {-0.025, 0, 0.025, 0.05, 0.075, 0.1, 0.125, 0.25}. The events were flavour tagged with the combined tagger so that mass distributions for oscillated and non-oscillated events could be constructed. These mass distributions were then fitted using Equation 4.13 to determine N_i^{osc} and N_i^{nos}, the number of events tagged oscillated and tagged non-oscillated in the ith VPDL bin. These numbers were then used to find the asymmetry A_i in the ith VPDL bin:

$$A_i \quad = \quad \frac{N_i^{nos} - N_i^{osc}}{N_i^{nos} + N_i^{osc}} \tag{4.19}$$

The full set of asymmetries from both samples were then compared to the expected asymmetries A_i^e using a binned likelihood fit to determine the tagger dilution and Δm_d.

Calculation of N_i^{osc} and N_i^{nos}

The calculation of the expected number of oscillated and non-oscillated events in each VPDL bin for the D^*- and D^0-samples requires several inputs. The starting point is Equation 2.22:

$$\begin{aligned} \Gamma(B_d^0(t) \to \bar{f}) &= N_f \left|\langle f|B_d^0\rangle\right|^2 \frac{e^{-\Gamma_d t}}{2}\left[1 + \cos\Delta m_d t\right] \\ \Gamma(B_d^0(t) \to f) &= N_f \left|\langle f|B_d^0\rangle\right|^2 \frac{e^{-\Gamma_d t}}{2}\left[1 - \cos\Delta m_d t\right] \end{aligned} \tag{4.20}$$

This must be modified to include the effect of imperfect flavour tagging to produce the expected number of *tagged* oscillated and non-oscillated B_d^0 events (n_d^{osc}, n_d^{nos}):

$$\begin{aligned} n_d^{osc}(x,K) &= \frac{K}{c\tau_{B^0}}\exp(-\frac{Kx}{c\tau_{B^0}})\cdot 0.5\cdot[1-\mathcal{D}_d\cdot\cos(\Delta m_d Kx/c)] \\ n_d^{nos}(x,K) &= \frac{K}{c\tau_{B^0}}\exp(-\frac{Kx}{c\tau_{B^0}})\cdot 0.5\cdot[1+\mathcal{D}_d\cdot\cos(\Delta m_d Kx/c)] \end{aligned} \qquad (4.21)$$

here the relation $ct = Kx$ (Equation 2.26) has been used to convert the proper time (t) to VPDL (x) and the K-factor (K) described in Section 2.5. In addition the relation $\tau_{B^0} = \frac{1}{\Gamma_d}$ has been used to recast the decay constant Γ_d in terms of the B_d^0-lifetime τ_{B^0}, and the distributions have been normalised so that $\int\int(n_d^{osc}(x,K)+n_d^{nos}(x,K))dx\ dK\ = 1$.

The D^0- and D^*-samples also contain significant B^+ and B_s^0 components. The charged B^+-mesons do not oscillate, but due to the imperfect tag dilution some events are tagged as oscillated. Therefore the number of tagged oscillated and non-oscillated B^+-events (n_u^{osc}, n_u^{nos}) is given by:

$$\begin{aligned} n_u^{osc}(x,K) &= \frac{K}{c\tau_{B^+}}\exp(-\frac{Kx}{c\tau_{B^+}})\cdot 0.5\cdot(1-\mathcal{D}_u) \\ n_u^{nos}(x,K) &= \frac{K}{c\tau_{B^+}}\exp(-\frac{Kx}{c\tau_{B^+}})\cdot 0.5\cdot(1+\mathcal{D}_u) \end{aligned} \qquad (4.22)$$

The functional form of Equation 4.21 also describes the number of oscillated and non-oscillated B_s^0-decays (n_s^{osc}, n_s^{nos}). However the world averaged limit, $\Delta m_s >$ 16.6 ps^{-1} (95% CL) [18] means that the mixing period is much shorter than the VPDL intervals, and the approximation of 50% oscillated and 50% non-oscillated B^s-decays is valid:

$$\begin{aligned} n_s^{osc}(x,K) &= \frac{K}{c\tau_{B_s^0}}\exp(-\frac{Kx}{c\tau_{B_s^0}})\cdot 0.5 \\ n_s^{nos}(x,K) &= \frac{K}{c\tau_{B_s^0}}\exp(-\frac{Kx}{c\tau_{B_s^0}})\cdot 0.5 \end{aligned} \qquad (4.23)$$

The above equations can be integrated over the normalised K-factor distribution $D(K)$ to produce the number of events as a function of VPDL. The K-factor distributions are decay mode specific and determined from Monte Carlo studies [68].

For the jth decay mode of B_q-mesons the number of oscillated and non-oscillated events ($n_{q,\,j}^{osc,nos}$) as a function of VPDL will therefore be:

$$n_{q,\,j}^{osc,\;nos}(x) = \int n_{q,\,j}^{osc,non-osc}(x,K)\;D_j(K)\;dK \tag{4.24}$$

where $n_{q,\,j}^{osc,non-osc}(x,K)$ are taken from Equations 4.21–4.23.

This must then be modified to account for the imperfect accuracy of the experimentally measured VPDL (x^M). This is modelled with a resolution function $R_j(x - x^M, x^M)$. In addition the relative efficiency to reconstruct a given channel $\varepsilon_j(x^M)$ is also taken into account. These functions were both determined from Monte Carlo studies [68]. The resulting calculation for the number of oscillated and non-oscillated events reconstructed with VPDL x^M is then:

$$n_{q,\,j}^{osc,\;nos}(x^M) = \int R_j(x - x^M, x^M)\;\varepsilon_j(x)\;\theta(x)\;n_{q,\,j}^{osc,\;nos}(x)\;dx \tag{4.25}$$

where the step function $\theta(x)$ is used to imply positive x values in the integration. This equation describes the distribution of tagged oscillated and non-oscillated events for B_q-mesons decaying via mode j.

Sample composition

The following decay channels of B-mesons were considered for the D^*-sample:

- $B^0 \to \mu^+\nu D^{*-}$;
- $B^0 \to \mu^+\nu D^{**-} \to \mu^+\nu D^{*-}X$;
- $B^+ \to \mu^+\nu \bar{D}^{**0} \to \mu^+\nu D^{*-}X$.
- $B_s^0 \to \mu^+\nu D^{*-}X$.

The following decay channels of B-mesons were considered for the D^0 sample:

- $B^+ \to \mu^+\nu \bar{D}^0$;
- $B^+ \to \mu^+\nu \bar{D}^{*0}$;

- $B^+ \rightarrow \mu^+ \nu \bar{D}^{**0} \rightarrow \mu^+ \nu \bar{D}^0 X$;
- $B^+ \rightarrow \mu^+ \nu \bar{D}^{**0} \rightarrow \mu^+ \nu \bar{D}^{*0} X$;
- $B^0 \rightarrow \mu^+ \nu D^{**-} \rightarrow \mu^+ \nu \bar{D}^0 X$;
- $B^0 \rightarrow \mu^+ \nu D^{**-} \rightarrow \mu^+ \nu \bar{D}^{*0} X$.
- $B_s^0 \rightarrow \mu^+ \nu \bar{D}^0 X$;
- $B_s^0 \rightarrow \mu^+ \nu \bar{D}^{*0} X$.

Here and in the following the symbol "D^{**}" denotes both narrow and wide D^{**} resonances, together with non-resonant $D\pi$ and $D^*\pi$ production. The contribution of $D\pi\pi$ final states was neglected.

An additional consideration was the relative efficiency of reconstructing the above channels using the $B \rightarrow D^0 \mu \nu X$ selection cuts. This variation is dependent on the kinematics of each decay channel, and was estimated using Monte Carlo simulation.

The latest PDG values [16] were used to determine the branching fractions of decays contributing to the D^0- and D^*-samples:

- $\mathrm{Br}(B^+ \rightarrow \mu^+ \nu \bar{D}^0) = 2.15 \pm 0.22\%$;
- $\mathrm{Br}(B^0 \rightarrow \mu^+ \nu D^-) = 2.14 \pm 0.20\%$;
- $\mathrm{Br}(B^+ \rightarrow \mu^+ \nu \bar{D}^{*0}) = 6.5 \pm 0.5\%$;
- $\mathrm{Br}(B^0 \rightarrow \mu^+ \nu D^{*-}) = 5.44 \pm 0.23\%$;

The $\mathrm{Br}(B^+ \rightarrow \mu^+ \nu \bar{D}^{**0})$ was estimated using the following inputs:

- $\mathrm{Br}(B \rightarrow \mu^+ \nu X) = 10.73 \pm 0.28\%$;
- $\mathrm{Br}(B^0 \rightarrow \mu^+ \nu X) = \tau^0/\tau^+ \cdot \mathrm{Br}(B^+ \rightarrow \mu^+ \nu X)$;

- $\mathrm{Br}(B^+ \to \mu^+\nu\bar{D}^{**0}) = \mathrm{Br}(B^+ \to \mu^+\nu X) - \mathrm{Br}(B^+ \to \mu^+\nu\bar{D}^0) - \mathrm{Br}(B^+ \to \mu^+\nu D^{*-})$;
- $\mathrm{Br}(B^0 \to \mu^+\nu D^{**-}) = \mathrm{Br}(B^0 \to \mu^+\nu X) - \mathrm{Br}(B^0 \to \mu^+\nu D^-) - \mathrm{Br}(B^+ \to \mu^+\nu\bar{D}^{*0})$;
- $\mathrm{Br}(B^0 \to \mu^+\nu D^{**-}) = \tau^0/\tau^+ \cdot \mathrm{Br}(B^+ \to \mu^+\nu\bar{D}^{**0})$;

and the following value was obtained:

$$\mathrm{Br}(B^+ \to \mu^+\nu\bar{D}^{**0}) = 2.70 \pm 0.47\% \tag{4.26}$$

The $\mathrm{Br}(B^+ \to \mu^+\nu\bar{D}^{**0} \to \mu^+\nu D^{*-}X)$ was estimated from the following inputs:

- $\mathrm{Br}(\bar{b} \to l^+\nu D^{*-}\pi^+X) = (4.73 \pm 0.77 \pm 0.55) \cdot 10^{-3}$ [71];
- $\mathrm{Br}(\bar{b} \to l^+\nu D^{*-}\pi^+X) = (4.80 \pm 0.9 \pm 0.5) \cdot 10^{-3}$ [64];
- $\mathrm{Br}(\bar{b} \to l^+\nu D^{*-}\pi^-X) = (0.6 \pm 0.7 \pm 0.2) \cdot 10^{-3}$ [64];

and assuming $\mathrm{Br}(b \to B^+) = 0.397 \pm 0.010$[16]. A common practice in estimating this decay rate is to neglect the contributions of decays $D^{**} \to D^*\pi\pi$. However by using the above measurements this contribution can be calculated. Neglecting decays $D^{**} \to D^*\pi\pi\pi$, which contribute $\sim 1\%$ to D^{**} decays according to simulation, and using the following relations:

$$\begin{aligned}
\mathrm{Br}(\bar{B} \to l^+\nu D^{*-}\pi^+X) &= \mathrm{Br}(B^+ \to l^+\nu D^{*-}\pi^+X^0) + \mathrm{Br}(B^0 \to l^+\nu D^{*-}\pi^+\pi^-) \\
\mathrm{Br}(\bar{B} \to l^+\nu D^{*-}\pi^-X) &= \mathrm{Br}(B^0 \to l^+\nu D^{*-}\pi^+\pi^-)
\end{aligned}$$

the following value is obtained:

$$\mathrm{Br}(B^+ \to \mu^+\nu\bar{D}^{**0} \to l^+\nu D^{*-}X) = 1.06 \pm 0.24\% \tag{4.27}$$

All other rates $\mathrm{Br}(B \to \mu^+\nu\bar{D}^{**} \to \mu^+\nu\bar{D}^*X)$ were obtained using the following relations:

- $\mathrm{Br}(B^0 \to \mu^+\nu D^{**-}(D^*\pi)) = \tau^0/\tau^+ \cdot \mathrm{Br}(B^+ \to \mu^+\nu \bar{D}^{**0}(D^*\pi)X)$;
- $\mathrm{Br}(B \to \mu^+\nu \bar{D}^{**}(\bar{D}^*\pi^+)X) = 2 \cdot \mathrm{Br}(B \to \mu^+\nu \bar{D}^{**}(\bar{D}^*\pi^0)X)$ (isospin invariance);

The following inputs were used for the $\mathrm{Br}(B \to \mu^+\nu \bar{D}^{**} \to \mu^+\nu \bar{D}X)$ estimate:

- $\mathrm{Br}(B \to \mu^+\nu \bar{D}^{**}(\bar{D}\pi^+)X) = 2 \cdot \mathrm{Br}(B \to \mu^+\nu \bar{D}^{**}(\bar{D}\pi^0)X)$ (isospin invariance);
- $\mathrm{Br}(B \to \mu^+\nu \bar{D}^{**}(\bar{D}\pi)X) = \mathrm{Br}(B \to \mu^+\nu \bar{D}^{**}) - \mathrm{Br}(B \to \mu^+\nu \bar{D}^{**}(\bar{D}^*\pi)X)$.

To estimate branching rates of B_s^0 decays, the following inputs were used:

- $\mathrm{Br}(B_s^0 \to \mu^+\nu X) = \tau^s/\tau^d \cdot \mathrm{Br}(B^0 \to \mu^+\nu X)$;
- $\mathrm{Br}(B_s^0 \to \mu^+\nu D_s^- X) = 7.9 \pm 2.4\%$[16];
- $\mathrm{Br}(B_s^0 \to \mu^+\nu D_s^{**-} \to \mu^+\nu D^{*-}X) = \mathrm{Br}(B_s^0 \to \mu^+\nu D_s^{**-} \to \mu^+\nu \bar{D}^{*0}X)$ (isospin invariance).

There is no experimental measurement for the fraction, R_s^{**} of $B_s^0 \to \mu^+\nu D_s^{**-}$ decays in which D_s^{**-} then decays to D^*X. For the purposes of this analysis the value of R_s^{**} was set at 0.35 and varied from 0 to 1 in the systematic studies.

A cross check of the predicted sample composition was made using Monte Carlo data using the standard DØ code for event generation. This study neglected any contribution to the samples from B_s decays. The calculation using the above branching fractions (without accounting for reconstruction efficiencies) predicts that the D^*-sample consists of 89% B_d^0 decays and 10% $B+$ decays, and the D^0-sample consists of 85% B^+ decays and 15% B_d^0 decays. The Monte Carlo simulation was in good agreement, predicting that the D^*-sample was composed of 87% B_d^0 decays and 13% B^+ decays, and that the D^0-sample consisted of 83% B^+ events and 17% B_d^0 events.

Including the effects of reconstruction efficiencies and the contribution by B_s channels in the calculation produces the following sample composition: the D^*-sample contains 89% B_d^0, 10% B^+ and 1% B_s^0 and the D^0-sample contains 83% B^+, 16% B_d^0 and 1% B_s^0.

Contribution of $B \to \mu^+\nu\bar{D}^0X$-decays to the D^*-sample

The signal events in both the D^0- and D^*-samples are fitted to the $K\pi$ mass distribution. This means that $B \to \mu^+\nu\bar{D}^0X$ decays which combine with a random pion candidate to produce a mass difference within the D^*-signal selection ($0.1425 < \Delta M(D^0 - D^*) < 0.1490$ GeV) will contribute to the $B \to \mu^+\nu\bar{D}^*X$ signal.

The magnitude of this effect was determined using data. For real D^*-signal events the charge correlation between the reconstructed muon and the additional pion will always be opposite. However the charge correlation between a D^0-signal event and additional pion will be random. Therefore the contribution to the D^*-sample from "$B \to \mu^+\nu\bar{D}^0X$ plus random pion" decays will be twice as large if the D^*-sample is reselected without a requirement on the additional pion charge. This comparison of the number of signal events in the D^*-sample with and without the charge requirement was made, and it was estimated that "$B \to \mu^+\nu\bar{D}^0X$ plus random pion" decays contribute $(4.00 \pm 0.85)\%$ to the D^*-sample.

Contribution of $c\bar{c}$-decays

In addition to B-decays, an important background process is the charmed decay $c\bar{c} \to \mu^+\nu\bar{D}^0X$, in which a pseudo B-vertex is formed from the reconstructed $\bar{c} \to \mu^+\nu X$ and $c \to \bar{D}^0X$ decays. A dedicated analysis of this background was made using both data and simulated events. This showed that the pseudo-decay length arising from the crossing of the muon and D^0 tracks resulted in a distribution centred around zero with width 150 μm. The form of the distribution as a function of

VPDL: $N_{c\bar{c}}(x^M)$, was taken from the simulated events. For the calculation of the contribution of these events, it was assumed that the ratio of the branching rates $c \rightarrow \bar{D}^0 X$ and $c \rightarrow D^* X$ was the same as for semileptonic B decays, and that the $c\bar{c}$ decays are tagged oscillated or non-oscillated with equal probability.

Calculation of A_i^e

The sample contribution studies can now be included in Equation 4.25 to find the total number of oscillated and non-oscillated events ($N_i^{e,\ osc}$, $N_i^{e,\ nos}$) summed over all contributing decay channels in each VPDL bin:

$$N_i^{e,nos/osc} = \int_i dx^M \left((1 - f_{c\bar{c}})(\sum_{q=u,d,s} \sum_j (Br_j \cdot n_{q,\ j}^{nos/osc}(x^M))) + f_{c\bar{c}} N_{c\bar{c}}(x^M) \right) \tag{4.28}$$

Here the integration $\int_i dx^M$ is taken over a given VPDL interval i, the sum $\sum_j$ is taken over all decay channels $B \rightarrow \mu^+ \nu \bar{D}^0 X$ contributing to the selected sample, , Br_j is the branching rate of a given channel j, and $f_{c\bar{c}}$ is the fraction of $c\bar{c}$ decays in the data sample.

Finally, the expected value, A_i^e, for interval i of the measured VPDL is given by:

$$A_i^e(\Delta m, f_{c\bar{c}}, \mathcal{D}_d, \mathcal{D}_u) = \frac{N_i^{e,nos} - N_i^{e,osc}}{N_i^{e,nos} + N_i^{e,osc}} \tag{4.29}$$

Minimisation code

The expected asymmetry A^e is compared with the measured asymmetry A_i, across all VPDL bins and for both samples. The variables Δm_d, $f_{c\bar{c}}$, $\mathcal{D}_u$ and $\mathcal{D}_d$ are adjusted to minimise χ^2 given by:

$$\begin{aligned}
\chi^2(\Delta m_d, f_{c\bar{c}}, \mathcal{D}_d, \mathcal{D}_u) &= \chi^2_{D^*}(\Delta m_d, f_{c\bar{c}}, \mathcal{D}_d, \mathcal{D}_u) + \chi^2_{D^0}(\Delta m_d, f_{c\bar{c}}, \mathcal{D}_d, \mathcal{D}_u) \\
\chi^2_{D^*}(\Delta m_d, f_{c\bar{c}}, \mathcal{D}_d, \mathcal{D}_u) &= \sum_i \frac{(A_{i,D^*} - A^e_{i,D^*}(\Delta m_d, f_{c\bar{c}}, \mathcal{D}_d, \mathcal{D}_u))^2}{\sigma^2(A_{i,D^*})} \\
\chi^2_{D^0}(\Delta m_d, f_{c\bar{c}}, \mathcal{D}_d, \mathcal{D}_u) &= \sum_i \frac{(A_{i,D^0} - A^e_{i,D^0}(\Delta m_d, f_{c\bar{c}}, \mathcal{D}_d, \mathcal{D}_u))^2}{\sigma^2(A_{i,D^0})}.
\end{aligned} \tag{4.30}$$

Here $\sum_i$ is the sum over all VPDL bins.

4.4 Results

The analysis was performed using the following flavour tag selections:

- Events tagged by the combined tagger with a quality cut $|d| > 0.3$. This formed a large sample so that the performance could be examined with minimal interference by statistical fluctuations.
- Events tagged by the individual muon, electron and SV tags with quality cut $|d| > 0.3$ were studied. This was in order to uncover any peculiarities in the individual taggers.
- Events tagged by the combined tag in four bins of $|d|$. This was in order to study the relationship between d and $\mathcal{D}$. The bin boundaries {0.1, 0.2, 0.35, 0.45, 0.6, 1.0} were chosen to split the events between the bins evenly and so that each bin contained sufficient statistics for fitting.

For each selection the values of N_i^{osc} and N_i^{nos} were determined and used to calculate the associated asymmetries A_i. The mass fits to the full D^*-samples tagged by the muon, electron and SV tags are shown in Figure 4.9. Examples of the mass fits in the low statistic sub-samples are shown in Figures 4.10–4.13. Figures 4.10 and 4.11 show the fitted oscillated and non-oscillated distributions for the SV tagged D^*-sample tagged with a requirement $|d| > 0.3$. Figures 4.12 and 4.13 show the fitted oscillated and non-oscillated distributions for the muon tagged D^*-sample tagged with a requirement $|d| > 0.3$. Both these sets of fits use parameters constrained by a fit to the full D^*-sample, but the function still fits the distributions reasonably.

Examples of the fitted asymmetries with a requirement $|d| > 0.3$ are shown for

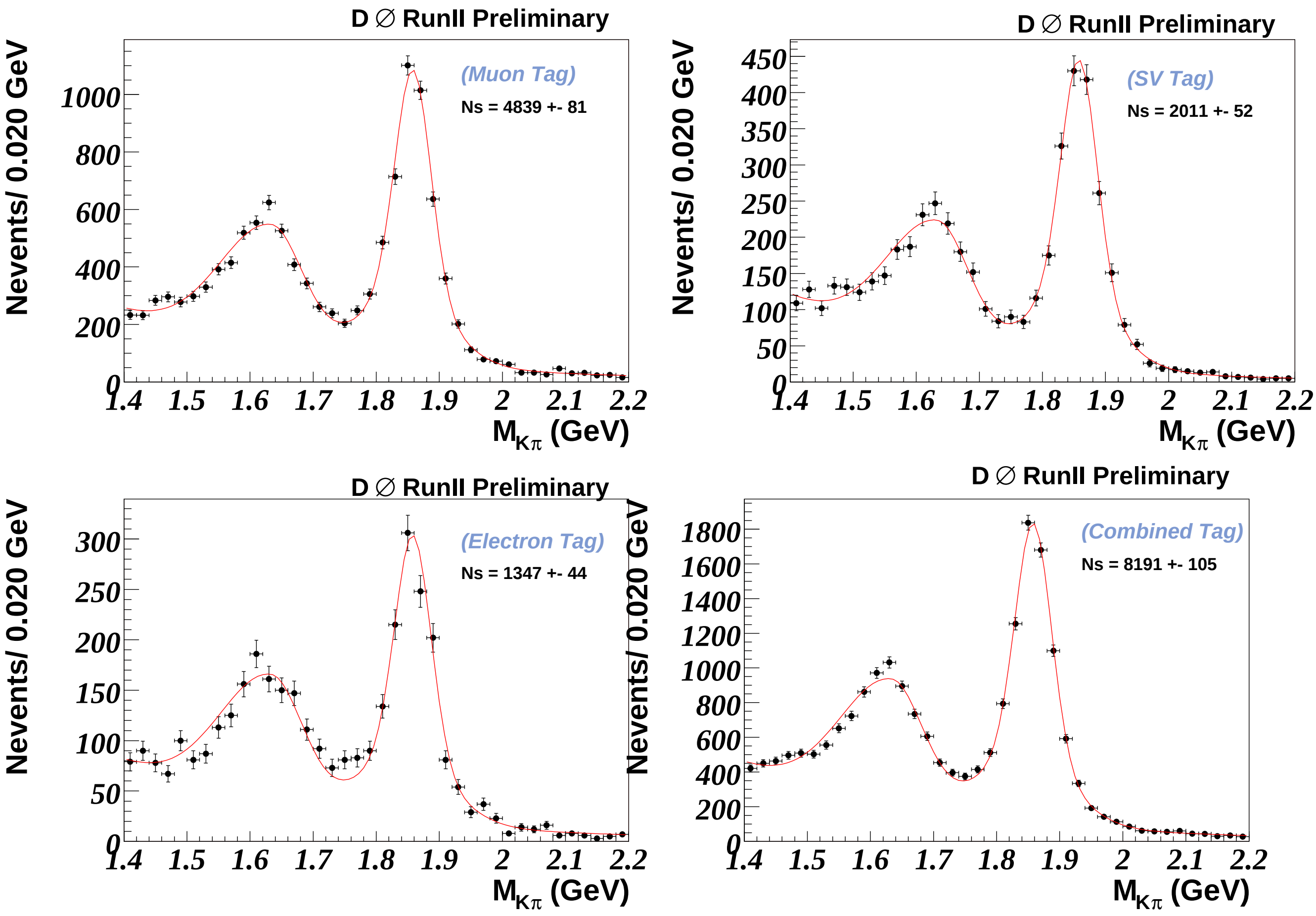

Figure 4.9: Tagged $M(K\pi)$ distribution for events in the D^* sample, tagged by the three taggers: muon, SV charge and electron, and by the combined tagger for $|d| > 0.3$. The fitted function and parameters corresponds to eqn. (4.13).

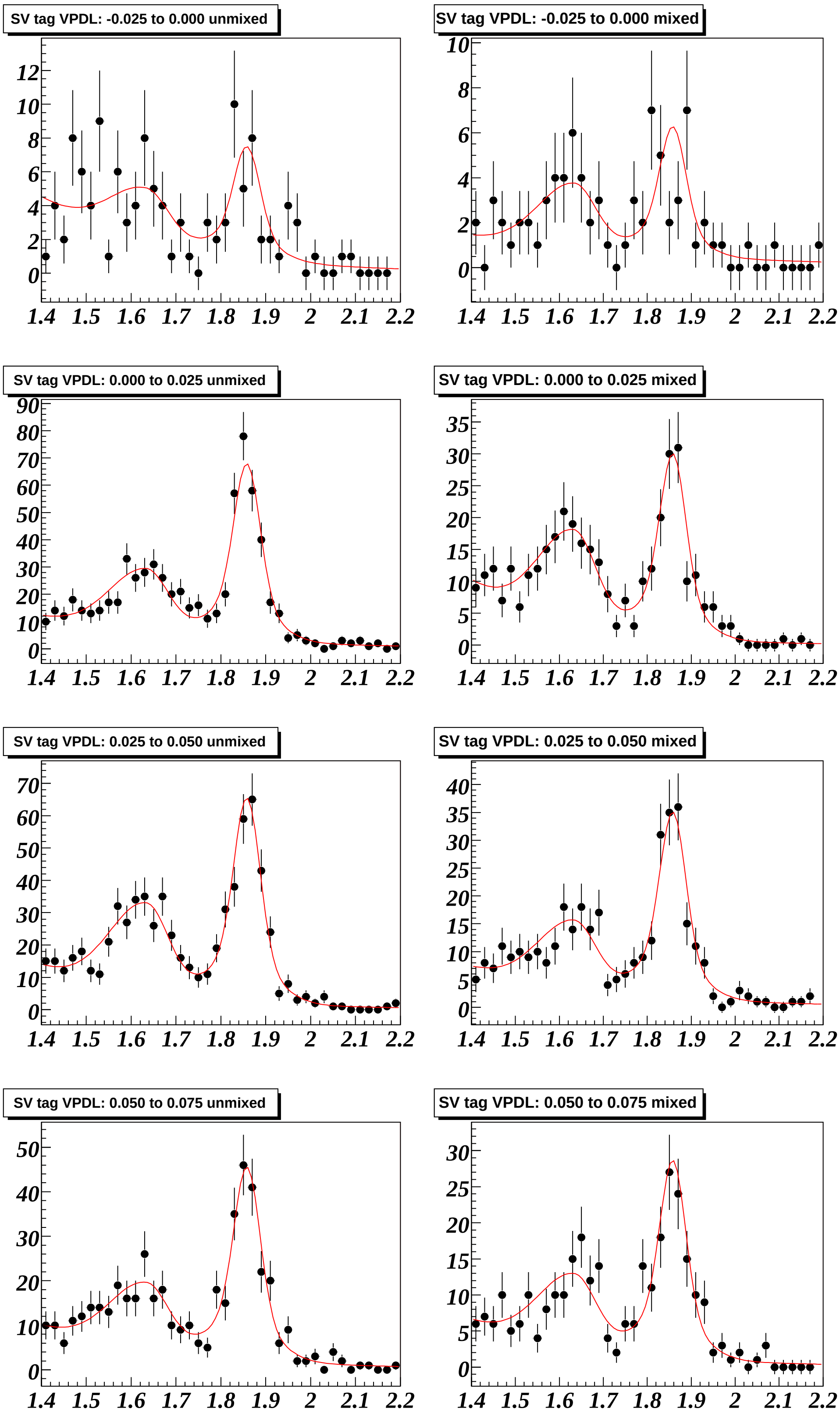
SV tag VPDL: -0.025 to 0.000 unmixed

SV tag VPDL: -0.025 to 0.000 mixed

SV tag VPDL: 0.000 to 0.025 unmixed

SV tag VPDL: 0.000 to 0.025 mixed

SV tag VPDL: 0.025 to 0.050 unmixed

SV tag VPDL: 0.025 to 0.050 mixed

SV tag VPDL: 0.050 to 0.075 unmixed

SV tag VPDL: 0.050 to 0.075 mixed

Figure 4.10: The fit to $M(K\pi)$ mass for non-oscillating (left) and oscillating (right) for μ^+D^{*-} events tagged by the SV charge with $|d| > 0.3$ in bins -0.025-0.0, 0.0-0.025, 0.025-0.050, 0.050-0.075

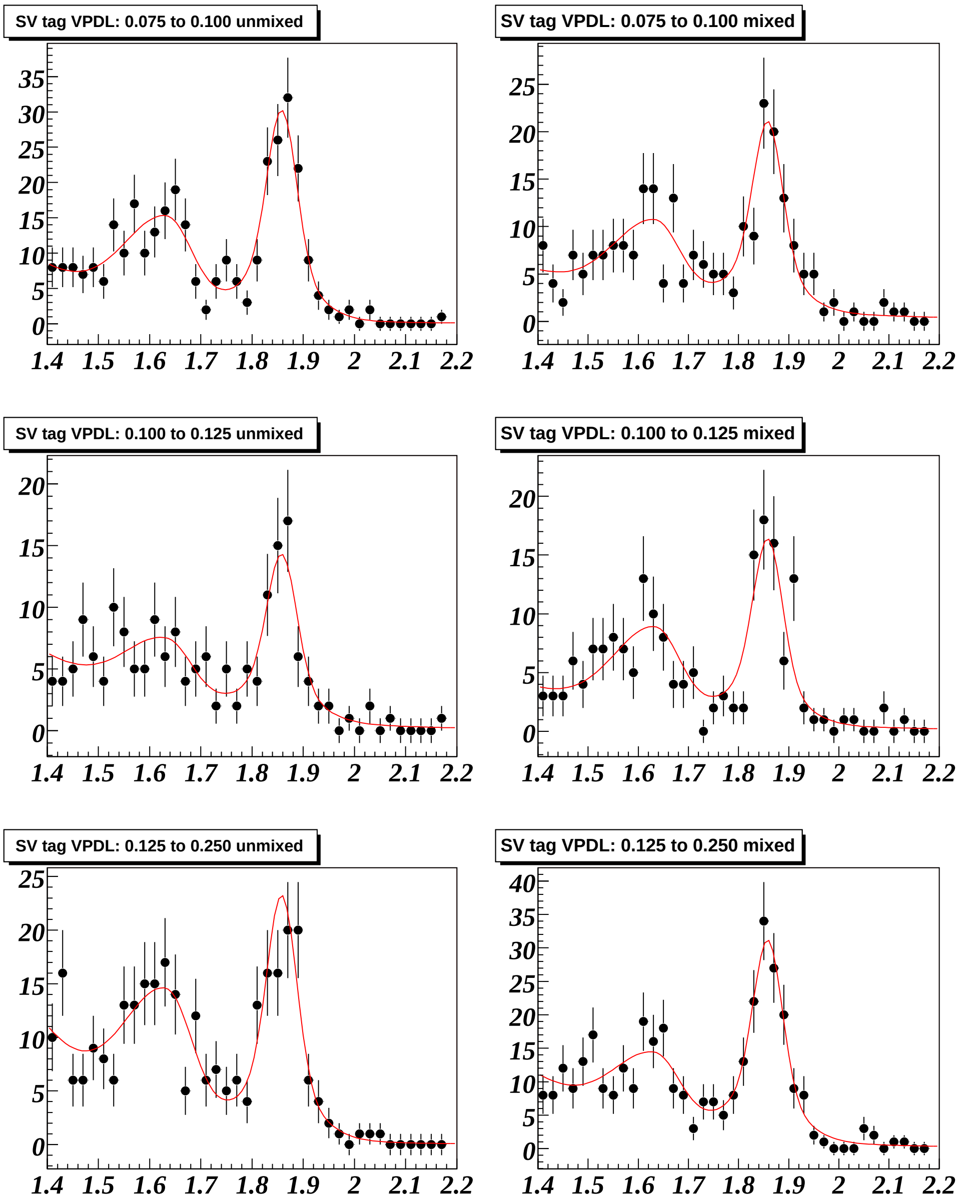

Figure 4.11: The fit to $M(K\pi)$ mass for non-oscillating (left) and oscillating (right) for μ^+D^{*-} events tagged by the SV charge with $|d| > 0.3$ in bins 0.075-0.100, 0.100-0.125, 0.125-0.250

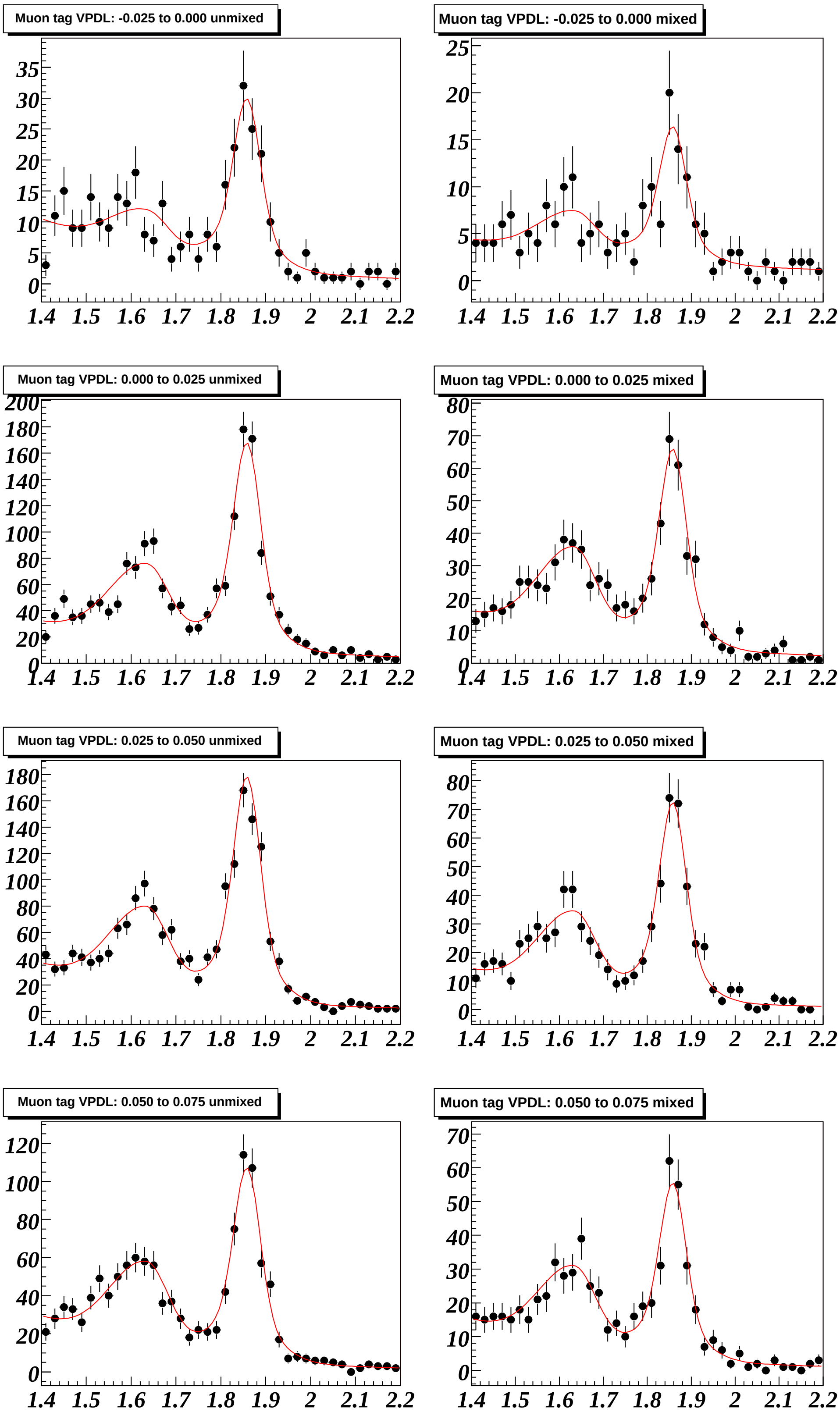

Figure 4.12: The fit to $M(K\pi)$ mass for non-oscillating (left) and oscillating (right) for $\mu^+ D^{*-}$ events tagged by the Muon tagger with $|d| > 0.3$ in bins -0.025-0.0, 0.0-0.025, 0.025-0.050, 0.050-0.075

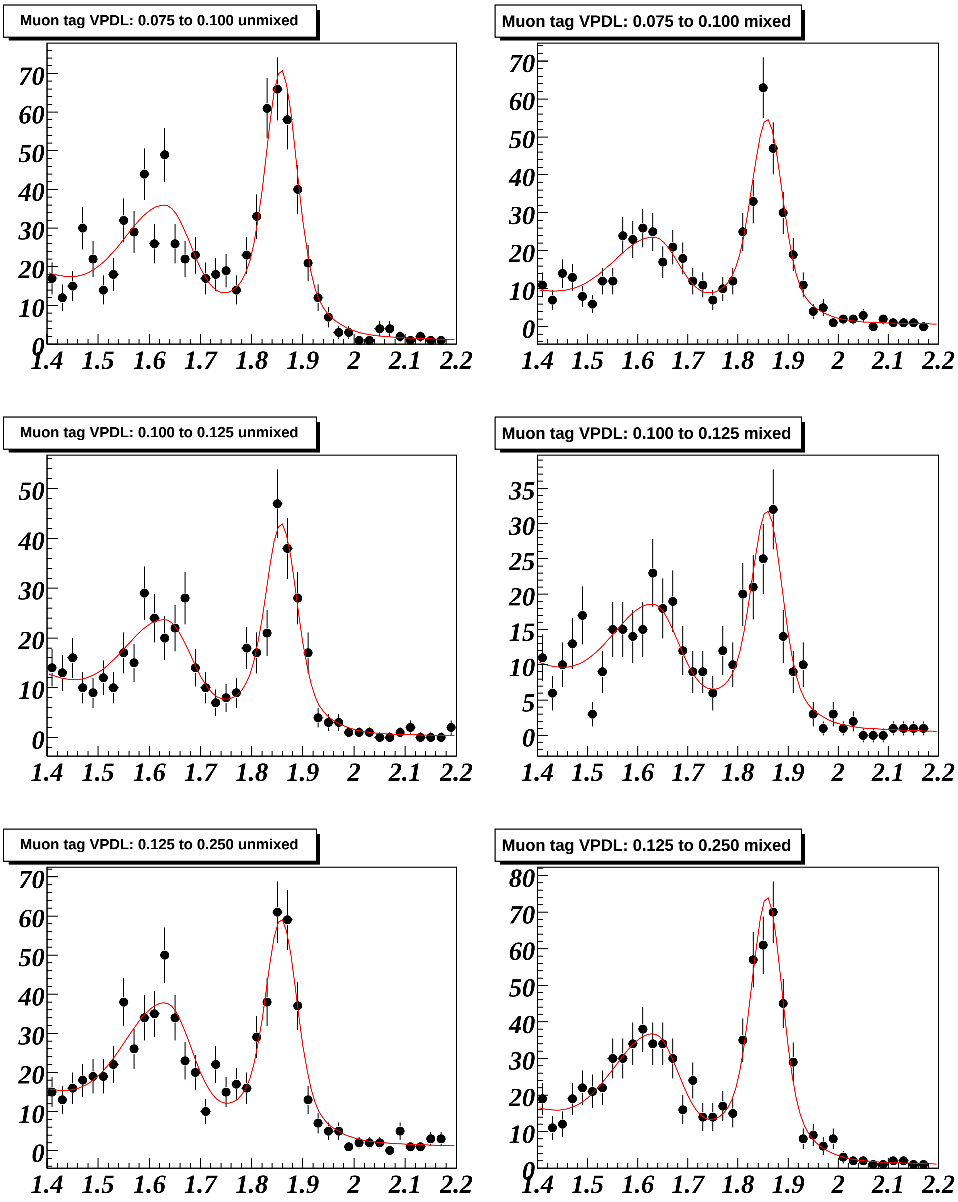

Figure 4.13: The fit to $M(K\pi)$ mass for non-oscillating (left) and oscillating (right) for $\mu^+ D^{*-}$ events tagged by the Muon tagger with $|d| > 0.3$ in bins 0.075-0.100, 0.100-0.125, 0.125-0.250

the muon, electron, SV, and combined tags in Figures 4.14 and 4.15. Figures 4.16 to 4.18 show the fitted asymmetries for the combined tagger in bins of $|d|$. The vertical error bars on these plots are calculated from the uncertainty in the fitted values of N^{osc} and N^{nos}. The horizonal bars drawn correspond to the VPDL bin intervals. The curves shown are illustrative, and drawn through the fitted asymmetry values calculated at each of the measured points.

There is a drop in the asymmetry in the first negative VPDL bin for all tag selections. This is due to the contribution of the $c\bar{c}$ background events. The $c\bar{c}$ fake vertices are distributed symmetrically around the primary vertex, and so have the largest effect in the short VPDL bins. Their effect is largest in the negative bin since real B-events all have positive decay length, and are only reconstructed with negative VPDL through the imperfect vertex resolution.

In all plots with $|d| > 0.3$ the B_d^0-flavour oscillations are clearly visible in the measured asymmetries for the D^*-sample. As expected the D^0-sample which contains only a small B_d^0-component shows smaller variation. The plot for the combined tag with the cut $|d| > 0.3$ (shown in Figure 4.15) has the largest statistics and therefore the smallest statistical error on the measured asymmetries. This plot shows the good agreement between measured and fitted asymmetries across the VPDL bins.

The measured asymmetry in the first positive VPDL bin for each tagger is approximately the same in the D^*- and D^0-samples. This is expected since these decays are largely unoscillated, and the opposite side tagger is predicted to have the same dilution for tagging B^+ and B_d^0 decays. The collated results are shown in

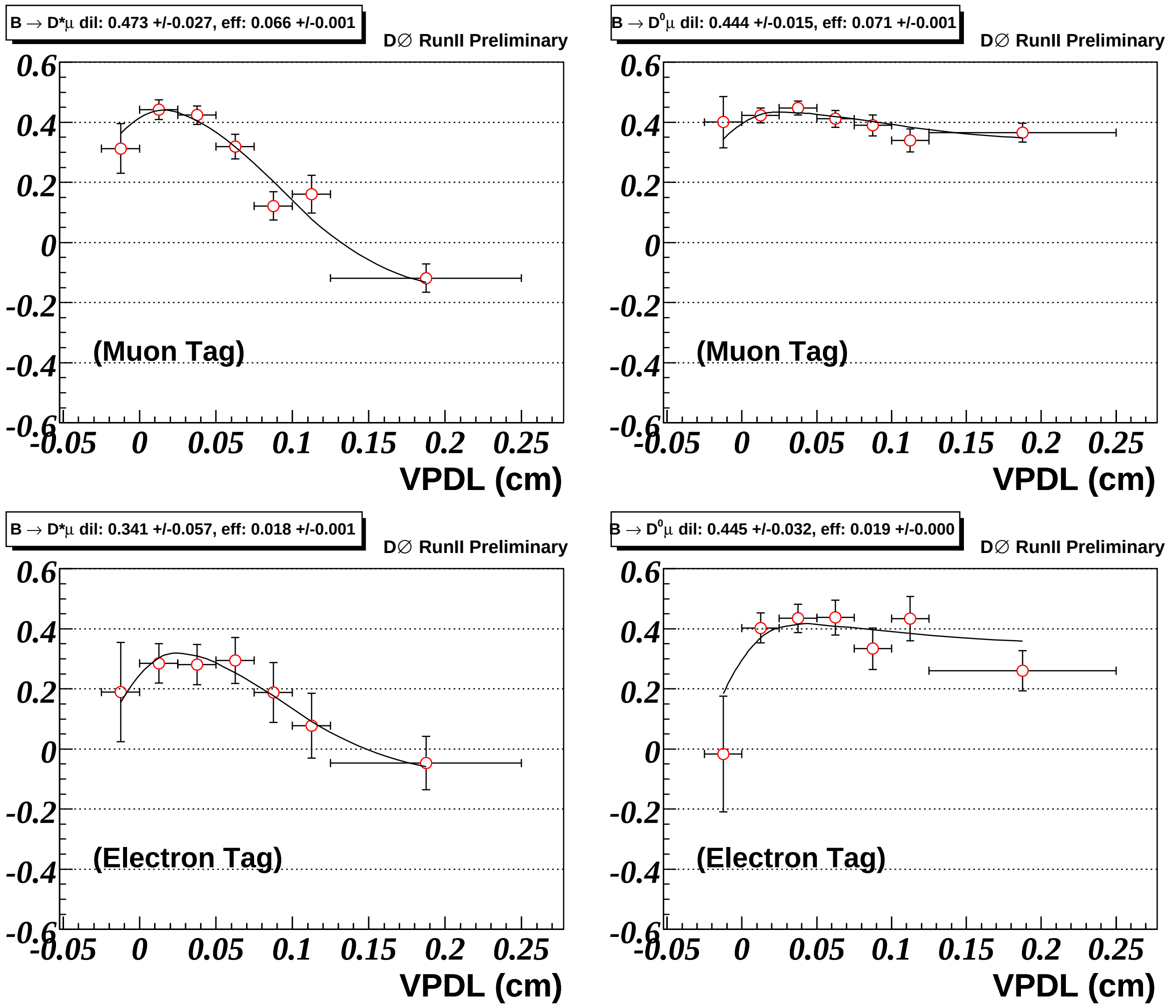

Figure 4.14: The asymmetries obtained in the D^* (left) and D^0 (right) samples with the result of the fit superimposed for the Muon and electron tagger. For the individual taggers, $|d| > 0.3$ was required. The drop in the negative VPDL bin is due to the $c\bar{c}$ background. Flavour oscillation of the B_d meson component is responsible for the fall in asymmetries across the positive VPDL bins.

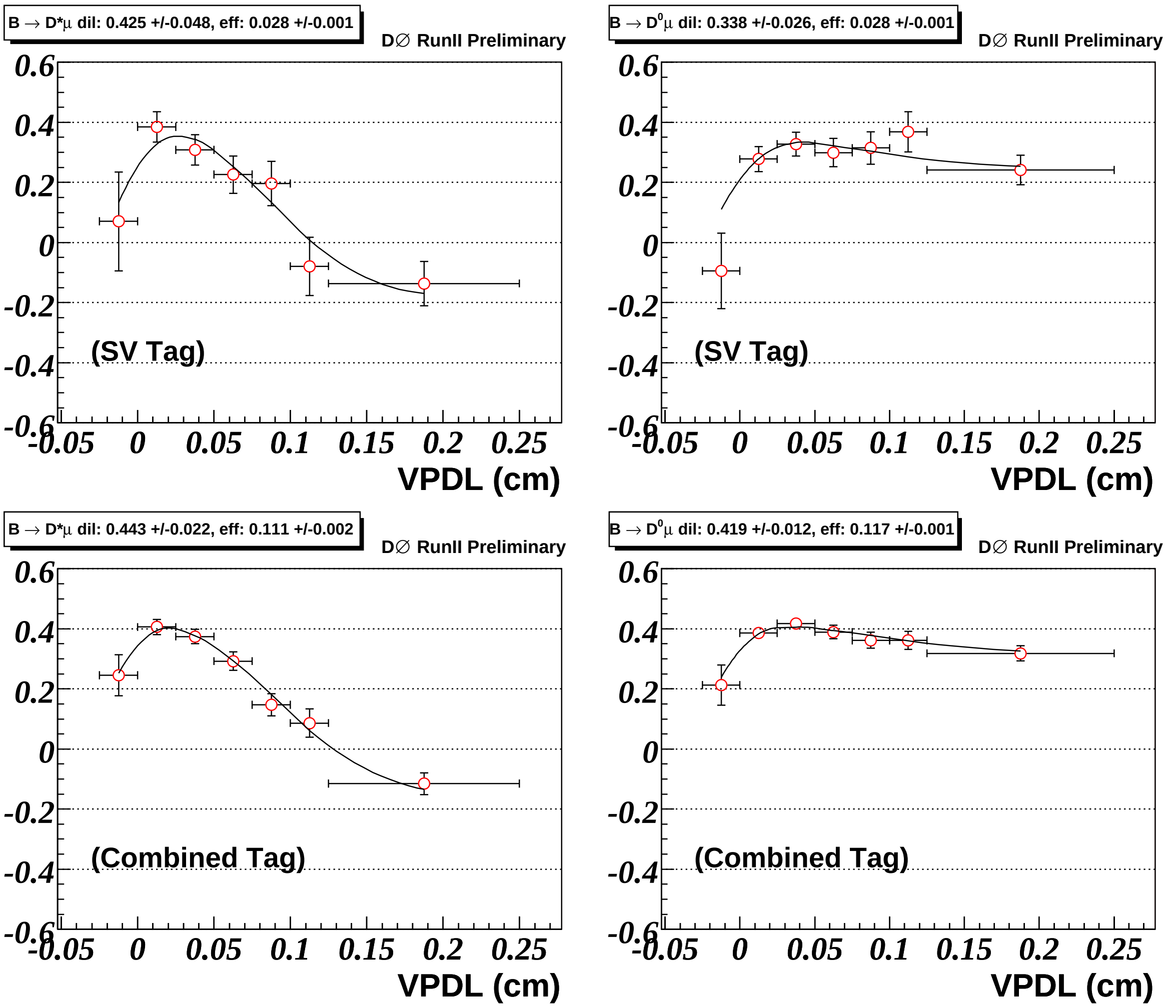

Figure 4.15: The asymmetries obtained in the D^* (left) and D^0 (right) samples with the SV and the combined tagger and the result of the fit superimposed. The samples required $|d| > 0.3$. The drop in the negative VPDL bin is due to the $c\bar{c}$ background. Flavour oscillation of the B_d meson component is responsible for the fall in asymmetries across the positive VPDL bins.

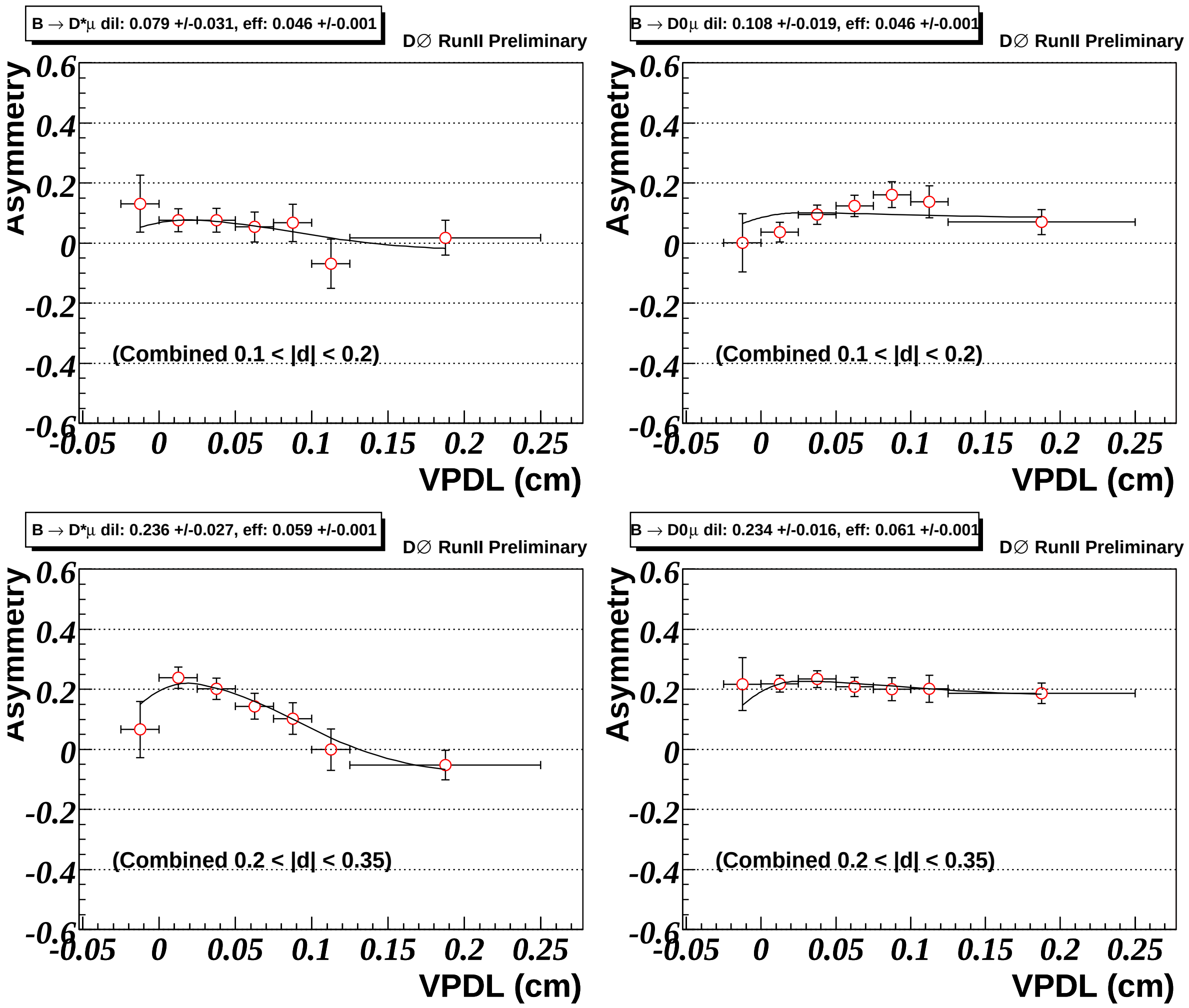

Figure 4.16: The asymmetries obtained in the D^* (left) and D^0 (right) samples with the combined tagger in $|d|$ bins, 0.1-0.2 and 0.2-0.3. The result of the fit is superimposed. As expected the measured asymmetries correspond to the $|d|$ interval with larger asymmetries found for events with larger values of $|d|$.

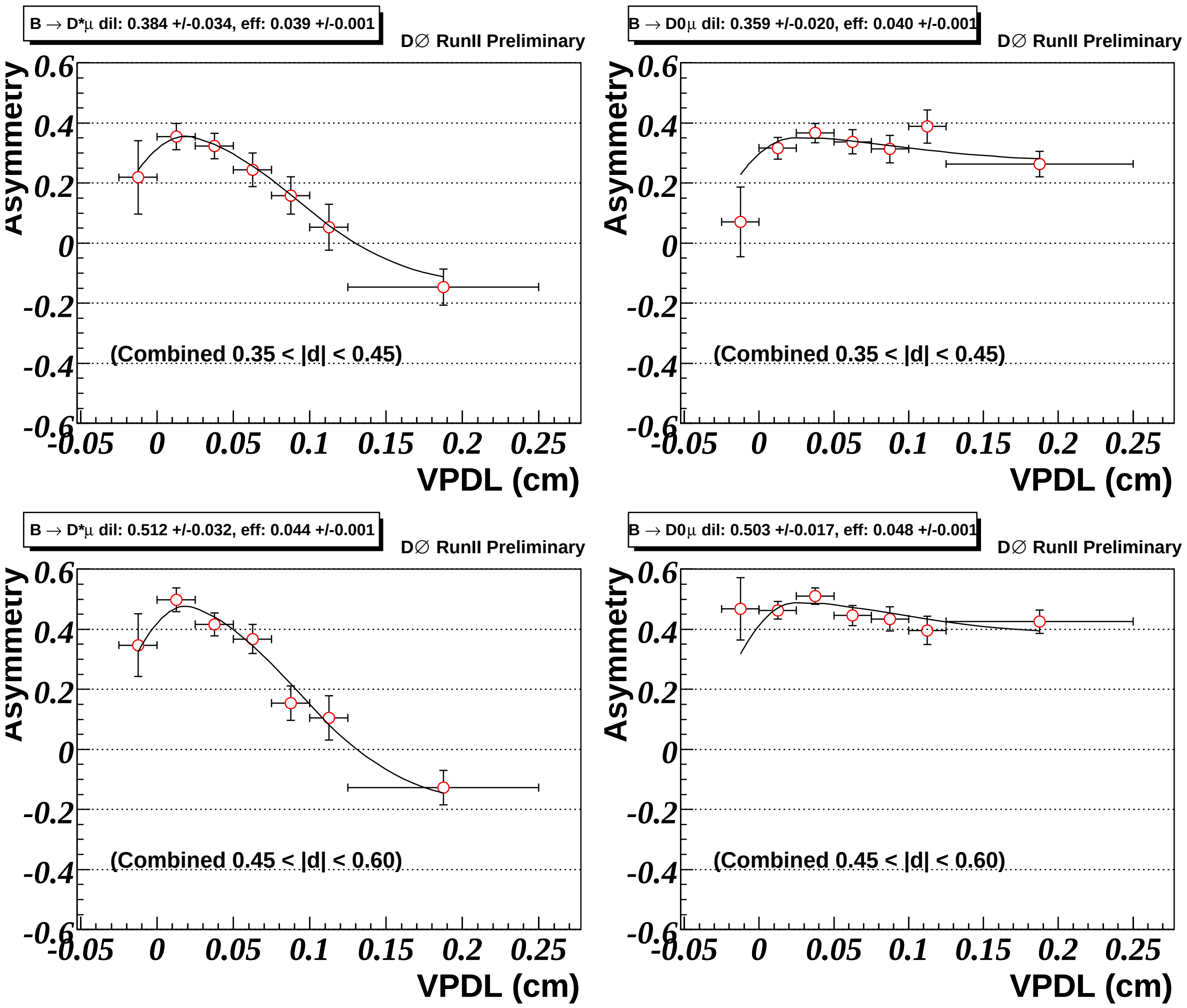

Figure 4.17: The asymmetries obtained in the D^* (left) and D^0 (right) samples with the combined tagger in $|d|$ bins, 0.3-0.45 and 0.45-0.6. The result of the fit is superimposed. As expected the measured asymmetries correspond to the $|d|$ interval with larger asymmetries found for events with larger values of $|d|$.

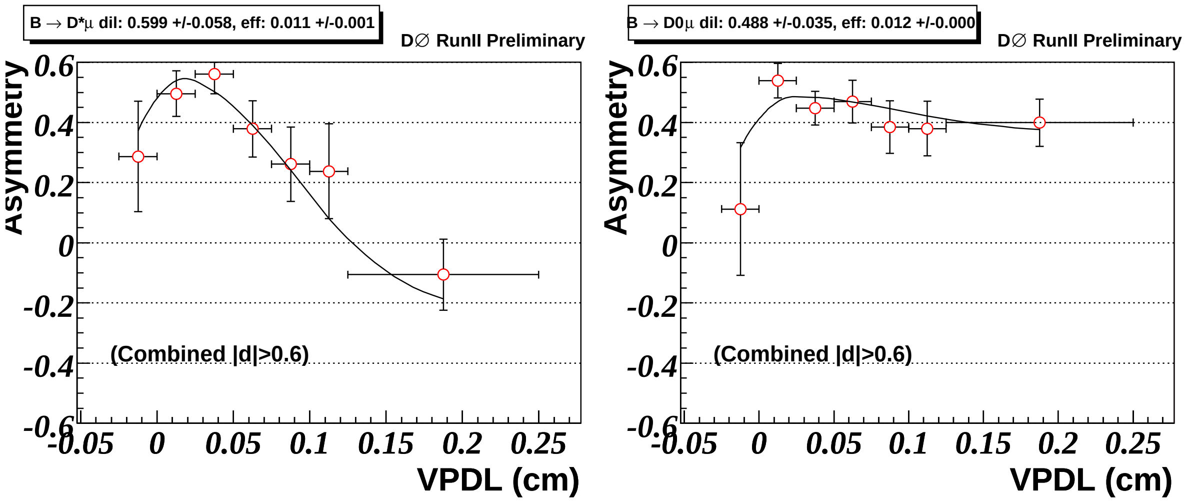

Figure 4.18: The asymmetries obtained in the D^* (left) and D^0 (right) sample with the combined tagger for bin $|d| > 0.6$. The result of the fit is superimposed. As expected the measured asymmetries correspond to the $|d|$ interval with larger asymmetries found for events with larger values of $|d|$.

Tables 4.5–4.7. Tables 4.6 and 4.5 shows the measured efficiencies, dilutions and resulting tagging power for each of the flavour tag selections. Table 4.7 shows the fitted values of Δm_d and the $c\bar{c}$-fraction for each selected tagger.

The values of Δm_d and $f_{c\bar{c}}$ are compatible across the component taggers. The measured values of $\mathcal{D}$ are all > 0.3 for the $|d| > 0.3$ samples, as expected[3]. The best

Tagger	$\varepsilon(\%)$	$\mathcal{D}_d$	$\varepsilon\mathcal{D}_d^2(\%)$
Muon ($\lvert d\rvert > 0.3$)	6.61 ± 0.12	0.473 ± 0.027	1.48 ± 0.17
Electron ($\lvert d\rvert > 0.3$)	1.83 ± 0.07	0.341 ± 0.058	0.21 ± 0.07
SVCharge ($\lvert d\rvert > 0.3$)	2.77 ± 0.08	0.424 ± 0.048	0.50 ± 0.11
Combined ($\lvert d\rvert > 0.3$)	11.14 ± 0.15	0.443 ± 0.022	2.19 ± 0.22
Combined($0.10< \lvert d\rvert <0.20$)	4.63 ± 0.10	0.084 ± 0.031	0.03 ± 0.02
Combined($0.20< \lvert d\rvert <0.30$)	5.94 ± 0.12	0.236 ± 0.027	0.33 ± 0.08
Combined($0.30< \lvert d\rvert <0.45$)	3.89 ± 0.09	0.385 ± 0.034	0.58 ± 0.10
Combined($0.45< \lvert d\rvert <0.60$)	4.36 ± 0.10	0.512 ± 0.032	1.14 ± 0.14
Combined($0.60< \lvert d\rvert <1.00$)	1.13 ± 0.05	0.597 ± 0.058	0.40 ± 0.08

Table 4.5: Tagging performance for events with reconstructed B^0 for different taggers and subsamples.

---

[3] The value of D is expected to differ for each individual tagger with a requirement —d—¿0.3 since they follow different $|d|$ distributions.

Tagger	$\varepsilon(\%)$	$\mathcal{D}_u$	$\varepsilon\mathcal{D}_u^2(\%)$	$\mathcal{D}'_d$
Muon ($\|d\| > 0.3$)	7.10 ± 0.09	0.444 ± 0.015	1.400 ± 0.096	0.463 ± 0.028
Electron ($\|d\| > 0.3$)	1.88 ± 0.05	0.445 ± 0.032	0.372 ± 0.054	0.324 ± 0.060
SVCharge ($\|d\| > 0.3$)	2.81 ± 0.06	0.338 ± 0.026	0.320 ± 0.050	0.421 ± 0.049
Combined ($\|d\| > 0.3$)	11.74 ± 0.11	0.419 ± 0.012	2.058 ± 0.121	0.434 ± 0.023
Combined(0.10< $\|d\|$ <0.20)	4.59 ± 0.08	0.104 ± 0.017	0.050 ± 0.016	0.079 ± 0.029
Combined(0.20< $\|d\|$ <0.30)	6.10 ± 0.09	0.234 ± 0.014	0.335 ± 0.042	0.212 ± 0.024
Combined(0.30< $\|d\|$ <0.45)	3.98 ± 0.07	0.361 ± 0.018	0.519 ± 0.052	0.364 ± 0.032
Combined(0.45< $\|d\|$ <0.60)	4.77 ± 0.07	0.504 ± 0.016	1.211 ± 0.077	0.489 ± 0.030
Combined(0.60< $\|d\|$ <1.00)	1.17 ± 0.04	0.498 ± 0.031	0.290 ± 0.038	0.572 ± 0.056

Table 4.6: Tagging performance for events with reconstructed B^+ for different taggers and subsamples. For comparison, the dilution $\mathcal{D}'_d$ measured in the D^* sample with addition of wrong sign $\mu^+\nu\bar{D}^0\pi^+$ events is also shown.

Tagger	Δm_d	$f_{c\bar{x}}$
Muon	0.502 ± 0.028	0.013 ± 0.010
Electron	0.481 ± 0.067	0.058 ± 0.045
SV Charge	0.553 ± 0.053	0.096 ± 0.050
Multidim	0.502 ± 0.026	0.031 ± 0.014
Combined($\|d\| > 0.3$)	0.513 ± 0.023	0.033 ± 0.013
Combined($0.10 < \|d\| < 0.20$)	0.506 ± 0.209	0.495 ± 0.505
Combined($0.20 < \|d\| < 0.35$)	0.523 ± 0.064	0.021 ± 0.025
Combined($0.35 < \|d\| < 0.45$)	0.531 ± 0.042	0.063 ± 0.038
Combined($0.45 < \|d\| < 0.60$)	0.510 ± 0.032	0.010 ± 0.010
Combined($0.60 < \|d\| < 1.00$)	0.456 ± 0.049	0.032 ± 0.026

Table 4.7: Measured value of Δm_d and $f_{c\bar{c}}$ for different taggers and subsamples.

single measurement of $\Delta m_d$is taken using the combined tagger with a $|d| > 0.3$ cut:

$$\begin{aligned}\varepsilon\mathcal{D}_d^2 &= (2.19 \pm 0.22)\% \\ \Delta m_d &= 0.513 \pm 0.023\ ps^{-1} \\ f_{c\bar{c}} &= (3.3 \pm 1.3)\% \end{aligned} \tag{4.31}$$

The study allowed the assumption that $\mathcal{D}_u = \mathcal{D}_d$ to be tested. Tables 4.6 and 4.5 show the measured dilutions for the B^+ and B_d^0 components for a range of $|d|$ cuts. The results show a general tendency for the measured B_d^0 dilution to be greater than the measured B^+ dilution.

This can be explained by the suppression of fake events in the reconstructed $B \rightarrow \mu^+\nu\bar{D}^{*-}X$ decays relative to the $B \rightarrow \mu^+\nu\bar{D}^0X$ decays. In both reconstructions there is a possibility to form a fake B-candidate by combining a "real" D^0-candidate with a random muon, for which M($K\pi\mu$) lies within the B-mass region. As the muon charge is used to determine the decay flavour, these events will be randomly tagged and tend to reduce the measured sample dilution. In the D^*-sample the extra requirement of charge correlation between the muon and additional pion reduces this background.

For a true comparison of tag performance between the two samples a second D^*-sample was constructed without making a requirement on the charge of the additional pion. The results of this study can be seen in the $\mathcal{D}'_d$ column of Table 4.6.

As expected the measured dilutions for the D^*-sample are smaller when no requirement on the pion charge is made, and the agreement between the measured tag performance for B^+ and the B_d^0 decays improves. For the B_s^0-analysis the decay $B_s^0 \rightarrow D_s^-\mu^+\nu_\mu X$, where $D_s^- \rightarrow \phi\pi^-$ and $\phi \rightarrow K^+K^-$ is reconstructed. This is the analogue of the decay $B \rightarrow \mu^+\nu\bar{D}^{*-}X$, where $D^{*-} \rightarrow D^0\pi^-$ and $D^0 \rightarrow K^+\pi^-$, and so the the $\mathcal{D}_d$ values are applicable for the B_s-mixing analysis tagger calibration.

A check was made that the tagging performance is independent of the P_T of the reconstructed B-meson. The P_T^B spectrum can be seen in Figure 4.19. The

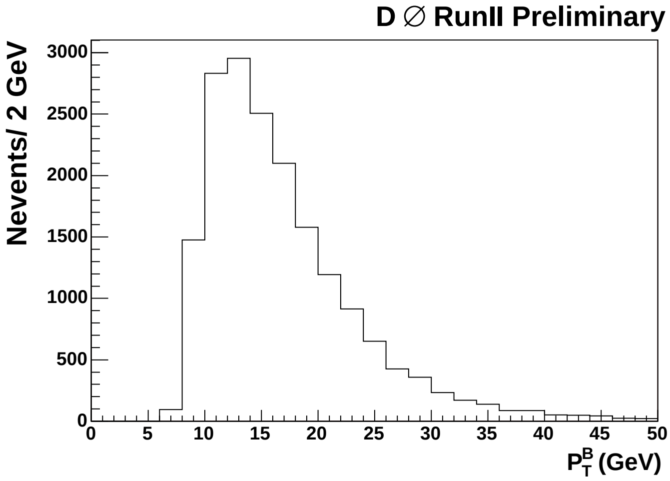

Figure 4.19: P_T distribution of the reconstructed B^+ candidates

predominately unmixed events with $200\mu m < x^M < 500\mu m$ were divided into two subsets using a P_T^B at 16 GeV. The resulting asymmetry for both D^0- and D^*-samples using events tagged with $|d| > 0.3$ can be seen in Tables 4.8 and 4.9. No dependance of the asymmetry on P_T^B is observed.

Sample	N_{nosc}	N_{osc}	A
All	1903 ± 57	777 ± 40	0.420 ± 0.024
$P_T^B < 16$	1226 ± 45	467 ± 31	0.449 ± 0.030
$P_T^B > 16$	677 ± 35	310 ± 25	0.371 ± 0.041

Table 4.8: The asymmetries for two samples B^+ candidates using a $P_T > 16$ GeV cut. No dependence of the asymmetry with P_T is observed.

Sample	N_{nosc}	N_{osc}	A
All	835 ± 33	372 ± 22	0.384 ± 0.030
$P_T^B < 16$	496 ± 25	226 ± 17	0.373 ± 0.039
$P_T^B > 16$	339 ± 21	145 ± 14	0.401 ± 0.049

Table 4.9: The asymmetries for two samples B^0 candidates using a $P_T > 16$ GeV cut. No dependence of the asymmetry with P_T is observed.

Table 4.5 shows the measured dilution $\mathcal{D}_d$ for tagged events divided in bins of $|d|$. As expected the measured dilution increases as the $|d|$ interval increases and the fitted relationship between $|d|$ and $\mathcal{D}_d$ is used to calibrate the dilution in the event-by-event fit for the B_s^0 mixing analysis.

The tagging power from each $|d|$ bin can be summed to give an estimate of the total tagging power:

$$\varepsilon\mathcal{D}_d^2 = (2.48 \pm 0.21)\% \tag{4.32}$$

To utilise the summed tagging power in the measurement of Δm_d, a fit was made to the asymmetries simultaneously across all bins of $|d|$, giving the best measurement:

$$\Delta m_d \quad = \quad 0.506 \pm 0.020 \; ps^{-1} \tag{4.33}$$

The fitted fraction of $c\bar{c}$-background in this sample was found to be:

$$f_{c\bar{c}} \quad = \quad (2.2 \pm 0.9)\% \tag{4.34}$$

This result can be compared with the measurement using the combined tagger with a $|d| > 0.3$ cut (Equation 4.31). The measured values of $f_{c\bar{c}}$ are in agreement and there is a 10% improvement in the precision of the Δm_d measurement.

4.5 Systematic errors

Tables 4.10 and 4.11 summarise the results of the studies of the systematic errors on the measured values of $\mathcal{D}$ and Δm_d. The sources of systematic errors were studied by repeating the analysis with the following variations:

- The B-meson lifetimes and branching ratios into the considered decay channels were varied by one sigma of their PDG values.
- The VPDL resolution function, extracted from a study of simulated events was multiplied by factors of 0.8 and 1.2, which exceeds the observed discrepancy between Monte Carlo events and data.

- The error due to dependency of the K-factors on the reconstructed B-momentum was calculated. The possible systematic error from neglecting this dependence was estimated by recalculating the K-factors using different selection cuts on the momentum of the B daughters. Neglecting the $P_T^{D^0} > 5$ GeV cut or placing an additional cut $P_T^{\mu} > 4$ GeV, changed the mean value of the K-factor distributions by less than 2%. The effect of shifting the K-factor distributions in this way was studied.

- The ratio for reconstructing D^{**} relative to the D^* and D^0 channels depends on the different kinematic properties of the decays. This was estimated using a study on simulated events. To estimate the uncertainty in the relative reconstruction efficiency for these channels, the study was repeated with different cuts on $P_T^{D^0}$ and P_T^{mu}. This resulted in a 12% change in the reconstruction efficiencies. A further check was made by changing from the $ISGW2$[72] to $HQET$[74] model to describe semileptonic B-decay, which gave a smaller variation to the reconstructed efficiency. Therefore the systematic study varied the efficiency to reconstruct $B \to \mu^+ \nu D^{**-}$ and $B \to \mu^+ \nu \bar{D}^{**0}$ channels by ±12%.

- The estimation of the fraction of the number of D^0 events contributing to the D^*-sample, as described in section 4.3.2, was varied from 4% by its estimated error 0.85%.

- The error arising from the use of fixed fit parameters for the $K\pi$ invariant mass distribution was estimated. The study of the fit parameters displayed no variation in the width and position of the signal and background peaks above the 3σ level. Therefore as a systematic check each of the fixed parameters were varied by 3σ from their fit to the all events sample.

- The bin width used to bin the $K\pi$ mass distribution histogram was varied from 0.020 GeV to smaller (0.016 GeV) and larger (0.027 GeV) values. This was done to check that the result was independent of the choice of bin width.

The largest source of uncertainty for Δm_d was the variation of the K-factor distribution by 2%. The corresponding change in Δm_d is also 2%, as expected, since shifting the mean of the K-factor distribution produces a proportional change in measured VPDL for each event. The variation of $Br(B \to D^{*}\pi\mu\nu X)$ was also a significant source of uncertainty. The overall uncertainty from the fitting procedure was $\approx 15\%$ of the total systematic error on Δm_d.

The sources of significant variation for the $\mathcal{D}$ measurement were different. The change of R^{**} from 0.35 to 0 and 1, caused the largest variation to the measured dilution $\mathcal{D}$. The fit procedure systematic was substantial, and for most bins of dilution contributed at a level of $> 50\%$ of the total systematic error.

4.6 Conclusions

The likelihood-based opposite-side tagging algorithm was tested on samples of B^0 and B^+ decays. The dilutions, $\mathcal{D}(B^+)$ and $\mathcal{D}(B^0)$, were measured to be consistent within statistical errors.

By splitting the sample into bins according to the tagging variable $|d|$ and measuring the tagging power as the sum of individual tagging power in all bins, the following result was obtained

$$\varepsilon\mathcal{D}^2 = 2.48 \pm 0.21(\text{stat.})\ ^{+0.08}_{-0.06}(\text{syst})\ \%$$

Using a simultaneous fit to events in all $|d|$ bins the mixing parameter Δm_d parameter was measured to be:

$$\Delta m_d = 0.506 \pm 0.020\ (\text{stat}) \pm 0.016\ (\text{syst})\ \text{ps}^{-1}$$

which is in good agreement with the world average value of $\Delta m_d = 0.507 \pm 0.003(\text{sys}) \pm 0.003(\text{stat})\ \text{ps}^{-1}$ [18].

	default	variation		$\Delta m_d/\text{ps}^{-1}$	
		(a)	(b)	(a)	(b)
$Br(B^0 \rightarrow D^{*-}\mu^+\nu)$	5.44	-0.23	0.23	.002	-.002
$Br(B \rightarrow D^*\pi\mu\nu X)$	1.07	-0.17	0.17	-.0078	.0078
R^{**}	0.35	0.0	1.0	.0006	-.0012
B lifetimes	.05022	-.00054	.00054	.0008	-.0008
Resolution function	—	÷1.2	÷0.8	.0021	-.0021
Alignment	—	$-10\mu m$	$+10\mu m$	± 0.004	-
K-Factor	—	-2%	+2%	.0098	-.0094
Efficiency	—	-12%	+12%	-.0054	.0052
Fraction D^0 in D^*	4%	3.15%	4.85%	-.0020	+.0030
Fit Procedure	See split below				
Bin width	2 MeV	1.6	2.67	.0009	.0014
Parameter μ_0	—	-3σ	3σ	-.0001	.0001
Parameter $\frac{\sigma_R+\sigma_L}{2}$	—	-3σ	3σ	-.0001	—
Parameter $\frac{\sigma_R-\sigma_L}{\sigma_R+\sigma_L}$	—	-3σ	3σ	-.0001	.0001
Parameter μ_1	—	-3σ	3σ	-.0016	.0015
Parameter $\frac{\sigma_1+\sigma_2}{2}$	—	-3σ	3σ	-.0006	.0006
Parameter R	—	-3σ	3σ	-.0005	.0004
Parameter $(\mu_2 - \mu_1)$	—	-3σ	3σ	.0006	-.0007
Parameter $\frac{\sigma_1-\sigma_2}{\sigma_1+\sigma_2}$	—	-3σ	3σ	—	—
Fit Procedure		Overall		+.0023 -.0019	
Total				+.0158 −.0158	

Table 4.10: Systematic uncertainties Δm_d.

	default	variation		$\mathcal{D}(B^0)$ $0.1 < \|d\| < 0.2$		$\mathcal{D}(B^0)$ $0.2 < \|d\| < 0.3$		$\mathcal{D}(B^0)$ $0.3 < \|d\| < 0.45$		$\mathcal{D}(B^0)$ $0.45 < \|d\| < 0.6$		$\mathcal{D}(B^0)$ $0.6 < \|d\| < 1\ .0$	
		(a)	(b)	(a)	(b)	(a)	(b)	(a)	(b)	(a)	(b)	(a)	(b)
$Br(B^0 \to D^{*-}\mu^+\nu)$	5.44	-0.23	0.23	—	—	—	-.001	.001	—	.001	-.001	.001	-.001
$Br(B \to D^*\pi\mu\nu X)$	1.07	-0.17	0.17	.0004	-.0004	-.0011	.0011	-.0019	.0021	-.0020	.0021	-.0008	.0028
R^{**}	0.35	0.0	1.0	-.0009	.0016	-.0027	.0048	-.0042	.0079	-.0057	.0105	-.0066	.0124
B lifetimes	.05022	-.00054	.00054	—	-.0001	.0001	-.0002	.0003	-.0001	.0003	-.0003	.0014	-.0003
Resolution function	—	÷1.2	÷0.8	.0005	-.0006	.0010	-.0012	.0020	-.0021	.0024	-.0028	.0028	-.0032
Alignment	—	-10 μm	10 μm	-0.004	0.004	-0.004	0.004	-0.004	0.004	-0.004	0.004	-0.004	0.004
K-Factor	—	-2%	+2%	—	—	-.0001	—	—	.0001	-.0001	—	—	—
Efficiency	—	-12%	+12%	.0006	-.0007	-.0008	.0006	-.0012	.0011	-.0013	.0010	-.0021	.0019
Fraction D^0 in D^*	4%	3.15%	4.85%	—	.0010	-.0010	—	-.0010	.0010	-.0010	.0010	-.0010	.0010
Fit Procedure	See split below												
Bin width	2 MeV	1.6	2.67	-.0026	.0002	-.0024	.0014	-.0001	.0027	.0037	.0038	.0089	.0087
Parameter μ_0	—	-3σ	3σ	-.0003	.0002	.0001	-.0001	.0001	.0001	-.0002	.0001	-.0007	.0007
Parameter $\frac{\sigma_R+\sigma_L}{2}$	—	-3σ	3σ	.0002	-.0002	.0001	-.0001	.0004	-.0003	—	-.0001	-.0002	.0001
Parameter $\frac{\sigma_R-\sigma_L}{\sigma_R+\sigma_L}$	—	-3σ	3σ	-.0005	.0005	.0002	-.0001	.0002	.0001	-.0002	.0001	-.0015	.0011
Parameter μ_1	—	-3σ	3σ	-.0009	.0010	-.0017	.0018	.0023	-.0015	.0006	-.0005	-.0004	-.0004
Parameter $\frac{\sigma_1+\sigma_2}{2}$	—	-3σ	3σ	.0008	-.0005	.0014	-.0009	.0037	-.0034	-.0013	.0017	-.0099	.0068
Parameter R	—	-3σ	3σ	.0015	-.0011	.0029	-.0024	.0030	-.0027	.0013	-.0011	-.0046	.0035
Parameter $(\mu_2 - \mu_1)$	—	-3σ	3σ	—	-.0003	.0008	-.0011	-.0001	.0006	-.0003	.0002	.0008	-.0003
Parameter $\frac{\sigma_1-\sigma_2}{\sigma_1+\sigma_2}$	—	-3σ	3σ	-.0001	—	-.0004	.0003	.0002	-.0002	-.0004	.0004	-.0006	.0010
Fit Procedure		Overall		+.0021 -.0031		+.0040 -.0041		+.0060 -.0046		+.0044 -.0019		+.0119 -.0111	
Total				+.0049 -.0052		+.0077 -.0066		+.0111 -.0081		+.0125 -.0081		+.0182 -.0140	

Table 4.11: Systematic uncertainties $\mathcal{D}(B^0)$.

Chapter 5

B_s Mixing Analysis

The observation of B_s^0 oscillations is a major Physics goal of the DØ experiment. The measurement of the B_s^0 mixing frequency (Δm_s) cannot be performed at the B-factories which operate at the $\Upsilon(4s)$ resonance, and is currently only accessible at the Tevatron. Limits on Δm_s can be translated to give theoretically clean constraints on the CKM matrix used to describe CP-violation in the Standard Model. B_s^0-mixing analyses are more difficult than B_d^0-mixing analyses due to the smaller B_s production cross section and faster oscillation frequency at which the K-factor momentum correction and the decay length resolution become limiting factors.

5.1 Sample selection

The B_s mixing analysis used a sample of $B_s^0 \to D_s^- \mu^+ \nu_\mu X$ decays, where $D_s^- \to \phi\pi^-$ and $\phi \to K^+K^-$. There were two stages in event selection. The first stage collected a loose set of candidate events using kinematic and track quality cuts. This sample was then purified, using a likelihood ratio method to separate the signal from background events.

5.1.1 Selection cuts

Candidate events were required to contain a muon candidate which satisfied:

- $P_T^{\mu} > 2$ GeV.
- $P^{\mu} > 3$ GeV.
- At least one hit in both the SMT and CFT.
- Have hits in at least two layers of the muon system.

The tracks in these events were clustered into jets according to the DURHAM[67] algorithm, using a P_T cutoff at 15 GeV. The tracks associated within the muon jet were then utilised in the search for a D_s^- candidate.

Two tracks with opposite charge were used to reconstruct the $\phi \to K^+K^-$ decay. Each track was required to have hits in both the SMT and CFT and have $P_T^K > 0.7$ GeV, and the invariant mass of the K^+K^- system had to satisfy $1.004 < M(K^+K^-) < 1.0034$ GeV. The transverse (ϵ_T) and longitudinal (ϵ_L) components of the kaon track impact parameters with respect to the primary vertex, and the associated uncertainties, were required to satisfy:

$$\sqrt{(\epsilon_T/\sigma(\epsilon_T))^2 + (\epsilon_L/\sigma(\epsilon_L))^2} > 4 \tag{5.1}$$

The pion track was then searched for, required to have opposite charge to the muon, hits in both the SMT and CFT, and $P_T^{\pi} > 0.5$ GeV.

The three tracks were required to form a common D_s^- vertex with a χ^2 fit < 16. The measured distance from the primary to D_s^--vertex ($D^{PV\to D}$) and its uncertainty was required to satisfy $D^{PV\to D} > 4 \cdot \sigma(D^{PV\to D})$. The angle between the direction of $D^{PV\to D}$ and the D_s^--momentum ($P^{D_s^-}$) was required to satisfy $\cos P^{D_s^-}, D^{PV\to D} > 0.9$.

The muon and D_s^- candidate were required to form a common B_s^0-vertex with a χ^2-fit < 9. The momentum and mass of the B-candidate were calculated using the muon and D_s^- system. A cut on the resulting B-candidate mass was made, requiring $2.6 < M(\mu^+ D_s^-) < 5.4$ GeV.

The transverse B-decay length ($D^{PV\to B}$) was calculated, along with its uncertainty. In the case that $D^{PV\to B} > 4\cdot\sigma(D^{PV\to B})$, an angular cut was made on the angle between the direction of $D^{PV\to B}$ and the B-momentum (P^B), $\cos(P^B, D^{PV\to B}) > 0.95$. The distance $D^{PV\to D}$ was allowed to be greater than $D^{PV\to B}$ provided the uncertainty in the measurement of $D^{B\to D}$ was such that $D^{B\to D} < 2\cdot\sigma(D^{B\to D})$.

5.1.2 Signal optimisation

The likelihood ratio method described in Section 4.2.1 was used to suppress background events. For this application the variables used to distinguish between signal and background events were as follows:

- Helicity angle between $P^{D_s^-}$ and P^{K^+} in the K^+K^- centre of mass frame.
- Isolation of the B_s candidate defined as:

  $$\frac{P(\mu^+D_s^-)}{(P(\mu^+D_s^-)+\sum_i P_i)} \tag{5.2}$$

  Here the sum $\sum_i$ is over all other tracks within the cone $\sqrt{(\Delta\phi)^2+(\Delta\eta)^2} < 0.5$, where ϕ and η are the azimuthal angle and pseudorapidity of the B-candidate respectively.
- Transverse momentum P_T of the D_s^- candidate.
- Invariant mass of the μD_s^- system.
- χ^2 fit of the tracks forming the D_S^- vertex.
- Invariant mass of the K^+K^- system.

Probability density functions (PDFs) of each of the variables were constructed for signal and background samples of events. The signal sample consisted of events in which $M(K^+K^-\pi^-)$ fell in the interval from 1.92 to 2.00 GeV. The background sample consisted of events in the side-bands to the signal peak, with $M(K^+K^-\pi^-)$

in the intervals 1.75 to 1.79 GeV and 2.13 to 2.17 GeV. The side-band intervals were chosen such that the number of background events under the signal peak was equal to the number of background events in the side-bands. The PDF for background events was taken directly from the background sample PDF, and the PDF for the signal events was constructed by taking the signal sample PDF and subtracting the PDF for the background events.

The signal and background event PDFs for each variable were compared to determine the likelihood ratio,

$$R^i = P^i_{sig}/P^i_{bkg} \tag{5.3}$$

where P^i_{sig} and P^i_{bkg} are the respective probabilities for the event to originate from a signal decay or background process, given the measured value of the ith distinguishing variable. The ratios were combined into an overall likelihood ratio:

$$R = P^{tot}_{sig}/P^{tot}_{bkg} = \prod_{i=1}^{n} P^i_{sig}/P^i_{bkg} \tag{5.4}$$

where the sum is taken over all discriminating variables. A cut was made on candidate events based on the value of the combined likelihood, in order to maximise the quantity $\frac{N_{sig}}{\sqrt{N_{sig}+N_{bkg}}}$ where N_{sig} is the number of events in the signal sample, and N_{bkg} is the number of events in the sidebands. This was found to occur for the selection cut at $-\log_{10}(P_{sig}/P_{bkg})) > 0.12$. After this selection, the sample contained 26710 ± 556 D_s^- events and 7422 ± 281 D^- events.

The events were then flavour tagged using the combined tagger described in Section 4.2. The value of predicted dilution, d, was translated to a calibrated dilution, $\mathcal{D}(d)$, constructed by a parameterised fit to the dilutions measurements from the B_d analysis. The invariant $M(K^+K^-\pi^-)$ mass plots for the selected events, and the subset of tagged events are shown in Figure 5.1.

5.2 Fitting procedure

The tagged events with $1.72 < M(K^+K^-\pi^-) < 2.22$ GeV were fitted using an unbinned fit on an event-by-event basis. A probability density function describing the

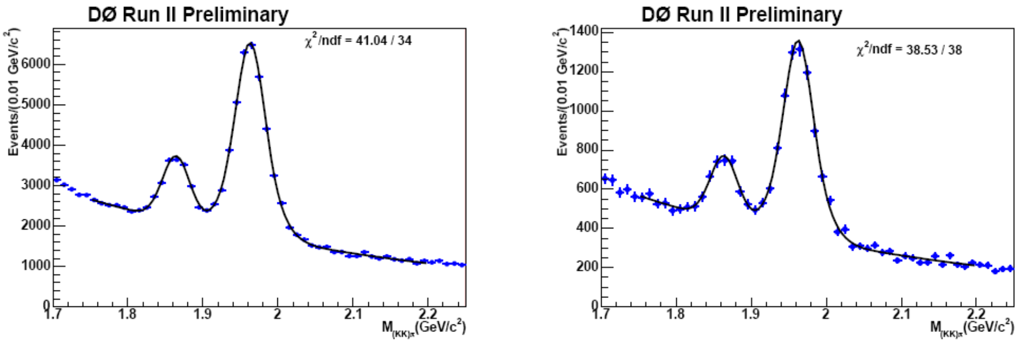

Figure 5.1: $M(K^+K^-\pi^-)$ invariant mass distribution for the untagged (left) and tagged (right) B_s^0 sample. The left and right peaks correspond to the μ^+D^- and $\mu^+D_s^-$ candidates respectively. The fitting curve uses a single Gaussian to describe the μ^+D^- signal and double Gaussian for the $\mu^+D_s^-$ signal. The background is modelled by an exponential function.

variables measured for each event was constructed as a function of the B_s mixing frequency. This included the necessary corrections for experimental effects and consideration of the potential origin of each event. This method effectively weights each event in the analysis according to its quality, and maximises the ability to detect B_s oscillations.

The following processes were considered as the possible sources for each event in the data sample:

- $\mu^+D_s^-$ $(\rightarrow \phi\pi^-)$ signal.
- μ^+D^- $(\rightarrow \phi\pi^-)$ signal.
- μ^+D^- $(\rightarrow K\pi\pi^-)$ reflection[1].
- combinatorial background.

The PDFs for each process were constructed with respect to the following variables:

- VPDL measurement, x^M.

---

[1] The signal reflection is due to a mass shift of 2 GeV caused by misassignment of the kaon mass to the pion.

- estimated uncertainty in VPDL measurement, σ_{x^M}.
- predicted dilution, d, of the tag.
- mass of the reconstructed D_s-candidate, M.
- value of the likelihood ratio $R = P_{sig}/P_{bkg}$ calculated during the sample selection process.

The overall PDF for each possible source, f_i, was constructed by combining separate PDFs for each of the measured variables:

$$f_i = P_i^{x^M}(x^M, \sigma_{x^M}, d) P_i^{\sigma_{x^M}} P_i^d P_i^M P_i^R \tag{5.5}$$

These were then summed over all i sources to give the total PDF F_n for each event:

$$F_n = \sum_i \mathcal{F}_i \cdot f_i \tag{5.6}$$

where $\mathcal{F}_i$ is the fraction of events resulting from the source i, $\sum_i \mathcal{F}_i = 1$ and the summation is for $i = \mu^+ D_s^-,\ \mu^+ D^-,\ \mu^+ D^-_{refl}$.

The likelihood $\mathcal{L}$ is defined as:

$$\mathcal{L} = -2 \sum_n lnF_n, \tag{5.7}$$

where the sum is taken over all n tagged events. This likelihood was minimised using MINUIT [75] in order determine required fit parameters.

The fractions $\mathcal{F}_{\mu^+ D_s^-}$, $\mathcal{F}_{\mu^+ D^-}$ and $\mathcal{F}_{comb\_bkg}$ were determined from the mass fit to all tagged events shown in Figure 5.1 (a). The fraction $\mathcal{F}_{\mu^+ D^-_{refl}}$ was determined from a fit to the full sample of events before tagging shown in Figure 5.1 (b), in order that the statistical fluctuations were sufficiently small for fitting. The resulting fits predicted that the number of $\mu^+ D^-$ reflected events was less than 1% of the number of signal $\mu^+ D_s^-$ events.

5.2.1 Signal PDF

The PDFs $P_i^{\sigma_{xM}}$, P_i^M and P_i^R for the $\mu^+ D_s^-$ signal events were constructed using experimental data. These PDFs were also used for the $\mu^+ D^-$ and $\mu^+ D^-_{refl}$ events, except for the mass distribution for the $\mu^+ D^-_{refl}$ events which was determined using Monte Carlo events.

The PDFs $P_i^{\sigma_{xM}}$, P_i^M and P_i^R for the combinatorial background were also constructed from data, taking into account the the dependance of the background slope on the mass distribution, $P^M_{comb\ bkg} = P^M_{comb\ bkg}(x^M)$.

The PDFs describing the x^M dependence for oscillating and non-oscillating signal events were determined by following a similar procedure to that used to construct $N^{osc,nos}_{B_d^0}$, described in section 4.3.2. The equations describing the PDF for oscillated and non-oscillated B_s decays, analogous to Equation 4.21, were modified to include B_s^0 oscillations explicitly, and a dependence on the predicted dilution d:

$$p_s^{nos}(x, K, d) = \frac{K}{c\tau_{B_s^0}} \exp(-\frac{Kx}{c\tau_{B_s^0}}) \cdot 0.5 \cdot (1 + \mathcal{D}(d) \cos(\Delta m_s K x/c)) \quad (5.8)$$

$$p_s^{osc}(x, K, d) = \frac{K}{c\tau_{B_S^0}} \exp(-\frac{Kx}{c\tau_{B_s^0}}) \cdot 0.5 \cdot (1 - \mathcal{D}(d) \cos(\Delta m_s K x/c)) \quad (5.9)$$

Here x is the visible particle decay length (VPDL), K is the K-factor correction, and $\mathcal{D}(d)$ is the calibrated dilution.

Corresponding PDFs were constructed for the B_u and B_d channels, which contribute to the signal through $B \to D D_s^-$ with $D \to \mu^+ X$ processes, and also for the $B_s \to D_s D_s$ channel.

In order to translate from the real VPDL, x, to measured VPDL, x^M, the PDF in each channel j was convoluted with the K-factor distribution $D_j(K)$ and the detector resolution function $G(x - x^M, \sigma_{x^M})$.

The K-factor distributions for each decay channel were determined from Monte Carlo events, with generator information used to find the true value of P_T^B. Figure 5.2 shows the resulting K-factor distributions for the B_s^0 semileptonic decay channels.

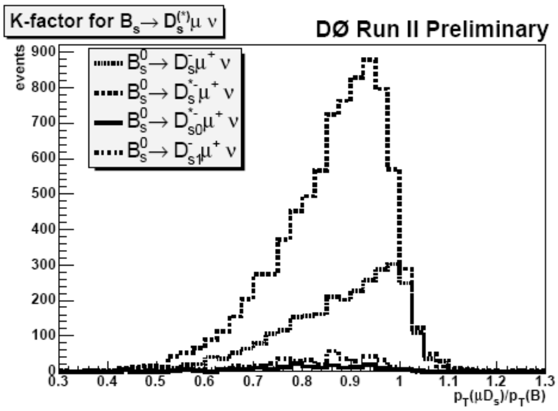

Figure 5.2: K-factor distributions used for the semileptonic B_s^0 decays. $P_T(B)$ is taken from Monte Carlo truth information, $P_T(\mu D_s)$ is calculated from the reconstructed tracks.

The resolution function $G(x - x^M, \sigma_{x^M})$ was described by a Gaussian:

$$G(x - x^M, \sigma_{x^M}) = \frac{1}{\sqrt{2\pi}\sigma_{x^M}} \exp(-\frac{(x - x^M)^2}{2\sigma_{x^M}^2}) \tag{5.10}$$

Here the uncertainty in VPDL, σ_{x^M}, was estimated on an event-by-event basis during the vertex fitting procedure. This uncertainty was adjusted by a scale correction factor for accurate performance determined using a data sample of J/ψ candidates.

There are no explicit decay length cuts on the B_s-meson candidate, but the impact parameter cuts on the daughter particles mean that the reconstruction efficiency is dependent on VPDL. This dependence was studied using Monte Carlo events to determine the efficiency $Eff_j(x^M)$ for each decay channel, j, which was then applied in the PDF calculation. Figure 5.3 shows the resulting efficiency function for $B_s \rightarrow \mu^+ D_s^- X$ events.

In addition to the B-decay channels considered there is a significant $c\bar{c}$ background. This has the same origin as the $c\bar{c}$ background observed in the B_d mixing analysis, consisting of events in which a fake B-meson candidate is formed from a muon and D_s^- meson which originate from different c quarks. It is assumed that this background is tagged oscillated or non-oscillated indiscriminately. The PDF $P_{c\bar{c}}^{osc,nos}(x^M)$ which describes these events was constructed using Monte Carlo events.

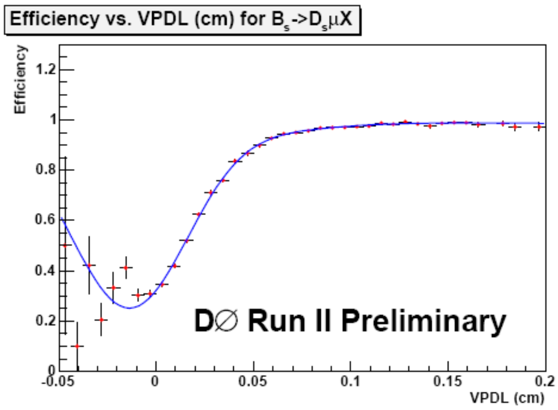

Figure 5.3: Efficiency to reconstruct the $B_s \to \mu^+ D_s^- X$ decay as a function of VPDL. The fall in efficiency at short VPDL is due to the significance cuts on the track impact parameters.

The final PDF for oscillated and non-oscillated signal events, $P^{osc,nos}_{\mu D_s}$ is given by:

$$P^{osc,nos}_{\mu D_s}(x^M, \sigma x^M, d) = (1 - \mathcal{F}_{c\bar{c}}) \sum_j Br_j \cdot P^{osc,nos}_j(x^M, \sigma x^M, d) + \mathcal{F}_{c\bar{c}} \cdot P^{osc,nos}_{c\bar{c}}(x^M) \tag{5.11}$$

Here $\mathcal{F}_{c\bar{c}}$ is the fraction of $c\bar{c}$ events present and the sum $\sum_j$ is taken over all decay channels contributing fraction Br_j to the μD_s signal. The decision to use the PDF for non-oscillated or oscillated events is made with respect to the sign of $(d \cdot q_\mu)$:

$$d \cdot q_\mu > 0 \quad : \quad P^{x^M}(x^M, \sigma x^M, d) = P^{osc}_{\mu D_s}(x^M, \sigma x^M, d) \tag{5.12}$$

$$d \cdot q_\mu < 0 \quad : \quad P^{x^M}(x^M, \sigma x^M, d) = P^{nos}_{\mu D_s}(x^M, \sigma x^M, d) \tag{5.13}$$

The PDG [16] values were used for the following input B-meson parameters: $c\tau_{B^+} = 501\mu$m, $c\tau_{B^0} = 501\mu$m, $\Delta m_d = 0.502$ps^{-1}. PDG values were also used for the branching rates, unless not available, in which case the theoretically motivated values from the EvtGen package [76] were used. The B_s lifetime was fitted from the data.

These inputs were used to determine that the fraction of $B^0_s \to \mu^+ D^-_s X$ events in the signal peak is $(85.6 \pm 3.3)\%$. This includes contributions from D^{*-}_s, D^{*-}_{s0}, D^{*-}_{s1} and $\tau^+ \to \mu^+$ decays, and the effect of reconstruction efficiencies. The other components of the signal peak consist of decays which do not exhibit oscillations at the Δm_s mixing frequency, e.g. $B \rightarrow D^+_{(s)} D^-_s X$ where $D^+_{(s)} \rightarrow \mu^+ \nu X$.

5.2.2 Background PDF

The PDF for the combinatorial background, $P_{comb\_bkg}(x^M, \sigma_{x^M}, d)$, was constructed using three distinct background sources.

- Prompt background originating from the primary vertex.
- Background events formed by tracks which form a fake vertex by chance. These were assumed to be distributed symmetrically around the primary vertex.
- Long lived background, described by a exponential decay length $c\tau_{bkg}$. This was modelled using three components distinguished by their response to the initial state tagging. These were: a tag insensitive component; a component sensitive to tagging but not oscillatory; and a component sensitive to tagging which oscillated at the Δm_d frequency.

The decay parameters and relative fractions of each component background source were determined by a fit to the total tagged data sample.

5.3 Amplitude fit method

The amplitude fit method is a modification of the standard likelihood fit method. In a likelihood fit for Δm_s, the likelihood, $\mathcal{L}$ (Equation 5.7), is minimised with respect to the mixing frequency in Equation 5.8 and 5.9. To perform the amplitude fit an extra term is added to these equations, describing the amplitude of the oscillations, $\mathcal{A}$:

$$p^{nos}_s(x, K, d) = \frac{K}{c\tau_{B^0_s}} \exp(-\frac{Kx}{c\tau_{B^0_s}}) \cdot 0.5 \cdot (1 + \mathcal{D}(d) \cdot \mathcal{A} \cos(\Delta m_s Kx/c)) \tag{5.14}$$

$$p^{osc}_s(x, K, d) = \frac{K}{c\tau_{B^0_S}} \exp(-\frac{Kx}{c\tau_{B^0_s}}) \cdot 0.5 \cdot (1 - \mathcal{D}(d) \cdot \mathcal{A} \cos(\Delta m_s Kx/c)) \tag{5.15}$$

The likelihood fit is performed at a fixed value of Δm_s, to minimise $\mathcal{L}$ and fit the amplitude, $\mathcal{A}$, for oscillations at this frequency. The associated error $\sigma\mathcal{A}$ is determined from the fit. The fit is then repeated with small increments to Δm_s until the full region of sensitivity is covered. The expected value of the amplitude is $\mathcal{A} = 1$ at the true B_s^0-mixing frequency, and $\mathcal{A} = 0$ elsewhere.

The amplitude scan can be be used to set limits on Δm_s. In general the measured $\sigma_{\mathcal{A}}$ increases with Δm_s. This is because the experimental power to resolve Δm_s at faster frequencies is weaker, due to the experimental resolution and the K-factor correction.

The expected lower limit or *sensitivity* of the analysis is set at the value of Δm_s where the error $\sigma_{\mathcal{A}}$ is sufficient to enable the measurement of $\mathcal{A}$ to fluctuate to one from a true value of zero,

$$1.645 \cdot \sigma_{\mathcal{A}} = 1 \tag{5.16}$$

where the limit is taken at the 95% confidence level, assuming the uncertainty in $\mathcal{A}$ is Gaussian.

The measured lower limit of the analysis is set at the value of Δm_s at which the error $\sigma_{\mathcal{A}}$ is sufficient to cause the measured value of $\mathcal{A}$ to fluctuate to one from its measured value, i.e.:

$$\mathcal{A} + 1.645 \cdot \sigma_{\mathcal{A}} = 1 \tag{5.17}$$

again this limit is made with a 95% confidence level, assuming the uncertainty in $\mathcal{A}$ to be Gaussian.

The advantage of using the amplitude fit method is in combining results from different decay channels and other experiments to set joint limits. The measurements of $\mathcal{A}$ from different analyses are statistically independent and so can be averaged to produce an amplitude scan from which combined limits can be taken. However, in order to produce the correct result it is important to calculate the combined values of $\sigma_{\mathcal{A}}$ correctly, with careful consideration given to common sources of systematic errors.

5.3.1 Systematic errors

The possible sources of systematic error were studied by repeating the amplitude fit at each fixed value of Δm_s, with modifications to the analysis made to determine the systematic uncertainties. The resulting variations in $\mathcal{A}$ and $\sigma_{\mathcal{A}}^{stat}$ were used to calculate a combined $\sigma_{\mathcal{A}}^{stat,syst}$ accounting for both statistical and systematic uncertainties. The results of this study are illustrated in Table 5.1.

The variations assigned to the branching rates for each channel were sufficient to cover both experimental and theoretical uncertainties, and the possible effects of trigger efficiency biases.

The sources studied with the largest contribution to the systematic uncertainties were found to be:

- adjustment of the fit to the signal distribution in VDPL.
- variation of the K-factor distribution means by 2%.
- recalculation of the measured scale factor correction, using the sample of J/ψ after a cut on the transverse muon momentum $P_T^{\mu} > 6$ GeV was applied.

The total contribution to $\sigma_{\mathcal{A}}$ from systematic variations was typically between 1/3 and 1/4 of the statistical uncertainty.

5.4 Results

The amplitude scan is shown in Figure 5.4. The expected limit was measured to be 14.4 ps^{-1} (statistical) and 14.1 ps^{-1} (statistical and systematic). However, the measured value of $\mathcal{A}$ in this region is less than zero, and this results in a larger measured limit of 15.0 ps^{-1} (statistical) and 14.8 ps^{-1} (statistical and systematic).

There is a peak in the amplitude at ~ 19 ps^{-1}, for which the value of $\mathcal{A} = 0$ is excluded at the 95% confidence level, suggesting that the oscillation frequency Δm_s might lie in this region.

Systematic variation studied	Δm_s value	7 ps^{-1}	13 ps^{-1}	19 ps^{-1}	25 ps^{-1}
–	measured $\mathcal{A}$	0.073	-0.459	2.749	0.018
–	measured $\sigma_{\mathcal{A}}$	0.231	0.504	1.068	1.920
branching rate	$\Delta\mathcal{A}$	-0.002	+0.010	-0.059	+0.009
$B \to D_s D_s$	$\Delta\sigma_{\mathcal{A}}$	-0.005	-0.010	-0.023	-0.040
branching rate	$\Delta\mathcal{A}$	-0.004	-0.011	+0.046	+0.011
$B \to D_s \mu X$	$\Delta\sigma_{\mathcal{A}}$	+0.004	+0.009	+0.019	+0.035
Resolution scale factor study	$\Delta\mathcal{A}$	+0.010	+0.029	-0.124	-0.019
repeated with P_T^μ	$\Delta\sigma_{\mathcal{A}}$	-0.011	-0.024	-0.054	-0.093
K-factor	$\Delta\mathcal{A}$	+0.001	+0.045	+0.207	-0.001
means shifted by 2%	$\Delta\sigma_{\mathcal{A}}$	+0.004	+0.011	+0.059	+0.050
K-factor distribution	$\Delta\mathcal{A}$	+0.001	+0.006	-0.003	-0.032
smoothed	$\Delta\sigma_{\mathcal{A}}$	+0.000	+0.002	-0.005	+0.009
K-factor from	$\Delta\mathcal{A}$	+0.001	+0.003	-0.021	-0.050
measured momentum	$\Delta\sigma_{\mathcal{A}}$	+0.001	+0.003	+0.006	-0.011
Fraction of peaking	$\Delta\mathcal{A}$	-0.001	-0.000	+0.012	+0.008
bkg in comb. bkg	$\Delta\sigma_{\mathcal{A}}$	+0.000	+0.001	+0.001	+0.004
Fraction of $c\bar{c}$	$\Delta\mathcal{A}$	-0.000	-0.016	+0.055	-0.021
bkg in signal $\mathcal{F}_{c\bar{c}}$	$\Delta\sigma_{\mathcal{A}}$	+0.002	+0.005	+0.014	+0.039
world average value	$\Delta\mathcal{A}$	-0.000	+0.003	-0.029	-0.000
of $c\tau_{B_s}$ used	$\Delta\sigma_{\mathcal{A}}$	-0.001	-0.003	-0.007	-0.015
Uncertainty in modelled	$\Delta\mathcal{A}$	+0.001	-0.001	+0.008	-0.001
$\mu^+ D^-$ reflection	$\Delta\sigma_{\mathcal{A}}$	+0.001	+0.001	+0.002	+0.004
Stat. fluctuation	$\Delta\mathcal{A}$	+0.001	-0.000	+0.016	+0.009
of N_{D_s}	$\Delta\sigma_{\mathcal{A}}$	+0.001	+0.002	+0.004	+0.009
Resolution	$\Delta\mathcal{A}$	+0.010	-0.019	+0.075	+0.076
(signal)	$\Delta\sigma_{\mathcal{A}}$	+0.004	+0.016	+0.046	+0.102
Resolution	$\Delta\mathcal{A}$	-0.001	-0.001	-0.006	-0.011
(background)	$\Delta\sigma_{\mathcal{A}}$	-0.000	-0.000	-0.000	-0.001
Alternate paramterisation	$\Delta\mathcal{A}$	+0.021	+0.001	-0.042	+0.129
for dil. $\mathcal{D}(D)$	$\Delta\sigma_{\mathcal{A}}$	-0.002	-0.004	-0.002	-0.018
Fraction of bkg.	$\Delta\mathcal{A}$	+0.003	-0.002	-0.004	-0.005
sensitive to tagging	$\Delta\sigma_{\mathcal{A}}$	-0.000	-0.000	-0.000	-0.000
Fraction of bkg.	$\Delta\mathcal{A}$	-0.001	-0.001	-0.003	-0.006
oscillating with Δm_d	$\Delta\sigma_{\mathcal{A}}$	+0.000	-0.000	+0.000	-0.000
Alternative fit to	$\Delta\mathcal{A}$	+0.030	+0.004	+0.379	+0.363
signal VPDL distb.	$\Delta\sigma_{\mathcal{A}}$	+0.003	+0.021	+0.043	+0.179
Non-zero $\Delta\Gamma$	$\Delta\mathcal{A}$	+0.000	+0.000	-0.005	-0.001
	$\Delta\sigma_{\mathcal{A}}$	-0.000	-0.001	-0.001	-0.002
Total syst.	σ_{tot}^{syst}	0.068	0.117	0.337	0.497
Total	σ_{tot}	0.241	0.517	1.119	1.983

Table 5.1: Systematic studies shown at four example values of Δm_s

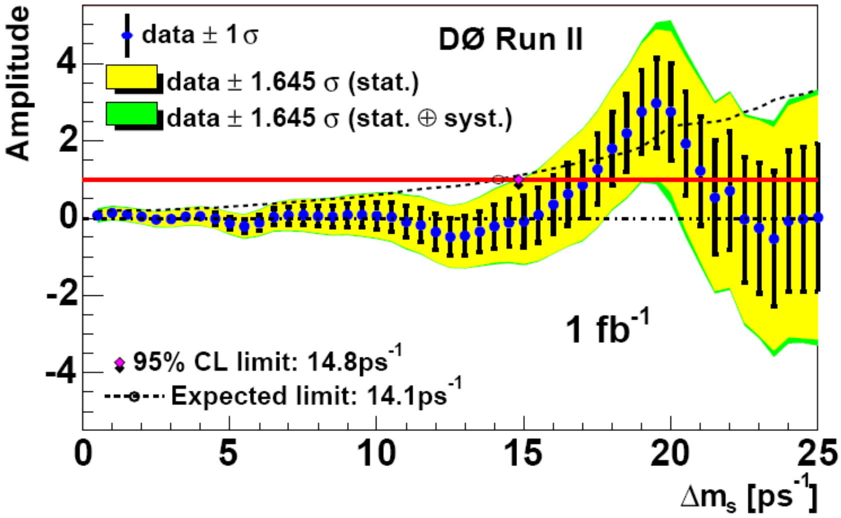

Figure 5.4: B_s^0 oscillation amplitude with statistical and systematic errors. The solid red line shows the $\mathcal{A} = 1$ axis. The dashed line shows the sensitivity $\sigma_{\mathcal{A}}$ including both statistical and systematic uncertainties. The expected limit corresponding to $\sigma_{\mathcal{A}} \geq 1$ was found to be 14.1 ps^{-1}. The measured limit corresponding to $\mathcal{A} + |\sigma_{\mathcal{A}}| \geq 1$ was found to be 14.8 ps^{-1}. There is a peak observed at $\mathcal{A} \sim 19$ ps^{-1} around which $\mathcal{A} \neq 0$ at a 95% confidence level.

In order to determine the significance of this result a log-likelihood fit was made, fixing $\mathcal{A}$ to 1, and varying Δm_s. The result is shown in Figure 5.5. The curve is well behaved and has a preferred value for Δm_s of 19 ps^{-1}. A 90% confidence limit can be taken for Δm_s to lie in the interval between 17 ps^{-1} and 21 ps^{-1} assuming Gaussian uncertainties. The lower limit of this bound is close to the world averaged limit of $\Delta m_s > 16.6$ ps^{-1} [18].

The statistical likelihood of this result was studied using ensemble testing. The log-likelihood scan was repeated many times using the same events but with the sign of the initial-state flavour tag assigned randomly. This simulates a data sample with B_s^0 oscillations at infinite frequency. These results were analysed to determine the probability of observing a likelihood minimum in the range $16 < \Delta m_s < 21$ ps^{-1} with the same or greater magnitude. This was found to occur in only $(5.0 \pm 0.3)\%$ of the test cases.

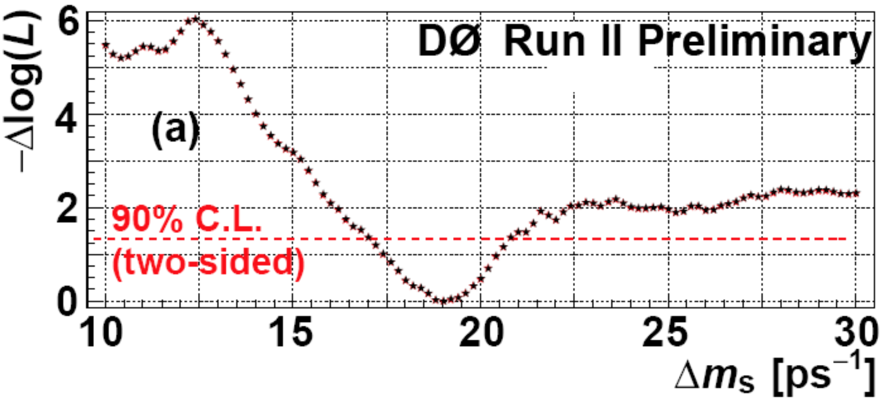

Figure 5.5: Likelihood scan over $\Delta m_s$with amplitude $\mathcal{A} = 1$. The dotted line is drawn to illustrate the 90% conifdence limits between 17 and 21 ps^{-1}, drawn with respect to the minimum at 19 ps^{-1}.

5.5 Cross checks

The validity of the analysis was cross-checked by measurement of the B_d^0-mixing frequency (Δm_d) using the μ^+D^- signal peak (see Figure 5.1). This was done both using the binned asymmetry fit method employed in the B_d analysis (described in Section 4.3.2), and an unbinned event-by-event fit, equivalent to that used in this analysis.

5.5.1 Binned asymmetry fit of Δm_d

The method described in Chapter 4 was repeated using B^0 and B^+ events in the μ^+D^- peak shown in Figure 5.1. The mass fits to the $M(K^+K^-\pi^-)$ distribution used a single Gaussian to describe the $D^- \to \phi\pi$ component, a double Gaussian for the $D_s^- \to \phi\pi$ component, and an exponential decay function to model the combinatorial background. The size and position of the signal Gaussians were fixed using a fit to the total tagged sample, and the background decay constant left free. The study of sample composition estimated the $D^- \to \phi\pi$ sample consisted of 90% oscillating B_d^0 decays and 10% non-oscillating B^+ decays. The events were divided into five bins of VPDL, with boundaries {-0.025, 0, 0.05, 0.1, 0.15, 0.25} chosen so each bin had sufficient statistics for fitting.

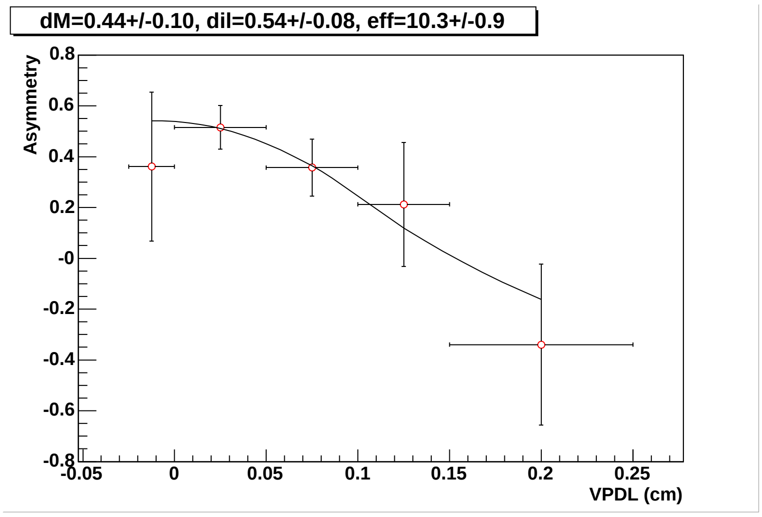

Figure 5.6: The asymmetries obtained in the $\mu^+ D^-$ sample using the combined tagger and $|d| > 0.3$ cut. The asymmetries are fitted to measure the B_d^0 oscillation frequency to be 0.44 ± 0.10 ps^{-1} consistent with the world averaged measurement.

Mass fits were performed for the set of all events tagged with $|d| > 0.3$ to find the numbers of oscillated and non-oscillated events in each VPDL bin. The asymmetry fitting code was modified to reflect the sample composition, and used to fit the measured asymmetries for Δm_d and the tag dilution $\mathcal{D}$ (constrained to be equal for both B^+ and B^0 components). The $c\bar{c}$ background was neglected in the calculation, therefore the first (negative) VPDL bin in which this background is most significant was assigned a zero weight in the fit.

The resulting fit can be seen in Figure 5.6. The measured value of $\Delta m_d = (0.44 \pm 0.10)$ ps^{-1} is in agreement with the world average and the result of the B_d mixing analysis. The measurement of dilution from the B_d mixing analysis was $\mathcal{D}_d = 0.44 \pm 0.02$, for the sample of all events tagged with $|d| > 0.3$. This can be compared to the equivalent result $\mathcal{D} = 0.54 \pm 0.08$ found for the $B \to \mu^+ D^-$, $D^- \to \phi\pi$ sample. The results are compatible within the large statistical errors and given the fact that the measurements come from different decay channels which may follow different d-distributions.

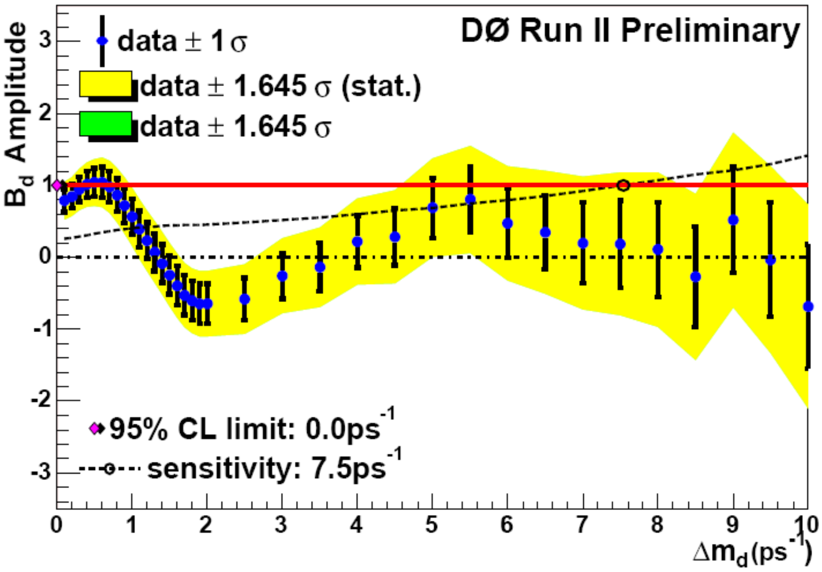

Figure 5.7: B_d^0 oscillation amplitude shown with statistical errors only. The solid red line shows the $\mathcal{A} = 1$ axis. The dashed line shows the sensitivity $\sigma\mathcal{A}$ using the statistical uncertainty only. The B_d^0 oscillations are clearly visible as the peak $\mathcal{A} = 1$ at ~ 0.5 ps^{-1}.

5.5.2 Amplitude fit for Δm_d

The amplitude fit analysis was performed on the $D^- \rightarrow \phi\pi$ mass peak, using modified PDFs to describe the number of oscillating and non-oscillating B_d^0 events. The resulting amplitude scan, with statistical errors only, can be seen in Figure 5.7. The amplitude $\mathcal{A}$ peaks with value $\simeq 1$ at $\Delta m_d \simeq 0.5$ ps^{-1}, demonstrating that the analysis performs as expected. The expected sensitivity for B_d^0 oscillations is at 7.5 ps^{-1}, which is lower than the sensitivity seen in the B_s amplitude scan due to the smaller sample statistics.

5.6 Conclusions

The calibration of the combined flavour tagger was an essential input into the B_s^0 mixing frequency analysis. The result of this analysis was the first two-sided limit on Δm_s to lie in the interval between 17 ps^{-1} and 21 ps^{-1} (90% CL), with the most probable value being 19 pb^{-1}. This was the first 1 fb^{-1} Tevatron Run II publication

[78], and is a huge success for the DØ collaboration.

The CKM fitter group used this limit to update the previous constraints on the unitarity triangle. The updated constraints are shown in Figure 5.8 and can be compared with the Summer 2005 constraints shown in Figure 2.3. The addition of the DØ double-sided limit has a significant effect on the $\Delta m_s/\Delta m_d$ constraint found using Equation 2.9, and places a tighter constraint on the apex of the unitarity triangle.

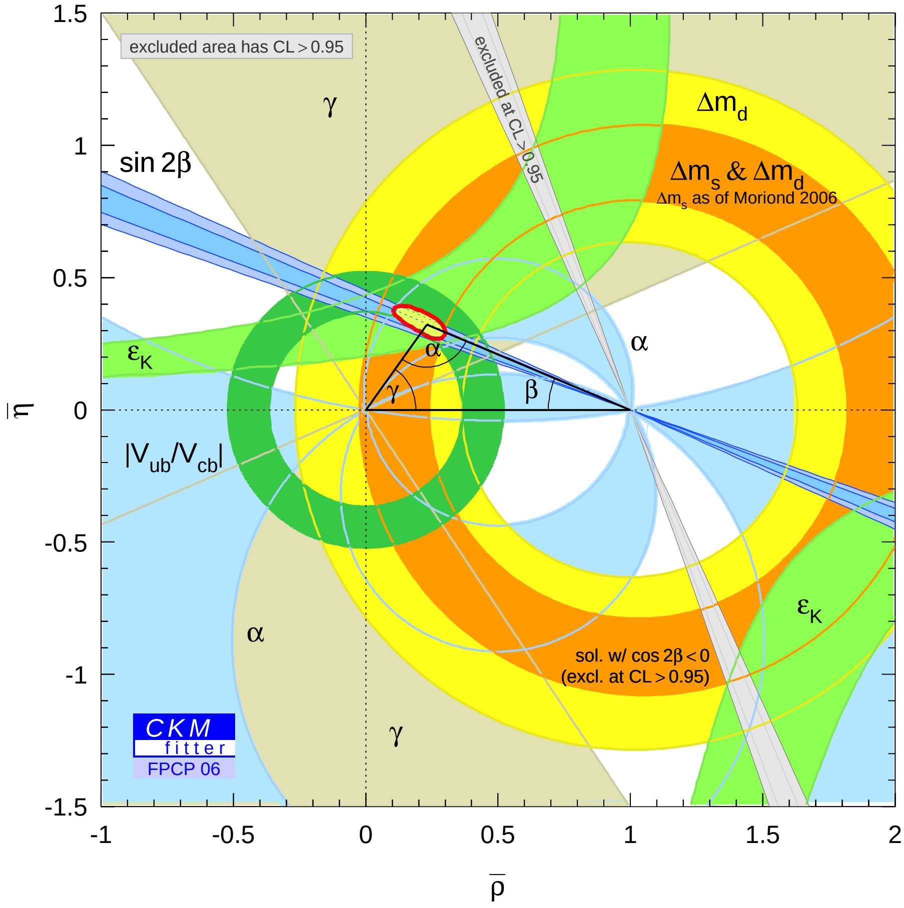

Figure 5.8: Constraints on the unitarity triangle, Spring 2006, with DØ result included.[20]

Subsequent improvements to the analysis will include the addition of additional semileptonic decay modes, fully reconstructed hadronic decay modes and the addition of same side tagging algorithms. This will improve the sensitivity of the analysis and should eventually lead to the observation of B_s-oscillations at DØ.

Chapter 6

Conclusions

6.1 Distributed Computing for DØ

Run IIa at the Tevatron has been successful, meeting the design specifications for peak and integrated luminosities. Over Run IIa the DØ detector has performed well, with data taking efficiency reaching $\sim$90%, so that more than 1 fb^{-1} of data has been recorded.

The storage and management of this dataset requires massive computational resources. Distributed computing via a grid provides the experiment with the means to use the substantial resources local to collaboration members, and is a fundamental aspect of the DØ computing model.

The work on DØ distributed computing projects described in this thesis covered the period in which Grid software and technologies were making the transition from development to production tools. Imperial College has made significant contributions to the development of the SAMGrid packages, and was one of the first operational remote sites. The work performed to extend the job broking and monitoring facilities, and the development of the *Storemgr* tool demonstrated the ability to run full Monte Carlo production using SAMGrid.

The p14 data reprocessing project was successful. The certification of all sites was managed at Imperial College. In total 300 M events were reprocessed over a

6 week period, with 100 M of these processed remotely. This was the first time that the reconstruction software had been used for official production offsite. The UK sites installed and managed by Imperial College made a significant contribution reprocessing 23 M events. The experience gained in the $p14$ data reprocessing was an essential input to the $p17$ data reprocessing project. This round of data reprocessing used SAMGrid to submit and monitor reprocessing jobs, and a common set of scripts to manage production. In total 470 pb^{-1} was reprocessed. This corresponds to almost 1000 M events or 250 TB of data and is the largest grid project to date in the field of high energy physics.

The successful completion of $p17$ reprocessing marked the maturation of the SAMGrid technologies and it is now the default for all production activities. A second round of $p17$ reprocessing took place in February 2006 in order to apply corrections to the hadronic calorimeter calibrations. Seven sites processed a data set of 1.5 billion events over a five week period. SAMGrid has been used for the production of Monte Carlo data in bulk. Testing is now taking place to use SAMGrid to run primary processing both onsite and remotely.

The use of SAMGrid has allows the collaboration to use LCG (and OSG) facilities, via either a local SAMGrid installation at each site, or via a SAMGrid forwarding node. This has enabled the DØ collaboration to make extensive use of the external computing resources coming online in preparation for the LHC experiment. In turn the lessons learnt from development and operation of SAMGrid will be very valuable for the LHC experiment.

6.2 B^0-oscillations

The measurement of the B_s oscillation frequency was a major physics goal of the DØ experiment. This measurement cannot be performed at the B-factories which operate at the $\Upsilon(4s)$ resonance, and is currently only accessible at the Tevatron.

Limits on Δm_scan be translated to give theoretically clean constraints on the CKM matrix which describes CP-violation in the Standard Model.

Performing a measurement of the B_d^0 mixing parameter is an essential step in the development of a B_s^0 mixing analysis. The larger statistics and less rapid oscillations mean that the B_d^0 decays are an excellent proving ground to understand and calibrate the tagging algorithm, and show that the sample composition and Monte Carlo inputs result in a measurement of Δm_d which is consistent with other measurements.

The combined opposite side flavour tagger described in this thesis was a significant improvement upon the previous tag tool [77]. It was tested on samples of B^0 and B^+ decays. The dilution of the tagger was found to be consistent for B^+ and B_d^0-meson reconstructed decays, which is necessary if the tool is to be applied to reconstructed B_s^0-meson decays.

By splitting the sample into bins according to the tagging variable $|d|$ and measuring the tagging power as the sum of individual tagging power in all bins, the following result was obtained

$$\varepsilon\mathcal{D}^2 = 2.48 \pm 0.21(\text{stat.})\ ^{+0.08}_{-0.06}(\text{syst})\ \%$$

Using a simultaneous fit to events in all $|d|$ bins, the mixing parameter Δm_d was measured to be:

$$\Delta m_d = 0.506 \pm 0.020\ (\text{stat}) \pm 0.016\ (\text{syst})\ \text{ps}^{-1}$$

which is in good agreement with the world average value of $\Delta m_d = 0.507 \pm 0.003(\text{sys}) \pm 0.003(\text{stat})\ \text{ps}^{-1}$ [18].

The calibration of the combined flavour tagger was an essential input into the B_s^0 mixing frequency analysis. The result of this analysis was the first two-sided limit on Δm_s to lie in the interval between 17 ps^{-1} and 21 ps^{-1} (90% CL), with the most probable value being 19 pb^{-1}. This was the first 1 fb^{-1} Tevatron Run II publication [78], and is a huge success for the DØ collaboration.

The CKM fitter group used this limit to update the previous constraints on the unitarity triangle. The updated constraints are shown in Figure 5.8 and can be compared with the Summer 2005 constraints shown in Figure 2.3. The addition of the DØ double-sided limit has a significant effect on the $\Delta m_s/\Delta m_d$ constraint found using Equation 2.9, and places a tighter constraint on the apex of the unitarity triangle.

Subsequent improvements to the analysis will include the addition of additional semileptonic decay modes, fully reconstructed hadronic decay modes and the addition of same side tagging algorithms. This will improve the sensitivity of the analysis and should eventually lead to the observation of B_s-oscillations at DØ.

The result has since been confirmed with an excellent result from the CDF collaboration which sees a B_s oscillation signal at a 3σ level [79]: $\Delta m_s = 17.4^{+0.3}_{-0.2}$ ps^{-1}.

References

[1] DØ Collaboration, “Observation of the Top Quark”, Phys. Rev. Lett. 74 2632 (1995).

[2] “Run II Handbook”, Fermilab beams division Run II web-page, http://www-bd,fnal.gov/runII/index.html

[3] DØ collaboration, “The upgraded DØ Detector”, Nucl.Instrum.Meth. A565 463-537 (2006).

[4] DØ collaboration, “The DØ Detector”, Nucl.Instrum.Meth. A338, 185 (1994).

[5] “Run II D0 Muon Identification”, DØ Muon ID Group web-page, http://www-d0.fnal.gov/ hedin/muonid.html

[6] “The Superconducting Solenoid” DØ Solenoid web-page, http://www-d0.fnal.gov/solenoid/index.html

[7] G. L. Kane, “Modern Elementary Particle Physics”, (1987).

[8] P. Higgs, “Broken Symmetries, Massless Particles and Gauge Fields”, Phys. Lett. 12 132. (1964).

[9] C. Wu *et al.*, “Experimental test of parity conservation in beta decay”, Phys. Rev. 105 1413 (1957).

[10] J. Christenson *et al.*, “Evidence for the decay of the K_2^0 meson”, Phys. Rev. Lett. 13, 138 (1964).

[11] J. Bell, Ph.D. thesis, Birmingham University, England, (1954).

[12] W.-M. Yao *et al.*, “The Review of Particle Physics”, Journal of Physics G 33, 1 (2006)

[13] A. D. Sakharov, “Violation of CP invariance, C asymmetry, and baryon asymmetry of the universe”, JETP 5: 24-27 (1967).

[14] M. Kobayashi, T Maskawa, “CP-violation in the Renormalizable Theory of Weak Interaction”, Prog. Theor. Phys 49, 652 (1973).

[15] L. Wolfenstein, “Parameterization of the Kobayashi-Maskawa Matrix”, Phys. Rev. Lett. 51, 1945 (1983).

[16] S. Eidelman *et al.* (Particle Data Group), Phys. Lett. B **592**, 1 (2004).

[17] M. Okamoto, “Full determination of the CKM matrix using recent results from lattice QCD”, XXIIIrd International Symposium on Lattice Field Theory, PoS LAT2005 (2005).

[18] Heavy Flavor Averaging Group, http://arxiv.org/abs/hep-ex/0603003.

[19] A. Ceccucci *et. al.* “The CKM quark Mixing Matrix” part of “The Review of Particle Physics” W.-M. Yao *et al.*, Journal of Physics G 33, 1 (2006).

[20] CKMfitter Group (J. Charles *et al.*), Eur. Phys. J. C41, 1-131 (2005), [hep-ph/0406184], updated results and plots available at: http://ckmfitter.in2p3.fr

[21] K. Anikeev *et al.*, “B Physics at the Tevatron: Run II and Beyond”, Section 2.4 (2002).

[22] O. Schneider, "$B^0 - \bar{B}$ Mixing", part of "The Review of Particle Physics" W.-M. Yao *et al.*, Journal of Physics G 33, 1 (2006).

[23] R. D. Field, "The Sources of b-Quarks at the Tevatron and their Correlations", Phys. Rev. D Journal-ref: Phys.Rev. D65 (2002).

[24] J. Nielsen, "Top Quark Pair Production at the Tevatron", Proceedings of the XXXXth Rencontres de Moriond: QCD and High Energy Hadronic Interactions (2005).

[25] Mangano, Michelangelo L., "The saga of bottom production in proton-antiproton collisions", 2004 Hadron Collider Physics Workshop, June 2004.

[26] CDF and DØ Collaborations, "*b*-production at the Tevatron", hep-ex/030933.

[27] E.Berger *et al.*, Phys. Rev. Lett. **86**, 4231 (2001).

[28] J. Stark, "B Physics at DØ", Proceedings of the 39th Rencontres de Moriond on Electroweak Interactions and Unified Theories (2004).

[29] K. Anikeev et al., "B Physics at the Tevatron: Run II and Beyond", Section 2.2 (2002).

[30] G.C.Blazey, "DZero Performance and Planned Improvements", http://nicadd.niu.edu/presentations/D0_Performance_Improvement.pdf (2005).

[31] DØ collaboration, "DØ Technical Proposal", Phys. Rev. Lett. 59 381-382 (1987).

[32] G. Borissov *et al.*, "The P14 Tracker Realignment", DØ Note 4161 (2003).

[33] A. Baranovski *et al.*, "SAM-Grid: Using SAM and Grid middleware to enable full function Grid computing", DØ Note 3630, (2002).

[34] I. Foster, “What is the Grid?”, *Grid Today* Vol. 1 No. 6 (2002).

[35] I. Bertram, *et. al.*, “Proposal for DØ Regional Analysis Centers”, DØ Note (2002).

[36] http://lcg.web.cern.ch/LCG

[37] http://www-d0db.fnal.gov/sam

[38] J. Frey *et. al.*, “Condor-G: A Computation Management Agent for Multi-Institutional Grids”, Journal of Cluster Computing, vol. 5 p237 (2002).

[39] http://www.cs.wisc.edu/condor/

[40] http://www.globus.org

[41] http://www-clued0.fnal.gov/runjob/

[42] http://www.openldap.org/

[43] http://www.cs.wisc.edu/condor/classad/

[44] http://www.fnal.gov/docs/products/ups/

[45] http://www-d0.fnal.gov/computing/grid/products/xmldb_client/doc/v1_0_5/api/xmldb.html

[46] http://www.w3.org/TR/xpath

[47] http://www-d0.fnal.gov/computing/grid/products/xmldb_client/

[48] http://www.w3.org/TR/xslt

[49] http://www-d0.fnal.gov/computing/algorithms/status/p14.html

[50] http://www.oracle.com/database/index.html

[51] http://www-d0.fnal.gov/computing/data_quality/d0_private/

[52] http://www-d0.fnal.gov/computing/reprocessing/p14/recocert/index.html

[53] http://www-d0.fnal.gov/computing/reprocessing/p17/

[54] http://gridengine.sunsource.net/

[55] http://www-d0.fnal.gov/computing/mcprod/Software/mcp17/mcp17.html

[56] http://www-d0.fnal.gov/computing/reprocessing/primary/

[57] BABAR Collaboration, Phys. Rev. D73, 012004 (2006).

[58] Belle Collaboration, Phys. Rev. D71, 072003 (2005)

[59] G. Borissov *et al.* "Bd mixing measurement using Opposite-side Flavor Tagging", DØ Note 4991 (2006).

[60] http://www-d0.fnal.gov/computing/algorithms/status/p14.html

[61] http://www-d0.fnal.gov/computing/algorithms/status/p17.html

[62] http://d0server1.fnal.gov/users/nomerot/Run2A/B_ANA.html

[63] http://www-d0.fnal.gov/D0Code/source/AATrack/.

[64] DELPHI Collaboration, Phys. Lett. B 475, 407 (2000).

[65] DELPHI Collaboration, "*b*-tagging in DELPHI at LEP", Eur. Phys. J. C32, 185 (2004).

[66] http://www-d0.fnal.gov/phys_id/muon_id/d0_private/certif/p14/index.html

[67] S. Catani *et al.* Phys.Lett. B269 (1991) 432.

[68] G. Borissov *et al.* "Measurement of Lifetime Ratio for Neutral and Charged B Mesons", DØ Note 4376 (2004).

[69] S. Burdin "First Direct Two-Sided Bound on the Bs Oscillation Frequency", http://d0server1.fnal.gov/users/burdin/talks/burdin_wandc20060324.ppt (2006)

[70] F. Beaudette and J.-F. Grivaz "The Road Method (an algorithm for the identification of electrons in jets)", DØ Note 3976, (2002).

[71] ALEPH Collaboration, Zeit. Phys. C73, 601 (1997).

[72] D. Scora and N. Isgur, Phys. Rev. D 52, 2783 (1995).

[73] D0 Collaboration, "Measurement of Bd mixing using opposite-side flavor tagging" submitted to Phys. Rev. D.

[74] M. Neubert, Phys. Rep. 245, 259 (1994).

[75] F. James, "MINUIT - Function Minimization and Error Analysis", CERN Program Library Long Writeup D506, 1998.

[76] D.J. Lange, Nucl. Instrum. Meth. A 462, 152 (2001); for details see http://www.slac.stanford.edu/ lange/EvtGen

[77] G. Borissov *et al.* "Opposite Side Flavor Tagging", DØ Note 4828 (2005).

[78] DØ Collaboration, "Direct Limits on the Bs Oscillation Frequency", Phys. Rev. Lett. 97 021802 (2006)

[79] http://www-cdf.fnal.gov/physics/new/bottom/050310.bsmix-combined